Aalborg University

Master Thesis in Materials Technology

Processing, Compatibilization and Molecular Dynamics Simulations of Immiscible Polyolefin/Copolyester Blends

Author:
Thomas Larsen

Supervisor:
Lars R. Jensen

The Faculty of Engineering and Science
Department of Materials and Production

3rd of June 2021

AALBORG UNIVERSITY
STUDENT REPORT

Title:

Processing, Compatibilization and Molecular Dynamics Simulations of Immiscible Polyolefin/Copolyester Blends

Project:

Master thesis

Project period:

February 2021 - June 2021

Members:

Thomas Larsen

Supervisor:

Lars R. Jensen

Number of pages: 60
Appendix: 9
Ended 3/6-2021

Abstract:

In this report the influence of temperature during extrusion compounding on the miscibility of polypropylene (PP) and poly(ethylene terephthalate glycol) (PETG) was investigated by microscopy and rheology. A trend of increased dispersed phase size with both dispersed phase content and temperature was observed. Furthermore, the effect of additional compatibilizer in a recycled blend of PP, high-density polyethylene, PET and compatibilizer was studied. It was found that the additional compatibilizer improved the dispersion. Mechanical tests revealed improved interfacial adhesion and toughness as a result of the presence of PET grafted with compatibilizer formed during extrusion compounding. Lastly, molecular dynamics simulations were used to study the miscibility of PP/PET blends by computing the Flory-Huggins χ-parameter. Values of χ indicative of full or slight immiscibility were found for most blends except the PP10/PET90 blend which appeared miscible. This was speculated to be partly caused by slight ordering of PET chains as observed from intermolecular radial distribution functions for carbon-carbon pairs. Two distinct glass transition temperatures (T_gs) of PP and PET in the PP75/PET25 blend suggested immiscibility, while a single T_g was found in a PP75/PET25 blend reactively compatibilized by maleic anhydride-grafted PP.

Preface

This master thesis was written by the undersigned author as part of the Master's degree programme in Materials and Nanotechnology with the specialisation in Materials Technology at the Department of Materials and Production at Aalborg University.

For literature reference, the IEEE citation style has been employed. Abbreviations for equations and figures are Eq. (#) and Fig. #, respectively, and the numbering is implemented according to their respective chapter and section.

For permissions to reproduce figures not made by the author, the reader is referred to Appendix I.

Acknowledgements

The author gratefully acknowledges supervisor Lars R. Jensen for helpful guidance with both the theoretical and experimental parts of this project.

The author further wishes to thank Allan V. Rasmussen from Plastix for providing the PETG, compatibilizer, and rPPC/PET blend, as well as for helpful discussions regarding parts of the project. Also, fruitful discussions with Kevin Barthomeuf from Bjørn Thorsen A/S are gratefully acknowledged.

Lastly, the author wishes to thank Thomas S. Quaade for introductions to experimental facilities.

Thomas Larsen

List of Abbreviations

AT	Acti-Tech 09MA13
CED	Cohesive Energy Density
CG	Coarse Grained
COMPASS	Condensed-phase Optimized Molecular Potential for Atomistic Simulation Studies
DMA	Dynamic Mechanical Analysis
DOC	Degree of Crystallinity
DP	Degree of Polymerization
FH	Flory-Huggins
FTIR	Fourier Transform Infrared Spectroscopy
HDPE	High Density Polyethylene
HT	High Temperature (260 °C)
LCST	Lower Critical Solution Temperature
LT	Low Temperature (250 °C)
MAH	Maleic Anhydride
MD	Molecular Dynamics (Simulations)
MFC	Microfibrillar Composite
MFR	Melt Flow Rate
MPW	Mixed Plastic Waste
MW	Molecular Weight
NHL	Nosé-Hoover-Langevin
PBC	Periodic Boundary Condition
PDI	Polydispersity Index
PET	Poly(ethylene terephthalate)
PETG	Poly(ethylene terephthalate glycol)
PLOM	Polarized Light Optical Microscopy
PP	Polypropylene
RDF	Radial Distribution Function
UCST	Upper Critical Solution Temperature

Summary

Blending of different polymers offers an attractive way of designing new materials. However, it is more often a rule rather than an exception that two components are immiscible, thereby limiting the applications where e.g. strength and toughness is required. However, the miscibility of polymer blends is influenced not only by the nature of the component polymers but also the type and conditions of processing. Thus, the first part of this report set out to investigate how the temperature profile during extrusion compounding would influence the miscibility and morphology of blends based on polypropylene (PP) and poly(ethylene terephthalate glycol) (PETG). Two different approaches were applied and their results compared, namely light microscopy and rheology. In the former, both the surface of the extruded strands and their melts were analysed, whereas in the latter frequency-sweep data was fitted to the Palierne model with dispersed phase size as a variable parameter. The Palierne model overestimated the observed dispersed phase sizes observed from microscopy measurements. Nonetheless, in both approaches the same trends were observed, namely an increase in dispersed phase size with increase in both dispersed phase content and processing temperature.

A common way of improving the adhesion between immiscible blend components is by adding a so-called compatibilizer which may either physically anchor both ends in the respective phases or chemically react with one of the components. Compatibilizers preferentially locate themselves at the interface of the blend components, thereby decreasing the interfacial tension and increasing the interfacial adhesion. Thus, the second part of this report investigated the influence of adding additional amounts of maleic anhydride (MAH) functionalized compatibilizer to a blend of recycled PP, high-density polyethylene (HDPE), poly(ethylene terephthalate) (PET), and $6\,wt\,\%$ of the MAH-functionalized compatibilizer. This blend was left-over from a production at the Danish recycling company Plastix. The influence of additional compatibilizer was studied by means of microscopy, infrared spectroscopy (FTIR), thermal and mechanical analysis. The microscopy analysis revealed an improved dispersion by adding compatibilizer to the blend, and FTIR suggested a chemical reaction between the PET component and MAH functional groups of the compatibilizer. This led to the formation of a copolymer of PET grafted with compatibilizer. Thermal and mechanical analysis suggested the formation of copolymer led to a decreased mobility of PET, and hence impeded crystallization, but also an improved interfacial adhesion due to enhanced toughness and elasticity in both the solid and molten states.

Molecular dynamics simulations (MD) have gained influence in the study of polymer properties, including miscibility of blends. In MD, the classical equations of motion are propagated in time by computing interactions commonly using force fields; the latter assigns to each particle a potential energy function with a large number of empirical parameters fitted to e.g. experimental or quantum mechanical data. The aim of the third part of the study was to investigate the miscibility of various PP/PET blends to study systems that closely resembled those investigated in the first two parts. This was firstly done by computing Flory-Huggins (FH) interaction parameters for the blends

which generally appeared immiscible or close to miscible from the data. However, the PP10/PET90 blend was predicted to be miscible due to its FH interaction parameter being significantly lower than the critical value. Additional investigations into the intermolecular radial distribution function (RDF) for carbon-carbon pairs generally revealed a tendency for carbon-carbon pairs in PET chains to be nearer each other compared to carbon-carbon pairs in dissimilar chains. Thus, it was speculated that part of the driving force for this slight ordering was dipole-dipole interactions between ester groups of PET. Furthermore, the immiscibility of the PP75/PET25 blend was investigated by dilatometry which allowed determination of the PP and PET glass transition temperatures. These were similar in both the PP75/PET25 blend and pure systems, thus suggesting immiscibility. The dilatometry was further used in the study of a PP75/PET25 blend reactively compatibilized by PP-g-MAH, i.e. PP grafted with MAH. The resulting PP/PP-g-PET blend contained the PP-g-PET copolymer and isolated PP chains, and the dilatometry revealed a single glass transition temperature in between those of PP and PET. Furthermore, on comparing the intermolecular RDFs between PP/PP-g-PET and PP75/PET25 the ordering of PET in the latter was absent in the former, and a greater tendency for carbon-carbon pairs in dissimilar chains, i.e. PP and PET, to locate near one another was observed.

Resumé

Blanding af forskellige polymerer er en attraktiv måde at designe nye materialer på. Det er dog oftere reglen end undtagelsen at to komponenter ikke er blandbare, noget som begrænser brugen af polymerblandinger hvor styrke og sejhed er krævet. Desuden afhænger blandbarheden ikke kun af komponenternes kemiske struktur - også proces-metode og -parametre spiller en betydelig rolle. Derfor er det formålet med første del af denne rapport at undersøge, hvilken indflydelse temperaturprofilen under ektrudering og kompoundering har på blandbarheden og morfologien af PP/PETG blandinger. Til dette formål er grundlæggende to metoder benyttet; optisk lysmikroskopi og reologi. I førstnævnte blev både overfladen af ekstruderede fibre og deres smelte undersøgt, mens sidstnævnte benyttede Palierne's model til at tilpasse data fra frekvens-sweep ved at variere radius af PETG-dråber som eneste variabel. Modellen overvurderede generelt dråbestørrelserne i fht. mikroskopiundersøgelserne. Alligevel viste begge metoder samme tendens i form af voksende dråbestørrelser som funktion af både øget PETG indhold og procestemperatur.

En typisk metode til at forbedre adhæsionen mellem ikke blandbare komponenter er ved at tilsætte en kompatibilisator. Afhængig af typen, så enten forankrer denne sig fysisk med begge ender i de respektive faser, eller denne reagerer kemisk med den ene fase. Kompatibilisatoren er fortrinsvist lokaliseret på grænsefladen mellem de to ikke blandbare faser, hvormed den sænker grænsefladespændingen og øger faseadhæsionen. I forlængelse af dette er målet for anden del af rapporten at undersøge effekten af yderligere tilsat MAH-funktionaliseret kompatibilisator til en blanding bestående af PP, HDPE, PET og $6\,\mathrm{wt}\%$ af den MAH-funktionaliserede kompatibilisator. Blandingen stammer fra en overskydende produktion hos plastgenanvendelsesvirksomheden Plastix. Effekten blev undersøgt vha. lysmikroskopi, FTIR, termiske og mekaniske undersøgelser. Mikroskopiundersøgelsen viste en forbedret spredning af faserne ved yderligere tilsætning af kompatibilisator. FTIR-undersøgelsen antydede en kemisk reaktion mellem PET og MAH, hvilket resulterede i dannelsen af en co-polymer bestående af PET grafted med kompatibilisatoren (PET-g-MAH). Termiske og mekaniske analyser indikerede en forringet krystalliseringsevne af PET, samt forbedret faseadhæsion grundet den observerede øgning i sejhed og elasticitet, sidstnævnte både i fast og smeltet form. Dette blev tilskrevet dannelsen af PET-g-MAH.

Molekylær dynamik simuleringer (MD) benyttes bredt til at simulere polymeregenskaber, herunder blandbarhed af polymerblandinger. I MD tidsudvikler et givent system sig iht. Newton's anden lov vha. såkaldte 'force fields'. Sidstnævnte tildeler hver partikel en parametriseret potentiel energi-funktion baseret på f.eks. eksperimentelt data og/eller kvantemekaniske beregninger. I denne forbindelse var formålet med rapportens tredje del at undersøge blandbarheden af forskellige PP/PET blandinger for dermed at kunne studere systemer som tilnærmelsesvis ligner dem fra rapportens forrige to dele. Undersøgelsen byggede først på beregnede Flory-Huggins interaktionsparametre (χ) som indikerede at blandingerne generelt var ikke blandbare. Undtagelsen var dog PP10/PET90 blandingen hvis χ var under den kritiske

værdi. Yderligere undersøgelser af de intermolekylære RDF'er for kulstof-kulstof par viste, at kulstof-kulstof par i PET-kæder generelt hyppigere var nærmere hinanden end kulstof-kulstof par i forskellige kæder. En hypotese kunne være, at dette delvist skyldtes en tendens til at danne dipol-dipol interaktioner mellem ester-grupperne i PET-kæderne; dette ville også delvist forklare den observerede blandbarhed hos PP10/PET90 blandingen. Desuden blev blandbarheden af PP75/PET25 blandingen yderligere undersøgt ved at finde glastransitionstemperaturen (T_g) af PP og PET. Denne var tilsvarende i både de rene systemer og PP75/PET25 for både PP og PET, hvilket indikerer, at PP75/PET25 blandingen ikke er blandbar. Ydermere blev (T_g) i den kompatibiliserede PP75/PET25 blanding (PP/PP-g-PET) undersøgt. Det var muligt at lokalisere én (T_g) mellem dem fundet i de rene PP og PET systemer, så denne blev tildelt PP-g-PET co-polymeren. Til sidst viste en sammenligning af de intermolekylære RDF'er for PP75/PET25 og PP/PP-g-PET, at førnævnte tendens til at finde kulstof-kulstof par i PET-kæder tættere på hinanden ikke var tilstede i PP/PP-g-PET. Modsat observeredes en kraftigere tendens til at finde kulstof-kulstof par i forskellige kæder tættere på hinanden i PP/PP-g-PET blandingen.

Contents

Chapter 1

Introduction

Polymer blends are characterized as a mixture of two or more polymers, and the attractiveness of blending can be explained by the possibility to manipulate the final material properties by proper selection of blend ingredients and appropriate compounding and processing methods. Blending of polymers also offers the opportunity to avoid the relatively high expenses associated with developing and commercializing new polymers. Moreover, polymer blends may be characterized based on their phase behaviour as either miscible or immiscible. The behaviour of a miscible blend is similar to that of a homopolymer, and it occurs when strong specific interactions are present, e.g. hydrogen bonds, dipole-dipole, and ionic interactions [1]. On the other hand, immiscible blends are generally characterized by multiple glass transition temperatures, and their properties are largely determined by the blend morphology. The latter depends on e.g. the thermodynamic and rheological properties of the components which implies complex flow responses. From a processing and fabrication perspective, this necessitates a consideration of not only the flow properties of the individual homopolymers (e.g. those determined by molecular weight and molecular weight distribution) but also the morphology and its evolution [2].

An example of the influence of processing conditions on blend miscibility is the work by T. Ougizawa et al. [3]. The authors e.g. studied blends of polystyrene/poly(vinyl methyl ether) which displayed a lower critical solution temperature (LCST), i.e. a one-phase region is found below a critical temperature. At low shear rates they found a shift in the cloud point curve to lower temperatures with increased shear rate, i.e. the two-phase region became larger. The shift was relative to the quiescent state. On the other hand, at shear rates of $14\,\mathrm{s}^{-1}$ and above the cloud point curve shifted to higher temperatures and remained unchanged. Thus, it is possible for shear flow to induce both phase demixing and mixing in the same blend whereas other blends (e.g. poly(methyl methacrylate)/poly(styrene-co-acrylonitrile)) only show one of these behaviours [3]. A different example is the study by J.-B. An et al. [4] which found that the nylon 4,6/poly(phenylene sulfide) blend, immiscible under quiescent conditions, became miscible at an 80/20 composition in a narrow range of shear rates and temperatures. J. K. Lee et al. [5] investigated the evolution of blend morphology for various blends during compounding in an internal mixer. For instance, the authors reported that a co-continuous morphology could be transformed into a dispersed morphology by 1) prolonging the mixing time (at fixed rotor speed), 2) increasing the rotor speed/shear rate (at fixed mixing time), or 3) increasing the temperature of the mixer. Furthermore, a phase inversion occurred if the minor component became liquid at a lower temperature than the major component. Hence, by heating the emulsion with initially dispersed major phase and allowing sufficient mixing, the structure

transformed into a co-continuous morphology before a dispersion of the minor component in the major component was attained. This led the authors to suggest the co-continuous morphology is a transitory morphological state.

B. D. Favis et al. [6] studied the morphology of an immiscible polycarbonate/polypropylene blend under various processing conditions. Firstly, the authors found a significant dependence of the dispersed phase particle size as a function of viscosity ratio between dispersed and matrix phases. This dependency was stronger in an internal mixer compared to a twin-screw extruder. Generally, the particle size increased with increasing dispersed phase viscosity in the internal mixer whereas it remained unchanged in the twin-screw extruder. Furthermore, at relatively high viscosity ratios the phase size was up to four times larger in the internal mixer compared to the twin-screw extruder. Moreover, the phase size remained unchanged with increasing screw speed in the twin-screw extruder.

Most polymers do not mix at the molecular level, and hence control of the morphology can be useful in achieving the desired properties. In this regard, the formation of reinforced fibers dispersed in a matrix phase is a preferable way to achieve favorable mechanical properties. This is described by K. Friedrich et al. [7] using polypropylene/poly(ethylene terephthalate) (PP/PET) blends in the weight ratio 60/40; the blends were melt blended and extruded, subsequently cold drawn to induce orientation of the two phases, and lastly injection or compression molded at temperatures below the melting temperature of PET but above that of PP. This resulted in microfibrillar composites (MFCs) with an isotropic PP matrix reinforced with PET microfibrils. However, despite the reinforcing effect of the microfibrils, the addition of a compatibilizer was required to improve the impact strength due to the incompatibility of PP and PET, and thus inherently poor interfacial adhesion.

In general, large interfacial tensions present in immiscible polymer blends will lead to phase separation and, given the heterogeneous blend is in the molten state, may lead to coalescence of particles and resulting poor mechanical properties [1]. However, the compatibility of the blend components may be improved by, as previously mentioned, a compatibilizer - typically a block or graft copolymer, or a chemically reactive species as e.g. maleic anhydride-grafted polyolefins. The compatibilizer serves to reduce the interfacial tension, thereby reducing the dispersed phase size, constraining phase coarsening, and improving mechanical properties by facilitating stress transfer between the phases [8].

As one of the numerous reasons for the generally poor plastic recycling rate in Europe, J. Maris et al. [9] mention the incompatibility of polymers. For mixed plastic waste (MPW), which may contain a variety of incompatible polymers, the authors mention mechanical recycling as a viable method for plastic recycling if properties can be improved by compatibilization. An example of MPW recycling is reported by E. P. A. van Bruggen et al. [10]. The authors considered the case of PP carpet backings with a minor fraction of PET shorn fiber. However, since the PP and PET were physically attached to each other, the melt blending of the two components would result in a two-phase morphology due to the inherent immiscibility of nonpolar PP and polar PET. Thus, the authors studied the influence of various commercial compatibilizers on the morphology and mechanical properties of the blends. Though the compatibilizers improved dispersion and toughness, their effectiveness was influenced by both processing temperature and content. Furthermore, the ability of the compatibilizer to migrate to the interface between dispersed and matrix phases, as well as the reactivity of functional groups in compatibilizers, may influence the effect of the compatibilizer in improving blend miscibility and properties [10].

Molecular dynamics simulations (MD) are a tool that may help in predicting and explaining experimentally observed structures and properties of materials, as well as complement in the design and discovery of new macromolecular materials. The significance of MD can be appreciated through the 2013 Nobel Prize in Chemistry for the development of multiscale models for complex chemical systems [11]. Furthermore, since high-performance computers are becoming increasingly powerful and widespread, the composites industry, for instance, is investing in MD tools for the design and screening of polymer systems relevant for future applications [12].

Classical molecular simulations of polymers are broadly described as either atomistic or coarse-grained (CG) [13]. In the former, one e.g. probes the monomer-level interactions to determine the Flory-Huggins interaction parameter between blend components [14]. On the other hand, CG simulations group together e.g. selected atoms or monomers into a single CG bead. This reduces the computational cost since it reduces some fast degrees of freedom, thus allowing for processing of larger spatial and temporal scales than atomistic molecular dynamics [15]. Since atomistic simulations are the focus of this work, a more in-depth description of CG models will not be pursued. MD propagates a system in time to obtain a trajectory of the motion described by Newton's Second Law. Relevant properties can be calculated for each stored 'frame' or 'snapshot' to obtain an average over the entire trajectory. However, atomistic models are computationally expensive and are typically limited to length scales of 1-100 Å and time scales of 1 fs to 100 ns [16]. Yet, applications of MD for simulating properties of polymers are varied and encompass e.g. macromolecular dynamics and diffusion phenomena [17]. However, of special interest to the present work is the prediction of miscibility in polymer blends using MD, a method which has gained acceptance as a reliable technique [18]. For instance, I. M. de Arenaza et al. [19] used MD to analyze the miscibility of poly(L-lactide)/poly(vinyl phenol) and poly(DL-lactide)/poly(vinyl phenol) as an alternative to the more cumbersome experimental miscibility studies.

Problem statements

The scope of the present work is threefold. Firstly, as explained above there are many factors influencing the miscibility of polymer blends during processing which necessarily calls for a delimitation. Hence, the scope of this project is to investigate the influence of different temperature profiles during extrusion compounding, a common industrial method of preparing blends [6], on the miscibility through morphological and rheological studies. The materials chosen for this purpose were PP and poly(ethylene terephthalate glycol) (PETG) due to their availability and widespread use in the industry. Secondly, this work seeks to examine the effect of different amounts of added compatibilizer to a recycled blend consisting mainly of the immiscible but industrially important polymers PP, PET, and high-density polyethylene (HDPE). The mixtures will be characterized using various mechanical and physico-chemical methods to establish and understand the effect of the added compatibilizer. Lastly, MD will be used as a tool to study the miscibility of PP and PET from a thermodynamic as well as structural point-of-view. An attempt is also made at probing the influence of PP grafted with maleic anhydride, a compatibilizer commonly used for compatibilizing PP/PET blends [20, 21], on the miscibility of a PP/PET blend.

Chapter 2

Theory

This chapter seeks to develop concepts and theories central to this report. Firstly, the Flory-Huggins theory will be presented and discussed wrt. evaluating the miscibility of polymer blends. This includes establishing criteria for the miscibility of polymer blends. Subsequently, theories related to the mechanism of compatibilization will be presented, whereafter two widely used compatibilization techniques - namely compatibilization by addition and reactive compatibilization - are examined. These concepts will be relevant for understanding the later blend compatibilization studies in this work. Lastly, central topics of molecular dynamics simulations are presented, e.g. force fields, thermostats and barostats. The exposition of molecular dynamics will by no means be comprehensive. Yet, along with the theory developed in the first section, it will provide the necessary foundation for understanding the simulations performed in this work.

2.1 Thermodynamics and Miscibility

This section is based on L. M. Robeson [22], E. Meaurio et al. [14], and Z. Stary [23]. The mixing of two components at conditions of constant temperature and pressure is associated with a change in Gibbs free energy of mixing

$$\Delta G_m = \Delta H_m - T \Delta S_m, \tag{2.1}$$

where T is temperature, and ΔH_m and ΔS_m are the enthalpy (heat consumed or generated during mixing) and entropy of mixing, respectively. Henceforth, subscript 'm' will denote 'mixing'. Equation (2.1) is e.g. applied in determining the miscibility of mixtures. Firstly. If one considers an ideal solution, i.e. a mixture where the strength of intermolecular equals the strength of interactions between pure components, the mixing enthalpy is zero since no particular interactions are favored over others. Hence, ΔG_m is entirely determined by the entropy of mixing. However, in real solutions or mixtures, which are non-ideal, some interactions will be preferred over others, e.g. due to hydrogen bonding. In this case both the enthalpy and entropy of mixing contribute to ΔG_m. Mixing of polymers has turned out to generally yield materials with inferior mechanical properties due to the unfavorable thermodynamics of mixing.

One condition for the mixing process to be spontaneous is

$$\Delta G_m < 0. \tag{2.2}$$

This could e.g. be achieved by heat being generated during mixing ($\Delta H_m < 0$) and/or an increase in entropy (or randomness) ($\Delta S_m > 0$). However, in order to observe a single-phase system this criterion is not sufficient. To ensure stability of a single-phase system requires

$$\left(\frac{\partial^2 \left(\Delta G_m\right)}{\partial \phi^2}\right)_{p,T} > 0, \tag{2.3}$$

i.e. the Gibbs free energy of mixing-curve must be upward concave. This latter requirement can be understood in terms of the schematic phase diagram for a polymer blend in Fig. 2.1. Three distinct regions are indicated; the binodals separate the single-phase from metastable regions, while the spinodals divide the metastable and two-phase regions. Blends with compositions in the metastable region require an energy input to overcome an energy barrier preventing the spontaneous phase separation into two phases with the binodal compositions (B' and B'' in Fig. 2.1). This is the basis of Eq. (2.3) as one condition for single-phase stability.
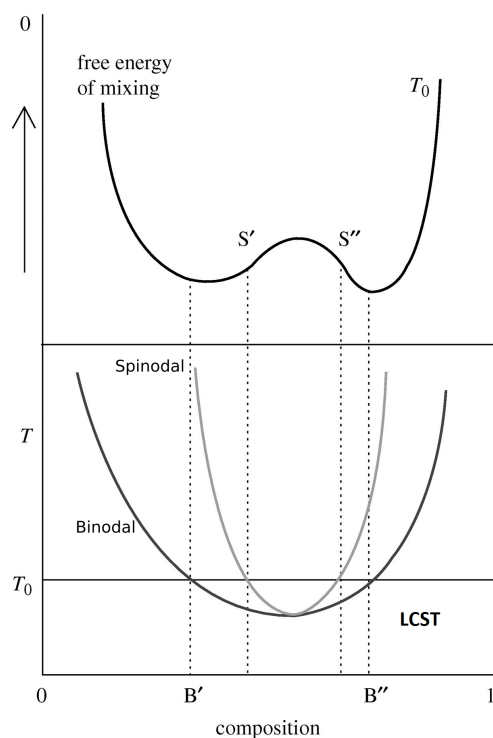
FIGURE 2.1: Schematic showing (top) a curve of the Gibbs free energy of mixing (ΔG_m) at a temperature T_0 for a typical polymer blend, and (bottom) a phase diagram for the same blend showing a lower critical solution temperature (LCST). The binodal and spinodal are indicated by the solid black and grey lines, respectively. Adapted from J. S. Higgins et al. [24] under the terms of Creative Commons CC BY license.

Furthermore, from Fig. 2.1 it can be seen that the spinodal compositions (indicated by S' and S'') are located through the condition

$$\left(\frac{\partial^2 \left(\Delta G_m\right)}{\partial \phi^2}\right)_{p,T} = 0, \tag{2.4}$$

i.e. at the inflection points of the Gibbs free energy of mixing-curve. Moreover, the binodal compositions (indicated by B' and B") are located through the condition

$$\left(\frac{\partial\left(\Delta G_m\right)}{\partial\phi_i}\right)_{T,P,n_j}^{\text{phase1}} = \left(\frac{\partial\left(\Delta G_m\right)}{\partial\phi_i}\right)_{T,P,n_j}^{\text{phase2}}, \tag{2.5}$$

which is equivalent to stating that the chemical potential of species i is equal in both phases at thermodynamic equilibrium. Thus, in Fig. 2.1 the binodal compositions are found by drawing a common tangent intersecting both minima, ensuring the same slope and hence chemical potential in both minima.

To further develop the thermodynamics of blends, the Flory-Huggins (FH) theory can be employed. P. J. Flory [25] and M. L. Huggins [26] considered a regular solution[1] of a polymer and solvent on a rigid lattice with only one molecule or repeat unit being able to occupy a single site at a time. As mentioned by P. J. Flory, the thermodynamic properties of ideal binary solutions are determined by the entropy of mixing

$$\Delta S_m = -R\left(n_1 \ln x_1 + n_2 \ln x_2\right), \tag{2.6}$$

which is based on random molecular mixing of components 1 and 2 on a rigid lattice. In Eq. (2.6) R is the universal gas constant, and n_i and x_i represent the number of moles and mole fraction of component i, respectively. However, it can be recognized that for a polymer (1)-solvent (2) mixture the addition of polymer will practically render the free energy of mixing unchanged since $n_2 \ln x_2 \gg n_1 \ln x_1$.

The treatment of a dilute polymer solution can, however, be extended to the case of a binary polymer blend as illustrated in Fig. 2.2.
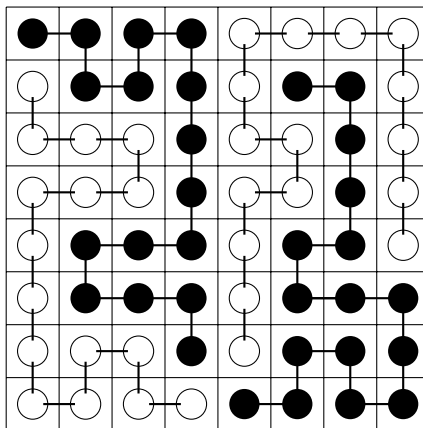
FIGURE 2.2: The Flory-Huggins rigid lattice model for a polymer blend. The black and white dots represent chain segments of two distinct types of polymer.

The Flory-Huggins theory assumes all members of species i are of similar size. Furthermore, the lattice comprises N cells with a total volume V with each polymer occupying a volume V_i. Furthermore, every monomer unit is assumed to occupy the volume of one cell as seen in Fig. 2.2. Thus, it is inviting to define the volume fraction of species i as $\phi_i = V_i N_i / \left(\sum_1^2 V_i N_i\right)$ with N_i being the number of molecules of polymer

---

[1]Entropy of mixing as ideal solution, but non-zero enthalpy of mixing. No volume change upon mixing.

i. By replacing the mole fractions in Eq. (2.6) for the volume fractions, the (molar) combinatorial entropy of mixing becomes

$$\Delta S_m = -RV \left[\frac{\phi_1}{\nu_1} \ln \phi_1 + \frac{\phi_2}{\nu_2} \ln \phi_2 \right], \tag{2.7}$$

where ν_i is the molar volume of species i. However, the choice of monomer units such that the polymers occupy a similar volume may become problematic if the two polymer species are distinctly different chemically. Yet, the effect of replacing x_i with ϕ_i accounts more realistically for the entropy of mixing observed in polymer solutions and blends.

From Eq. (2.7) it is seen that entropy favours mixing due to $\phi_i < 1$ in a blend combined with Eq. (2.1). Furthermore, the combinatorial entropy is greatly reduced in going from a polymer solution to a polymer blend since ΔS_m is proportional to the number of molecules of a given species; for polymers there is a loss in combinatorial entropy due to the linkage of individual repeat units. Generally, for blends of high molecular weight (MW) polymers the combinatorial entropy is small compared to the enthalpy of mixing

$$\Delta H_m = \frac{\chi_{12}}{\nu_r} RTV \phi_1 \phi_2, \tag{2.8}$$

where ν_r is the reference molar volume often calculated from the individual molar volumes as $\nu_r = \sqrt{\nu_1 \nu_2}$, and χ_{12} is the FH interaction parameter.

One way of defining χ_{12} is through the Hildebrand approach, which introduces solubility parameters δ_i for each component i in the mixture. This allows Eq. (2.8) to be rewritten in terms of the Hildebrand solubility parameters as

$$\Delta H_m = (\delta_1 - \delta_2)^2 V \phi_1 \phi_2, \quad (\delta_1 - \delta_2)^2 = \frac{\chi_{12} RT}{\nu_r}. \tag{2.9}$$

The solubility parameter is related to the cohesive energy E_{coh}, i.e. the measure of intermolecular attractive energy (or equivalently the energy of vaporization from liquid to ideal gas state), as

$$\delta^2 = CED = \frac{E_{coh}}{V}, \tag{2.10}$$

where CED is the cohesive energy per unit volume, i.e. cohesive energy density. For polymers, δ can e.g. be obtained from intrinsic viscosity measurements in different test solvents of known δ-values. Better solvents will lead to stronger interactions and greater polymer chain extension, thus yielding higher intrinsic viscosities. The solubility parameter of the polymer is then taken as the δ of the solvent yielding the most viscous solution. However, the method is only reliable in determining solubility parameters for polymers that lie in the range of the test solvents; due to being in a state in between solid and liquid, the cohesive energies of polymers may be too high to dissolve them, leading to underestimated solubility parameters [23, 27]. Thus, as the discrepancy between δ_1 and δ_2 decreases the miscibility increases. It is worth noting that Eq. (2.9) can evaluate the miscibility of two polymers from knowledge of the pure components only. Moreover, using the definition of solubility parameters in Eq. (2.9) the interaction parameter will always be positive or zero. Thus, the best predictions

for interaction parameters will be achieved for nonpolar polymer blends with only weak interactions. To account for specific interactions, more elaborate expressions for Eq. (2.9) have been developed as mentioned by J. M. Hughes et al. [28]. Yet, these are beyond the scope of this project.

For a mixing process at constant pressure P involving a regular solution, i.e. the volume of mixing $\Delta V_m = 0$, the enthalpy (defined, in general, as $H = U + PV$) of mixing ΔH_m equals the internal energy of mixing ΔU_m

$$\Delta H_m = \Delta U_m = U_{12} - (U_1 + U_2), \tag{2.11}$$

where U_i are internal energies of the pure components, and U_{12} is the internal energy of the mixture. Moreover, the derivation of Eq. (2.9) assumes that changes in internal energy of the mixing process can be approximated by changes in the cohesive energy. By acknowledging that cohesive energies are positive (see Eq. (2.10)) while internal energies are defined with opposite sign [14], one can substitute E_{coh} for U in Eq. (2.11) while dividing by the total volume V and recalling that $V\phi_i = V_i N_i$, i.e. the total volume of component i. This results in

$$\frac{\Delta U_m}{V} = \phi_1 \left(\frac{E_{coh}}{VN} \right)_1 + \phi_2 \left(\frac{E_{coh}}{VN} \right)_2 - \left(\frac{E_{coh}}{V} \right)_{12}, \tag{2.12}$$

where subscripts on the parentheses mean e.g. $\left(\frac{E_{coh}}{VN} \right)_1 = \frac{E_{coh,1}}{V_1 N_1}$ and $V_{12} = V$. Hence, using Eqs. (2.11) and (2.12) allows rewriting Eq. (2.8) in terms of cohesive energies as

$$\chi_{12} = \left[\phi_1 \left(\frac{E_{coh}}{VN} \right)_1 + \phi_2 \left(\frac{E_{coh}}{VN} \right)_2 - \left(\frac{E_{coh}}{V} \right)_{12} \right] \cdot \frac{\nu_r}{RT\phi_1\phi_2}. \tag{2.13}$$

Equation (2.13) is commonly used in molecular dynamics simulations to obtain the FH interaction parameter [14, 18, 19, 29], and it is also the method used in this study. It is seen that one may obtain $\Delta U_m/V$ by building cells for the pure and mixed polymer systems and calculating CEDs for each system.

Combining the combinatorial entropy in Eq. (2.7) and enthalpy of mixing in Eq. (2.8) with the definition in Eq. (2.1) allows writing the FH equation for the Gibbs free energy of mixing of a polymer blend as

$$\Delta G_m = RTV \left[\frac{\phi_1}{\nu_1} \ln \phi_1 + \frac{\phi_2}{\nu_2} \ln \phi_2 + \phi_1\phi_2 \frac{\chi_{12}}{\nu_r} \right]. \tag{2.14}$$

From Eq. (2.14) it is seen that, depending on the magnitude of the combinatorial entropy, a low or negative interaction parameter (promoted by e.g. hydrogen bonds) favours mixing of the polymers.

It is relevant to know the critical value of the FH interaction parameter leading to an immiscible blend. This requires directing the attention to the spinodal curve which is defined in Eq. (2.5) and schematized in Fig. 2.1. Furthermore, the critical composition at which the binodal and spinodal merge is related to the extremum of the spinodal curve; as the spinodal defines the compositions ϕ satisfying the condition $\frac{\partial^2 (\Delta G_m)}{\partial \phi^2} = 0$, the critical point is located by imposing on the rate of change of the spinodal wrt. composition

$$\left(\frac{\partial^3 \left(\Delta G_m\right)}{\partial \phi^3}\right)_{p,T} = 0.$$ (2.15)

Thus, using Eq. (2.15) while assuming χ_{12} is independent of composition allows finding the critical composition, $\phi_{1,c} = \left(1 + \sqrt{\nu_1/\nu_2}\right)^{-1}$, at which the spinodal and binodal merge. Using this expression for $\phi_{1,c}$ in Eq. (2.4) leads to the critical FH interaction parameter

$$\chi_c = \frac{\nu_r}{2}\left[\frac{1}{\sqrt{\nu_1}} + \frac{1}{\sqrt{\nu_2}}\right]^2.$$ (2.16)

This implies that an increase in number of chain segments in the polymers decreases χ_c ($\nu_i = M_i/\rho_i$ is the ratio of molecular weight to density, i.e. molar volume) and hence favours phase separation since the miscibility region is defined by $\chi_{12} < \chi_c$.
The FH theory does, however, have some drawbacks. For instance, in the derivation of Eq. (2.16) it was assumed that the FH interaction parameter was independent of polymer concentration. However, this assumption is known to be incorrect for many polymer-containing systems [30–32]. Moreover, only nearest-neighbour interactions are considered. Yet, in systems with electrostatic interactions this assumption is likely not justifiable due to their long-range nature. Furthermore, the model neglects any volume change that could occur due to interactions, e.g. the negative volume change in the case of favorable intermolecular attractions such as hydrogen bonding. Moreover, in the case of distinctly different thermal expansion coefficients of the blend components, the existence of two separate lattice structures is preferable. The latter decreases the combinatorial entropy and hence favours phase separation with increasing temperatures. Also, energetically favorable arrangements of polymer molecules are not taken into account, i.e. the random choice of lattice sites does not hold true in the case of favorable arrangements.
As seen in Eq. (2.1) the miscibility is improved with increasing temperature, i.e. an upper critical solution temperature (UCST) is modelled. Furthermore, for blends containing high MW polymers a temperature change is ineffective towards improving the miscibility due to the inherently low combinatorial entropy. Thus, in order for the FH equation to capture the phase behaviour associated with a lower critical solution temperature (LCST), see Fig. 2.1, the FH interaction parameter can e.g. be expressed as [33, 34]

$$\chi_{12}\left(T\right) = a + \frac{b}{T},$$ (2.17)

where a and b are constant parameters. Using Eq. (2.17), a LCST behaviour can be captured for instance if the constant b is negative, while UCST behaviour is captured by a positive value of b. In ending this section it is worth pointing out that comparing χ_{12}-values for different blends is typically not meaningful. M. Tambasco et al. [34] present how different polymer blend systems exhibiting 1) similar values and trends of χ_{12} (in their case UCST behaviour) display critical temperatures (temperature at which binodal and spinodal coincide) differing by over 100 K in value, and 2) similar values of χ_{12} display opposite critical behaviour (UCST and LCST).

2.2 Compatibilization of Polymer Blends

This section is based on Z. Stary [23], J. Maris et al. [9], and L. A. Utracki [35]. Compatibilization is the process whereby additives are used to promote the miscibility between components of an immiscible blend by optimizing the interfacial tension to suppress phase separation. By increasing the adhesion between the phases in the solid state, stress transfer is facilitated and mechanical properties improved. Apart from lowering of the interfacial tension, this process also leads to a reduction in the rate of coalescence, and thus a decrease in domain size. Even though the mechanism for the latter is unknown [36], two possible explanations have been proposed, and both are illustrated schematically in Fig. 2.3. Firstly, U. Sundararaj et al. [37] proposed that coalescence suppression originates from steric repulsive forces between the droplets resulting from the compression of block copolymer chains at the surface of two approaching droplets. This lowers the number of possible configurations of the copolymers, and hence reduces the entropy. An elastic repulsion is thus generated between the approaching droplets. The second explanation considers the coalescence suppression in terms of a compatibilizer concentration gradient at the interface [38]. The compatibilizer concentration gradient causes an interfacial tension gradient, resulting in a Marangoni stress (see hollow arrows in Fig. 2.3a) which attempts to redistribute the compatibilizer at the interface. This in effect immobilizes matrix fluid in the gap between two approaching droplets, thus preventing drainage of matrix material and thereby delaying coalescence.

(a)   (b)
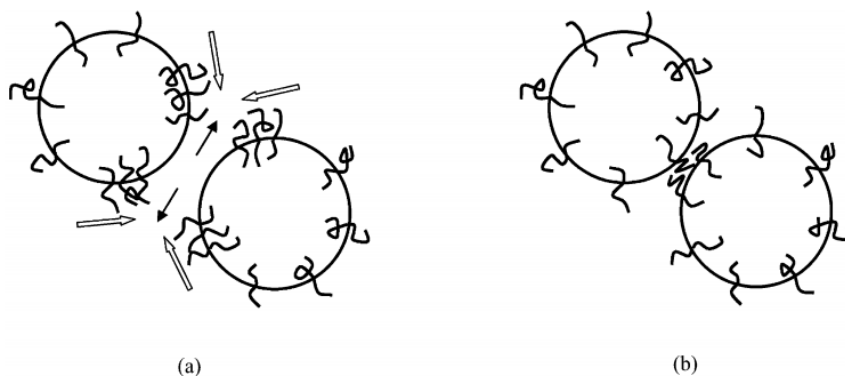
FIGURE 2.3: A schematic illustration of two possible explanations for coalescence suppression in compatibilized polymer blends. (a) Marangoni stress (hollow arrows) due to compatibilizer concentration gradient at the interface. (b) Steric repulsion due to compression of block copolymers at the surface. Reproduced from P. Van Puyvelde et al. [39] with permission from Elsevier.

The remainder of this section will focus on two possible compatibilization pathways, namely compatibilization by addition and reactive compatibilization. In case of the former the prepared additive, typically a block or graft copolymer, is added to the immiscible blend. It may form specific interactions (hydrogen bonding, dipole-dipole, ionic, to name a few) with the main polymeric components, anchoring its segments in the respective polymer, thereby promoting miscibility. Moreover, the copolymer should have a molecular weight (MW) just above the entanglement MW for each block. This is due to diffusion to the interface being impeded by a relatively high MW which directly affects the morphology of the blend as well as compatibilization efficiency. Furthermore, the copolymer concentration in the blend should be minimized; at thermodynamic equilibrium the copolymer not only dissolves in the interphase, it also

dissolves in the matrix and dispersed phases. Increasing the compatibilizer concentration above some critical value will subsequently lead to micelle formation, resulting in increased blend viscosity and deteriorated mechanical performance. However, the problem of micelle formation may be alleviated to some extent by using tapered instead of di- or triblock copolymers due to the gradual change in chemical composition of the former [40]. Another example of the influence of copolymer architecture (random, alternating, diblock, stars and combs) and chain length on compatibilization efficiency was presented by Y. Lyatskaya et al. [41]. The authors found that diblock copolymers were most efficient at reducing the interfacial tension at a fixed MW. However, long random or comb copolymers were found to be more efficient than short diblock copolymers.

Rather than using preformed grafted or block copolymers, reactive compatibilization relies on a chemical reaction in the interphase to produce the interfacial agent of interest during melt blending. The precursor polymer is miscible or compatible with one of the blend components, and its pendant or end groups are reactive towards the second blend component. For instance, polymers grafted with maleic anhydride (MAH) are widely used in reactive compatibilization (see e.g. Fig. 2.4).
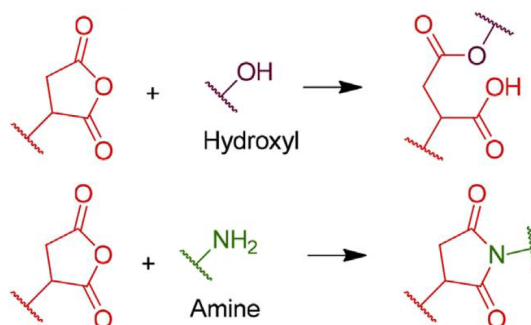
FIGURE 2.4: Examples of functional groups present in blend components and reactive towards cyclic anhydride-grafted polymers; hydroxyl groups of e.g. polyesters (top), and amine groups of e.g. polyamides (bottom). Adapted from J. Maris et al. [9] with permission from Elsevier.

For instance, due to the nonpolar nature of polypropylene (PP), the grafting of MAH on PP can endow it with a compatibilization functionality [42, 43], e.g. in PP/PET blends [44]. Other pendant groups grafted onto PP could be glycidyl methacrylate which was also employed as an effective compatibilizer in PET/PP blends [45, 46]. Some advantages over compatibilization by addition is e.g. that the compatibilizer only forms at the interfaces and not in the bulk, and the problem of block copolymer transport to the interface is not relevant since the copolymers are formed at the interface. However, for efficient compatibilization the processing conditions require e.g. the residence time in the processing unit be sufficiently long compared to the reaction rate. Moreover, the mixing should ensure sufficient dispersion and distribution of material to continually supply fresh interface to be compatibilized.

2.3 Molecular Dynamics Simulations

One of the aims of this work is to investigate the miscibility of polymer blends using the theory developed in the previous two sections. For this purpose molecular dynamics simulations (MD) will be used, and hence this section will provide the necessary background that will allow one to perform the miscibility studies. Furthermore, the

theory presented in this section is based on T. E. Gartner, III et al. [13] and J. M. Haile [47].

The aim of MD is to calculate the trajectory of a set of interacting particles in a given system over a finite time interval. If the system contains N particles, then each particle position is contained in the vector $\mathbf{r}^N = (\mathbf{r_1}, ..., \mathbf{r_N})$ of length $3N$. The classical equations of motion

$$\mathbf{F}_i = m_i \ddot{\mathbf{r}}_i(t), \quad \mathbf{F}_i(\mathbf{r_1}, ..., \mathbf{r_N}) = -\nabla_i \mathcal{U}(\mathbf{r_1}, ..., \mathbf{r_N}), \quad i = 1, \ldots, N \qquad (2.18)$$

with dots indicating time derivatives, are then solved step by step. In Eq. (2.18), m_i is the mass of atom i, and the force $\mathbf{F}_i$ on atom i is derived from the potential energy function $\mathcal{U}(\mathbf{r}^N)$, also known as the *potential energy surface*. Its origin is quantum mechanical, and its derivation follows based on splitting the molecular Schrödinger equation into an electronic and nuclear part using the Born-Oppenheimer approximation. It is hereby assumed that the motion of the nuclei are sufficiently slow that it can be decoupled from the motion of the electrons. Hence, the motion of the nuclei can be said to take place on the potential energy surface $\mathcal{U}(\mathbf{r}^N)$ [48].

As seen in Eq. (2.18), a set of initial velocities and positions are required to solve the coupled differential equations. Thus, knowing the forces on each atom allows the calculation of the updated velocity and position vectors using a finite difference integration scheme; a discussion of these is, however, beyond the scope of this project. Yet, when one is concerned with the motion of light particles such as hydrogen atoms, the molecular Schrödinger equation must be solved [49].

Solving the equations of motion above generates a detailed microscopic description of the positions $\mathbf{r}^N$ and momenta $\mathbf{p}^N$ of the system particles. However, one is often interested in some macroscopic measureable property A. This property is measured over a finite time interval whereby the computed time average becomes

$$A_{\mathrm{MD}} = \frac{1}{M} \sum_{j=1}^{M} \mathcal{A}\left(\mathbf{r}^N(j\Delta t), \mathbf{p}^N(j\Delta t)\right). \qquad (2.19)$$

A_{MD} denotes the macroscopic, measureable property as computed by MD, and the MD simulation is performed over a finite time interval of M time steps of size Δt. At equilibrium this interval average is assumed to reliably approximate the true time average as will be discussed in a later subsection.

Force field

In MD calculations the demanding electronic structure and internuclear interaction calculations are often omitted by use of a force field. This is a classical approximation to the above-mentioned quantum mechanical potential energy surface $\mathcal{U}(\mathbf{r}^N)$ in Eq. (2.18). It typically consists of two main components, namely bonded and non-bonded interactions. The former typically describes the evolution of bond lengths, angles and torsions, whereas the latter accounts for electrostatic and dispersive interactions. A generic force field could thus be

$$\mathcal{U}(\mathbf{r}^N) = \mathcal{U}_{\mathrm{bond}} + \mathcal{U}_{\mathrm{angle}} + \mathcal{U}_{\mathrm{dihedral}} + \mathcal{U}_{\mathrm{nonbonded}}. \qquad (2.20)$$

The first term represents bond stretching, and the quantum-mechanical solution is often approximated by a Morse potential $\mathcal{U}_{\mathrm{Morse}} = D_b \left[1 - e^{-\alpha(b-b_0)} \right]^2$ with D_b being the well depth, α a constant, and $b-b_0$ the displacement from the equilibrium bond length [50]. However, if $b-b_0$ is small the classical harmonic oscillator $\mathcal{U}_{\mathrm{harm.\ osc.}} = k_b \left(b - b_0 \right)^2$ with k_b being a force constant is often used. Since the latter requires fewer parameters per bond to be determined, the latter may be preferable from a computational point-of-view. Similarly to the bond potential, the bond angle (θ) bending might be represented by a harmonic potential by replacing bond lengths with bond angles, i.e. $\mathcal{U}_{angle} = k_\theta \left(\theta - \theta_0 \right)^2$.

The third term in Eq. (2.20) considers dihedral angle (ϕ) potentials and relies on four atoms. The resulting interactions are less restrictive on the configurations compared to bond and angle terms, and thus multiple minima exist. An example of a functional form is $\mathcal{U}_{\mathrm{dihedral}} = k_\phi \left[1 + \cos \left(n\phi - \delta \right) \right]$ with k_ϕ a force constant, n the multiplicity corresponding to the number of minima, and δ an offset parameter determining the location of minima [51].

The nonbonded interactions include Coulomb's law $\mathcal{U}_{\mathrm{Coulomb}} \propto r_{ij}^{-2}$ in the case of electrostatic interactions, and an attractive $\mathcal{U}_{\mathrm{dispersion}} \propto r_{ij}^{-6}$ in the case of interacting dipolar molecules. The repulsive forces due to Pauli repulsion are typically modelled as $\mathcal{U}_{\mathrm{repulsion}} \propto r_{ij}^{-12}$, which is the square of the attractive dispersive interaction making it relatively efficient to compute. An alternative could be an exponential decrease with distance as used in the Buckingham potential, which describes internuclear interactions at moderate distances well [52].

Finally, some force fields include cross-terms that correct intramolecular energies by taking into account the coupling between bond stretching, angles and torsions; for example bend/stretch- and bend/torsion-coupling, to name a few [52]. The above-mentioned functional forms are not unique, and a variety of different force fields exists; Dreiding [53] and Universal [54] (or UFF) for all elements of the periodic table, CHARMM [55] commonly used for biomolecules, and COMPASS (Condensed-phase Optimized Molecular Potential for Atomistic Simulation Studies) optimized for condensed matter [56], the functional form of which is presented and commented in Appendix A since it is applied in this report.

The force fields have been fit to results of quantum mechanical calculations and/or experimental measurements on various chemical species at a specific set of experimental conditions. Subsequent testing of the force fields ensures their ability to reproduce experimentally observed properties, e.g. glass transition temperature and cohesive energy to name a few. Thus, one should ideally choose a force field that was developed for the system of interest.

Periodic boundary conditions

For typical system sizes encountered in MD simulations of bulk properties it is generally not fruitful to construct the simulation domain inside a container with rigid walls with which particles may collide but cannot escape. Since, at any time, a significant fraction of all particles are located near the rigid walls they will experience a different environment than bulk particles. Thus, they are unable to capture the properties of an interior particle. Hence, a more convenient path is to use periodic boundary conditions (PBCs). In this approach the simulation box containing all N particles is replicated and thus surrounded by images of itself such that the system no longer has a surface. This is illustrated in Fig. 2.5.

A consequence of this is that a particle leaving its simulation box will reenter it from
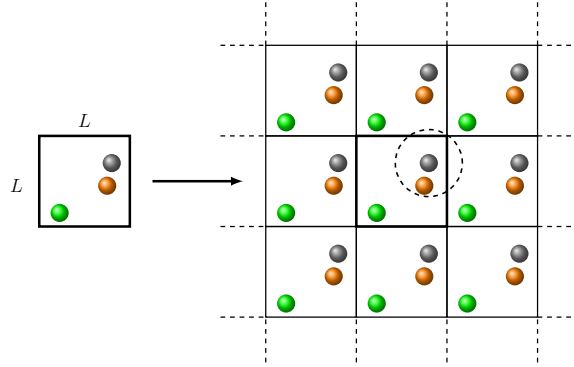
FIGURE 2.5: Schematic of a two-dimensional square-shaped simulation domain of size L containing three distinct particles (left) subjected to periodic boundary conditions (right). The dashed circle in the centered simulation box illustrates the concept of the radial cut-off distance.

the opposite side - the so-called wrap-around effect. Thus, the greatest separation between particles is effectively half the shortest lattice parameter; if interaction forces persist over longer distances, a given particle in the simulation box may interact with its own periodic images. However, non-bonded terms as e.g. van der Waals interactions decay rapidly with interatomic separation, thus permitting the truncation of these interactions above some specified radial cut-off distance r_c. Thus, if $r_c < L/2$ then a given particle will at most interact with the nearest periodic image of a surrounding particle. This limit to the radial cut-off distance is called the minimum image convention.

In the case of electrostatic interactions it is not straight-forward to assign a cut-off distance since these are long-ranged interactions $\propto 1/r$. The Ewald summation method [57, 58], for example, was initially developed to evaluate the electrostatic potential experienced by one ion in the presence of all other ions in an ionic crystal. However, the method can also be applied in the study of systems subject to the above-mentioned PBCs. Briefly, in the Ewald method a slowly convergent sum is decomposed into two rapidly convergent sums, thus allowing high accuracy of the computed electrostatic interactions. In this method, the decaying term becomes

$$\frac{1}{r} = \frac{\text{erf}\,(\beta r)}{r} + \frac{\text{erfc}\,(\beta r)}{r}, \tag{2.21}$$

where $\text{erf}(x)$ is the error function and $\text{erfc}(x) = 1 - \text{erf}(x)$. The first term in (2.21) is evaluated in the reciprocal space while the second term is evaluated in the real space. The proper choice of the convergence parameter β will then allow a rapid convergence when summing the interactions. A more detailed analysis of the Ewald method is, however, beyond the scope of this project.

Sampling

The objective of MD simulations is to estimate time averages as exemplified earlier in Eq. (2.19). However, at equilibrium this finite time average is assumed to reliably approximate the infinite-time average

$$A_{\text{MD}} = \langle A \rangle, \quad \text{where} \quad \langle A \rangle = \lim_{\tau \to \infty} \frac{1}{\tau} \int_{\tau_0}^{\tau_0 + \tau} \mathcal{A}\left(\mathbf{r}^N(t), \mathbf{p}^N(t)\right) dt. \tag{2.22}$$

Here τ_0 is an arbitrary starting time, and the angular brackets $\langle \cdots \rangle$ denote a time average. Yet, the validity of this approximation poses firstly the question of how long the sampling time must be. As mentioned by J. M. Haile [47], if the complete equilibrium phase-space trajectory of an isolated system is discretized into M_∞ points with an associated trajectory average $\langle A \rangle$, while MD simulations sample $M << M_\infty$ points with a resulting sample average $\langle a \rangle$, then under conditions of random sampling and $M << M_\infty$ the expected variance

$$E\left[(\langle A \rangle - \langle a \rangle)^2\right] \propto \frac{1}{M}. \tag{2.23}$$

Thus, the precision of the sampling does not depend on the total length of the trajectory M_∞, i.e. it is not necessary to let $M \to M_\infty$. Rather, the precision depends on the number of sampled points M. Furthermore, whether the systematic sampling of MD generates a random sample can be investigated by a time correlation function $C(t)$. It is a coefficient that measures the strength of correlation between a property $a(t)$ at successive time steps. As $C(t) \to 0$ successive measurements become uncorrelated, and the characteristic time for this to occur is the relaxation time. Thus, to obtain a valid approximation of the infinite-time average, sampling can be performed over several multiples of the relaxation time for a given property. These relaxation times, however, depend on the property of interest [47].

Secondly, if the structure is in a metastable state the equilibrium fluctuations of $A(t)$ can be suppressed, making the equality in Eq. (2.22) doubtful. To test for metastability, the initial conditions of the motion can be altered or thermal energy can e.g. be donated to the system, using one of various techniques to be discussed later. This may drive the system over any energy barriers within reasonable time.

Lastly is the question of whether the system is properly equilibrated. Measureable properties fluctuate with time. For instance, the total energy of an isolated system is constant but the kinetic and potential energy components may fluctuate so as to keep their sum constant. However, when the kinetic and potential energies fluctuate around constant values, and other key properties no longer change with time, the system may be said to have been equilibrated [16].

The equations of motion Eq. (2.18) are energy conserving. This implies that the system is isolated with no means to exchange mass or heat with the surroundings. Equivalently, the total energy $E = \mathcal{K}\left(\mathbf{p}^N\right) + \mathcal{U}\left(\mathbf{r}^N\right)$ as a sum of kinetic and potential energy, number of particles N, and volume V remains unchanged as the system moves along its trajectory. Thus, the parameters NVE describe the thermodynamic state of the system. Assuming both sampling of the entire phase space as well as infinite numerical precision, i.e. an absence of numerical rounding errors, MD will sample the microcanonical ensemble or NVE-ensemble [59]; this is known as the ergodic theorem which states that the time average of Eq. (2.22) equals the ensemble average, the latter being an average over phase space. Yet, the time-averaged property computed by MD in (2.19) is not likely to represent the microcanonical ensemble since only a subset of the possible system configurations will be explored; these are the ones most quickly accessible to the initial configuration [16]. Thus, the ergodic theorem is impossible to satisfy by simulations [60].

Thermostats

Many polymer properties are dependent on the temperature of the surroundings; density depends e.g. on strength of intermolecular interactions, and the density in

turn influences the mechanical properties. This is readily observable in the laboratory. As mentioned above, in the absence of energy drift and assuming ergodicity holds, MD essentially samples the microcanonical ensemble. Thus, temperature (and pressure) will vary so as to maintain constant average energy and volume. However, it may be desirable to maintain the average temperature of the system constant, or one might be interested in cooling down the system from a molten state to the solid state. This requires an algorithm that adds or removes energy as required. In MD this can be achieved by coupling the system to a large heat reservoir through a thermostat [61]. Different thermostats exist, one being the Andersen thermostat, as formulated by H. C. Andersen [62]. It considers the system to be coupled to a heat bath of fictitious particles imposing stochastic impulsive forces on randomly selected system particles. The resulting change in momentum of the particles occurs instantaneously, and the new momentum magnitude is chosen at random from a Maxwell-Boltzmann distribution at the desired temperature $\mathcal{T}$

$$p\left(v_{x,i}\right) = \sqrt{\frac{m_i}{2\pi k_B \mathcal{T}}} \exp\left(-\frac{m_i v_{x,i}^2}{2 k_B \mathcal{T}}\right), \tag{2.24}$$

with no memory of the previous momentum. Here v_x is the velocity component in the x–direction, and k_B is the Boltzmann constant. A similar expression is obtained for the two other particle velocity components v_y and v_z. All other particles are unaffected by this stochastic collision. Thus, in between collisions the thermodynamic state of the system is described by the NVE-ensemble. However, each collision event transfers the system from one constant energy surface to another. Apart from $\mathcal{T}$, a second parameter ν is used to specify the strength of the coupling to the heat bath, i.e. the frequency of collisions. Hence, the probability of a particular particle participating in a collision event in a small time interval Δt is $\nu \Delta t$. However, since the collisions with the heat bath are stochastic, the dynamics are perturbed in an unphysical way, especially if the collision frequency is large [59, 63]. Moreover, a too low collision frequency results in a loose coupling and hence poor temperature control [59].

A different type of thermostat considers scaling of the particle velocities at each time step, the Berendsen thermostat being one such example [64]. The scheme considers a weak coupling to an external heat bath through an exponential decrease in temperature with time described by $dT/dt = (\mathcal{T} - T)/\tau_B$. Here, τ_B is a relaxation time describing the strength of the coupling, $\mathcal{T}$ is the heat bath temperature, and T is the instantaneous temperature. This results in a proportional scaling of the velocities per time step from v to λv with [64]

$$\lambda = \sqrt{1 + \frac{\Delta t}{\tau_B}\left(\frac{\mathcal{T}}{T} - 1\right)}. \tag{2.25}$$

A relatively large value of τ_B corresponds to a weaker coupling since longer time is required to bring about the desired temperature change. Hence, in the limit $\tau_B \to \infty$ the Berendsen thermostat becomes inactive and the microcanonical ensemble is sampled [59]. On the other hand, a small value corresponds to tight coupling with unrealistically small temperature fluctuations; for instance, letting $\tau_B = \Delta t$ does not allow for temperature fluctuations.

Lastly, it is worthwhile mentioning the Nosé-Hoover thermostat originally formulated by S. Nosé [65] and reformulated by W. G. Hoover [66]. This method includes the heat bath as an additional (fictitious) degree-of-freedom in the equations of motion.

This dynamic variable $\tilde{s} > 0$ of the now extended system is associated with a fictitious 'mass' $Q > 0$ (units of energy×time^2), and the former serves as a scaling factor between the physical system and extended system times (and hence velocities). However, it may be noted that in the extension by W. G. Hoover [66], the scaling of velocities and time is avoided by introducing a parameter ζ which includes this scaling factor. A more thorough mathematical analysis of the Nosé-Hoover thermostat is, however, beyond the scope of this project. Here, it suffices to present the equations of motion to be solved in this approach [59, 66]

$$\dot{\mathbf{q}}_i = \frac{\mathbf{p}_i}{m_i}, \quad \dot{\mathbf{p}}_i = -\frac{\partial \mathcal{U}\left(\mathbf{q}^N\right)}{\partial \mathbf{q}_i} - \zeta \mathbf{p}_i, \quad \dot{\zeta} = \frac{3N k_B T}{Q}\left[\frac{T}{\mathcal{T}} - 1\right]. \qquad (2.26)$$

Here, $(\mathbf{q}, \mathbf{p})$ represent the phase-space coordinates, $\mathcal{U}$ is the potential energy, ζ is a friction coefficient which can be of either sign, while T and $\mathcal{T}$ again play the roles of instantaneous and heat bath temperatures, respectively. For example, if the instantaneous temperature exceeds the heat bath temperature, the friction coefficient will tend to increase. The choice of the parameter Q influences the coupling strength to the heat bath. A large value of Q, i.e. a loose coupling, will result in poor temperature control. Indeed, in the limit $Q \to \infty$ (and $\zeta = 0$) the NVE-ensemble is sampled due to vanishing thermostatization. On the other hand, a small value of Q implies a low-inertia heat bath resulting in rapid temperature fluctuations; these oscillations may, however, become off-resonant with the highest-frequency fluctuations of the system, leading to long kinetic energy transfer times.

Barostats

To mimic the environment of a laboratory test, it is often desirable to conduct a simulation at constant pressure rather than constant volume. For instance, both the glass transition temperature and the melting temperature in case of amorphous and semi-crystalline polymers, respectively, depends on the local movements of polymer chains. Thus, e.g. an increase in pressure will hinder these movements, requiring more energy to be put into the system for the transition to occur, i.e. additional heat must be supplied. Knowledge of these dependencies is important e.g. in the polymer processing industry [67]. Hence, to maintain the pressure constant the system volume must be allowed to fluctuate. In the method proposed by H. C. Andersen [62] the size of the simulation box is allowed to vary but not the shape. Here, the coordinates of the simulation domain are normalized to the volume of the simulation box which is now a dynamic variable, i.e. $\mathbf{r}_i = \mathbf{q}_i / V^{1/3}$. In this connection, V can be interpreted as the coordinate of a piston whose acceleration is determined by the external pressure P_{ext} and the instantaneous pressure P_{inst} of the system through

$$\ddot{V} = \frac{P_{inst} - P_{ext}}{M}. \qquad (2.27)$$

The parameter M can be regarded as the mass of the piston; for a relatively small value of M the volume of the simulation box will fluctuate rapidly, while a large mass will result in slow volume adjustments. In the limit $M \to \infty$ of the fictitious mass, the barostatization vanishes since the volume effectively stays fixed. Thus the NVE-ensemble is sampled.

A different constant pressure-approach is taken by H. J. C. Berendsen [64] where the

pressure is controlled by a weak coupling to a pressure bath. Similarly to the Berendsen thermostat, the Berendsen barostat considers periodic rescaling of the simulation box length and particle coordinates over a time interval Δt through

$$\mu = \left\{ 1 - \Delta t \frac{\beta}{\tau_P} \left[\mathcal{P} - P(t) \right] \right\}^{\frac{1}{3}}. \tag{2.28}$$

Here β is the isothermal compressibility, τ_P is a relaxation time of the pressure bath, $\mathcal{P}$ is the target pressure, and $P(t)$ is the instantaneous pressure. Lack of knowledge about β does not critically affect the system dynamics since the algorithm relies on the user-defined relaxation time τ_P. Furthermore, by observing Eq. (2.28) it is seen that a larger value for the relaxation time results in a weaker coupling to the pressure bath and vice versa.

The Berendsen barostat aims to exponentially dampen the pressure difference $\mathcal{P} - P(t)$ at each rescaling step, albeit not realistically [68]. Yet, E. Braun et al. [16] suggest the use of the Berendsen barostat for quickly bringing the system to the desired pressure, while e.g. the Anderson barostat is more suitable for final equilibration since it does not behave well far from the target pressure.

A final question pertaining to both thermostats and barostats is whether the given algorithm, assuming ergodicity, samples the correct ensemble. For instance, in the canonical (or NVT) ensemble, the macroscopic temperature $\mathcal{T}$ has a specified average value. Yet, the instantaneous temperature T is allowed to fluctuate with a variance [59]

$$\sigma_{\mathcal{T}}^2 = \left\langle T^2 \right\rangle_{NVT} - \left\langle T \right\rangle_{NVT}^2 = \frac{2\mathcal{T}^2}{N_{df}}. \tag{2.29}$$

Here, $\langle \cdots \rangle_{NVT}$ denotes an ensemble average, and N_{df} is the number of internal degrees of freedom in the system. It is e.g. seen that the fluctuations become smaller as the system size grows, but P. H. Hünenberger [59] mentions they are often non-negligible for systems encountered in MD simulations. Moreover, it is also clear from Eq. (2.29) that e.g. aggressive velocity scaling as mentioned for the Berendsen thermostat Eq. (2.25) in the limit $\tau_B = \Delta t$ precludes sampling of the canonical ensemble due to suppression of temperature fluctuations.

Radial distribution function

The radial distribution function (RDF) is a non-normalized function which measures the organization of atoms around one another, i.e. it is proportional to the probability of finding a particle at a distance r from another particle. Specifically, it can be written as [69]

$$g(r) = \lim_{dr \to 0} \frac{p(r)}{4\pi \frac{N_{pair}}{V} r^2 dr}, \tag{2.30}$$

where $p(r)$ is the average number of atom pairs in a spherical shell between r and $r + dr$, V is the volume of the system, and N_{pair} is the number of unique pairs of atoms; one atom is from each of two sets, and N_{pair} thus depends on whether the two sets are the same or share no atoms. The RDF can hence be seen a a measure of the local density relative to a uniform distribution of particles. Therefore $g(r)$ approaches

unity as distance from the center increases since one atom should eventually have no influence on the position of another atom. Moreover, at one extreme structures displaying crystallinity will show relatively sharp and narrow peaks with $g(r) > 1$, whereas $g(r) < 1$ in between the atoms on the lattice. Thus, the short range order present in liquids can also be characterized by $g(r)$.

Since the average number of atom pairs $p(r)$ is generally calculated as an ensemble average, it is calculated over a finite number of frames in the context of MD. Furthermore, due to finite sampling the function $p(r)$ is replaced with a histogram of bin width Δr [69]. This presents a compromise since this finite shell thickness must be small enough to resolve significant features of $g(r)$. On the other hand, a larger value will allow sampling a larger population, thus obtaining more statistically reliable results. Furthermore, since MD simulations are typically performed on cubic containers, the largest spherical shell radius to fit inside the container is $\frac{1}{2}L$, where L is the dimension of the container. However, the necessary information contained in $g(r)$ for molecules interacting through short-range forces is, as mentioned by J. M. Haile [47], typically present within this limit.

Chapter 3

Methods

3.1 Materials

For the polypropylene/poly(ethylene terephthalate glycol) (PP/PETG) blends, a PP homopolymer from Borealis AG (HG265FB, melting temperature = 161-165 °C, melt flow rate (MFR) (230 °C/2.16 kg) = 26 g/10 min) and PETG from Eastman Chemical Co. (Eastar EB022, density 1.27 g/cm^3, processing melt temperature = 249-271 °C) was used.

The rPPC/PET was obtained from recycled maritime ropes by Plastix and delivered as mixed granulate. Here, rPPC is a circa 70/30 wt.% mixture of PP and high-density polyethylene (HDPE), and PET is poly(ethylene terephthalate). The rPPC/PET contained roughly 6 wt.% Acti-Tech 09MA13 (AT) compatibilizer (Nordic Grafting Company, density = 0.89 g/cm^3, maleic anhydride (MAH) content > 1.0 %, MFR (190 °C/2.16 kg) = 15 g/10 min). This AT was later added in different amounts, and thus rPPC/PET refers to the as-received mixture. The ratio of rPPC to PET was 84/16 in wt.%. PETG, compatibilizer, and rPPC/PET was kindly supplied by Plastix.

3.2 Sample Preparation

Compounding and extrusion

The PETG and rPPC/PET was vacuum dried overnight at 60 °C to avoid hydrolysis of PETG and PET during processing at elevated temperatures. Subsequently, the PP/PETG were mixed in weight ratios of 75/25 and 50/50, whereas either 0, 4 or 6 wt.% AT was added to the rPPC/PET, which henceforth is referred to as rP-PC/PET/X (X=0, 4, 6 wt.% AT).

The melt blending of both PP/PETG and rPPC/PET/X blends was performed in a PRISM Eurolab 16 twin-screw extruder (Thermo Scientific, Waltham, MA) with six temperature-controlled zones and parameters shown in Table 3.1. The extruded strands were pulled through a water bath with demineralised water, left to dry for roughly two hours, then pelletized and vacuum dried overnight at 60 °C. Inspired by A. D. Drozdov et al. [70] who melt mixed low-density polyethylene and PP on the same extruder, the above.mentioned process was repeated twice to ensure a homogeneous distribution of components.

Piston injection molding

The dried rPPC/PET/X pellets were piston injection molded into rectangular specimens (80 mm×10 mm×3 mm) and tensile specimens (ASTM D638 type IV) using a

TABLE 3.1: Processing parameters used during compounding on the twin-screw extruder. [T_{profile} states the temperature in all six barrel zones.]

	PP/PETG				rPPC/PET/X		
	75/25LT	75/25HT	50/50LT	50/50HT	X=0	X=4	X=6
T_{profile} (°C)	250	260	250	260	280	280	280
Screw RPM	200	150	180	150	200	200	200

HAAKE MiniJet II (Thermo Scientific, Waltham, MA). For all blends and both specimen types the pellets were melted in a heated cylinder at 280 °C for three minutes. Subsequently, the melt was injected with 200 bar for 5 s into a mold heated at 110 °C. The post-pressure was 300 bar for 10 s to ensure the mold was completely filled.

The surface of the rectangular specimens opposite the mold entrance appeared frayed with fibrillar structures (see Fig. C.1). This was speculated to be a consequence of high shear stresses and cooling of the melt inside the mold, thus causing fibers of PET to be drawn due to the relatively high melting temperature of PET; a phenomenon qualitatively similar to the MFCs mentioned in the introduction [7].

3.3 Characterization

Polarized light optical microscopy

Both for the PP/PETG and rPPC/PET/X blends pellets were chosen at random and their surface analysed with polarized light using a Zeiss Axio Imager 2 (Carl Zeiss Microscopy GmbH, Jena, Germany). The center of the pellet was used for image analysis since the morphology may vary with radial position of extruded strands [6]. Due to the relatively rough surfaces, a Z-Stack acquisition was performed in the AxioVision SE64 software (Carl Zeiss Microscopy GmbH, Jena, Germany). This procedure combined a number of slices taken at a constant intervals. Image analysis was performed in ImageJ 1.53e (NIH, USA). Subsequent data analysis was performed in MATLAB (The MathWorks, Inc., MA).

Rheometry

Oscillatory shear tests were performed on a TA Instruments (New Castle, DE) Discovery HR-3 hybrid rheometer equipped with a 40 mm parallel plate geometry. Measurements were performed using a gap height of 1 mm and within the linear viscoelastic range as ensured by performing strain amplitude sweeps. After equilibrating the samples for 30 minutes at the measurement temperature, frequency-sweeps were performed with a strain amplitude of $\gamma = 0.05$ and frequencies ranging from 600 rad/s down to 0.016 rad/s under nitrogen atmosphere to minimize thermal degradation.

Model fitting was performed using Microsoft Excel and the built-in nonlinear regression algorithm 'Solver' to obtain parameters that yielded the best fit to the measured data. An initial guess for the parameters was provided, and subsequently the best-fit parameters were found by minimizing the residual

$$\sum_{\omega_i} \left\{ \left[\log_{10}\left(G'_{fit}(\omega_i)\right) - \log_{10}\left(G'_{data}(\omega_i)\right) \right]^2 + \left[\log_{10}\left(G''_{fit}(\omega_i)\right) - \log_{10}\left(G''_{data}(\omega_i)\right) \right]^2 \right\},$$

(3.1)

where the subscripts 'fit' and 'data' denote values calculated by the model and measured experimentally, respectively.

Hot-stage microscopy

PP/PETG specimens were melted on a glass slide situated on a Linkam THMS 600 (Linkam Scientific Instruments, Tadworth, United Kingdom) hot stage at 250 °C or 260 °C before carefully pressing the molten blend to a thin film with a glass slide. Temperature was controlled by a Linkam T95-PE controller. The hot stage was mounted on a Nikon (Tokyo, Japan) Labophot-2 microscope. Images were acquired with an Evolution LC Color (Media Cybernetics, Inc., Silver Spring, MD) camera. Image analysis was performed in ImageJ 1.53e, and subsequent data analysis was carried out in MATLAB.

Fourier transform infrared spectroscopy

Infrared spectra were gathered with a Thermo Scientific (Waltham, MA) Nicolet iS20 FTIR Spectrometer. An initial background spectrum was collected before the sample spectra. The number of scans was 32, and the data spacing was $0.482 \, \text{cm}^{-1}$.

Differential scanning calorimetry

Thermal characterization was performed with a TA Instruments Q2000. Granulate was placed in Tzero pans and tested in a nitrogen atmosphere with a heating/cooling rate of 20 K/min unless otherwise stated. The samples weighted between 5 and 10 mg. Data analysis was performed in TA Universal Analysis (TA Instruments, New Castle, DE) with the built-in tools. The baseline was linearly extrapolated above/below peaks.

Dynamic mechanical analysis

Thermo-mechanical analysis was performed with a TA Instruments DMA 850 on piston injection molded samples of thickness around 3 mm, width roughly 10 mm, and cut to a length of 60 mm. A dual-cantilever geometry was used, and tests were performed using a frequency of 1 Hz, strain amplitude of 0.1 % to ensure the linear viscoelastic region was probed, and a heating rate of 2 °C/min from -40 °C up to 120 °C. Data analysis was performed in TRIOS software (TA Instruments, New Castle, DE) with built-in data analysis tools.

Impact testing

Unnotched Izod impact tests were performed on an Instron (Norwood, MA) CEAST 9050 impact tester equipped with a DAS 8000 Junior data-acquisition system, using a 50 J Izod pendulum hammer. Specimens were rectangular and obtained by piston injection molding as described earlier. The reported data are based on ten repetitions as prescribed by the ISO 180 standard.

Tensile testing

Uniaxial tensile tests were performed with a crosshead speed of 50 mm/min on an Instron 5568 tensile testing machine with a 50 kN load cell. An extensometer was mounted on the ASTM D638 type IV specimens obtained by piston injection molding,

and a 0.2 MPa preload was applied before starting the test. The reported data are based on five repetitions as prescribed by the ASTM D638 standard.

3.4   Molecular Dynamics Simulations

Molecular models

The building and simulation of the molecular models was performed using the Materials Studio (Accelrys Software Inc., v. 6.0.0) software. Isotactic PP and PET molecules were constructed in a head-to-tail configuration using the polymer builder tool and subsequently a 5000 step geometry optimization (convergence tolerance 0.001 kcal/mol and 0.5 kcal/mol/Å for energy and force, respectively) with the Smart algorithm was carried out using the Forcite module. The Smart algorithm combines steepest descent, Newton-Raphson and quasi-Newton methods sequentially, thus allowing efficient and accurate energy minimization. Forcite is a molecular mechanics tool and hence uses force fields for calculations of interactions. In all simulations the COMPASS forcefield [56], optimized for the prediction of condensend-phase properties of a broad range of molecules and polymers [71], was used. Thus, to compute interactions during geometry optimization, the Ewald summation method was used with an accuracy of 0.001 kcal/mol for electrostatic interactions, and an atom-based summation was used for van der Waals interactions with a 12.5 Å cutoff distance and cubic spline truncation over 1 Å.

For the construction of PP-g-MAH, the site for grafting of the maleic anhydride (MAH) on the PP chain was chosen at random. The MAH-content was 5 wt % based on a molecular weight of 98.06 g/mol for MAH [72], and it was the minimum amount possible to attach. The formation of the PP-g-PET copolymer structure was based on the mechanism proposed in [73] and in Fig. 2.3 by J. Maris et al. [9]. Here, the MAH-group was opened and covalently attached to the PET backbone. Lastly, correct number of H-atoms and hybridisation of the atoms was checked, and the geometry was optimized. The resulting PP-g-MAH compatibilizer content was 9.7 wt % in the compatibilized PP75/PET25 blend, henceforth denoted as PP/PP-g-PET. It may be noted that the same degree of polymerization (DP) of PP and PET molecules was used in all blends.

Periodic cubic cells were constructed using the Amorphous Cell module with parameters presented in Table 3.2 followed by a geometry optimization until the energy converged. Three different initial periodic cells were constructed for each system (except PP/PP-g-PET which only had one due to time limitations) used for the study of FH interaction parameters.

TABLE 3.2: The parameters used to construct the amorphous cells considered in the molecular dynamics simulations.

Name	PP/PET (wt.%)	PP/PP-g-PET (wt.%)	Number of chains	Initial density[†] (g/cm^3)
PET	0/100	-	9PET	1.33 [74]
PP10/PET90	10.9/89.1	-	1PP/3PET	1.29
PP25/PET75	26.7/73.3	-	3PP/3PET	1.22
PP50/PET50	47.7/52.3	-	5PP/2PET	1.12
PP75/PET25	74.5/25.5	-	8PP/1PET	1.01
PP	100/0	-	9PP	0.9 [75]
PP/PP-g-PET	-	67.8/32.2	8PP/1PP-g-PET	1.01

[†]Linear combination of weight fractions, and assuming density of PP-g-MAH similar to PP.

Simulation procedure

The simulation procedure consisted of equilibration and production runs. After generation and minimization, equilibration was required since the initial structures may still be in a state of relatively high energy. Thus, an annealing procedure was employed to allow the molecules to overcome torsional energy barriers and prevent the structure from being trapped in a conformation that represents a local minimum. The procedure consisted of five cycles between initial and midcycle temperatures of 298 K and 500 K, respectively. Each half-cycle contained ten temperature steps with 100 dynamics calculations per step, thus resulting in a total of 10 000 steps. The annealing was performed with a time step of 1 fs (used for all simulations) and at constant temperature and volume (NVT-dynamics) at each step. Temperature was controlled with a Nosé-Hoover-Langevin (NHL) thermostat which modifies the friction coefficient in Eq. (2.26) by adding additional stochastic terms. The NHL thermostat was used throughout both equilibration and production runs for temperature control, and assuming ergodicity it samples the correct (canonical) ensemble [16]. Initial velocities were random and drawn from a temperature-dependent Gaussian distribution.

After the annealing procedure, further equilibration consisted of 50 ps NVT-dynamics at 298 K to stabilise the temperature before performing isothermal-isobaric ensemble (NPT) simulations at 298 K and 0.0001 GPa (unless otherwise stated) using the Berendsen barostat. This barostat was chosen since it relatively efficiently both approaches the target pressure and equilibrates the system [16]. The duration of the NPT-dynamics varied between the systems and was determined based on the profiles of e.g. density and energy reaching a plateau; this is illustrated with one of the PP10/PET90 blend structures in Fig. B.1. After this equilibration procedure, two different paths were followed depending on the task.

Firstly, for the thermodynamic miscibility studies and radial distribution function analysis, 100 ps NVT-dynamics were performed. Trajectories were saved every 5 ps and the production run consisted of the final 50 ps; these configurations were hence used for the analysis.

Secondly, for the glass transition studies, NPT-dynamics at 600 K and 0.0001 GPa were performed using the Berendsen barostat until the structure was deemed equilibrated as mentioned above. Next, the structure was cooled down in steps of 30 K with 50 ps NVT-dynamics (to stabilize the temperature) and 200 ps NPT-dynamics at 0.0001 GPa using the Andersen barostat (to sample the correct ensemble [16]). This effectively resulted in a cooling rate of 7.2×10^{12} K min^{-1}.

Chapter 4

Results and Discussion

4.1 Processing of PP/PETG Blends

The effect of extrusion temperature on the miscibility and morphology of two PP/PETG blends was investigated by means of polarized light optical microscopy (PLOM), and the obtained micrographs are presented in Fig. 4.1 below.
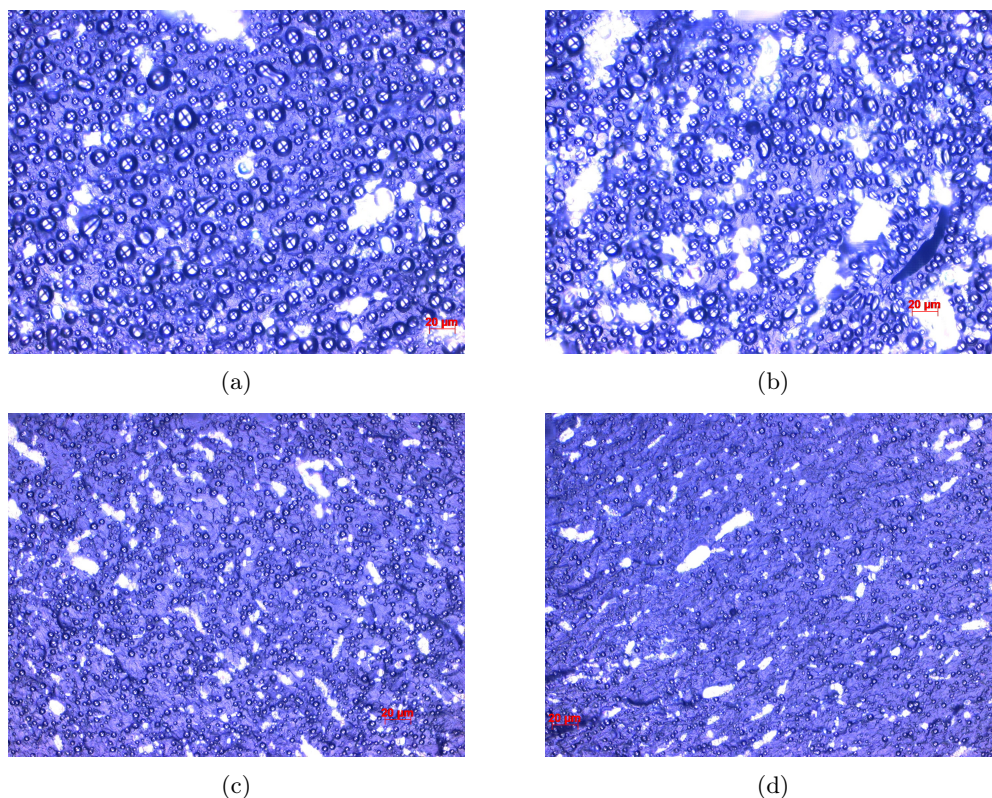
FIGURE 4.1: Surface (parallel to extrusion direction) images obtained with polarized light and 50× magnification of the PP50/PETG50 HT (a), PP50/PETG50 LT (b), PP75/PETG25 HT (c), and PP75/PETG25 LT (d) blends. LT and HT indicate 250 °C and 260 °C, respectively.

One may immediately notice the distinct discrepancy in density and domain size of the dispersed phase (PETG) between 50/50 and 75/25 blends at both investigated temperatures. Moreover, the dispersed phase seems to appear as circular Maltese crosses. Even though the PETG is amorphous and hence does not crystallize significantly (see e.g. Fig. D.1 in Appendix D), M. Kattan et al. [76] showed that, by uniaxially drawing initially amorphous PETG samples at temperatures above the

T_g, it is possible to create a strain-induced crystalline phase. This suggests that the observed spherulites in Fig. 4.1 arise from the drawing of the fibers during extrusion with the subsequent cooling in a water bath freezing-in the structural state. Next, the size of the dispersed phase particles was investigated and appears to be normally distributed (see Fig. 4.2).
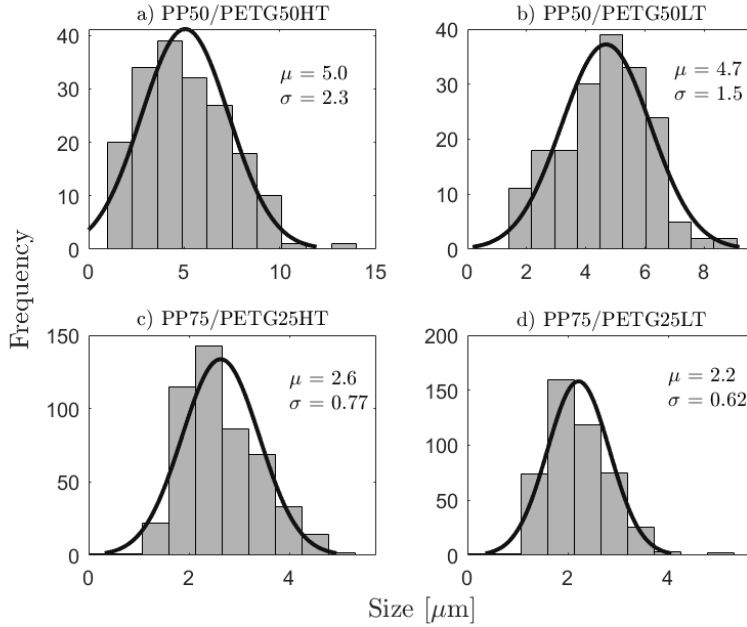
FIGURE 4.2: Particle size distribution with mean value μ and standard deviation σ (both in units of μm) used to fit the normal distribution curve (solid black line).

In general, the mean particle size, assumed to be represented by the radius of the circular Maltese crosses in Fig. 4.1, decreases slightly as the content of dispersed PETG is lowered. Moreover, a mean value for the PP75/PETG25 blend of 2-3 μm seems reasonable when compared with the dispersed phase sizes of 1-2 μm in a PP80/PET20 blend found by M. Heino et al. [77] on extruded strands and $\sim 2.5-2.8$ μm diameter in a PP85/PETG15 blend reported by E. P. A. van Bruggen et al. [10]. Furthermore, as the mean particle size decreases, the standard deviation from the Gaussian distribution fits decreases, meaning a lower polydispersity. This is similar to results observed by B. D. Favis et al. [78] on immiscible polypropylene/polycarbonate blends. This can be explained by considering stress-induced droplet breakup in a liquid matrix. In shear flow a balance exists between shear forces and interfacial forces, the former deforming and breaking up droplets while the latter opposes breakup. By considering the droplet and matrix to be Newtonian liquids, one defines the capillary number

$$Ca \equiv \frac{\dot{\gamma}\eta_m D}{2\Gamma}, \tag{4.1}$$

where $\dot{\gamma}$ is the shear rate, η_m the matrix phase viscosity, D the droplet diameter, and Γ the interfacial tension [79]. As droplets are deformed and become progressively smaller due to breakup, the interfacial tension becomes more significant and eventually balances the viscous forces. Hence, below some critical Ca_{crit} the droplets remain stable. Thus the polydispersity can be expected to decrease with droplet size.
Regarding the dispersed particle size as a function of processing temperature it is

not possible to draw a definite conclusion due to the significant overlap of standard deviations. However, E. P. A. van Bruggen et al. [10] reported from scanning electron microscopy-images on their PP85/PETG15 blend a slight increase in mean particle diameter from 2.54 μm to 2.77 μm as the processing temperature was increased from 250 °C to 300 °C. However, the standard deviations were of similar magnitude or even comparable to the mean value, thus questioning the significance of the observed increase. Hence, from the above analysis it is not possible to conclude on the relation between investigated processing temperatures and blend miscibility.

Rheological frequency-sweep measurements of the PP/PETG blends were performed at the investigated processing temperatures and are presented in Fig. 4.3 along with the pure components. Furthermore, in Fig. 4.4 the blend behaviour at both investigated temperatures are presented and compared in a more narrow data range.
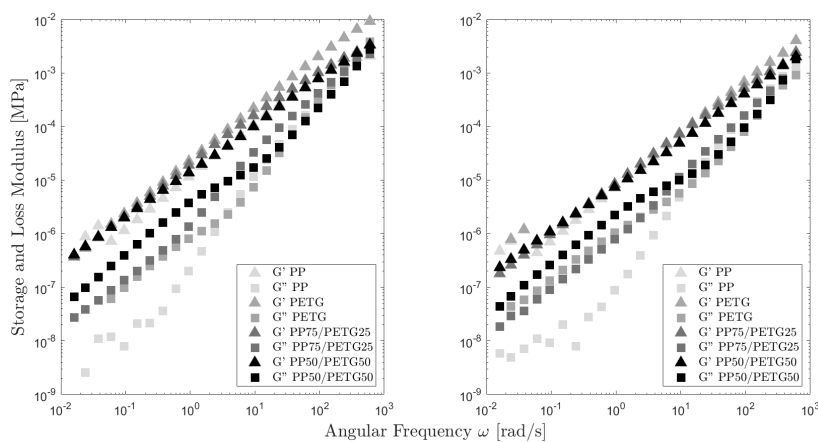
FIGURE 4.3: Frequency-sweep data of PP, PETG, PP75/PETG25 and PP50/PETG50 showing storage (G') and loss (G") moduli at 250 °C (left), and 260 °C (right).
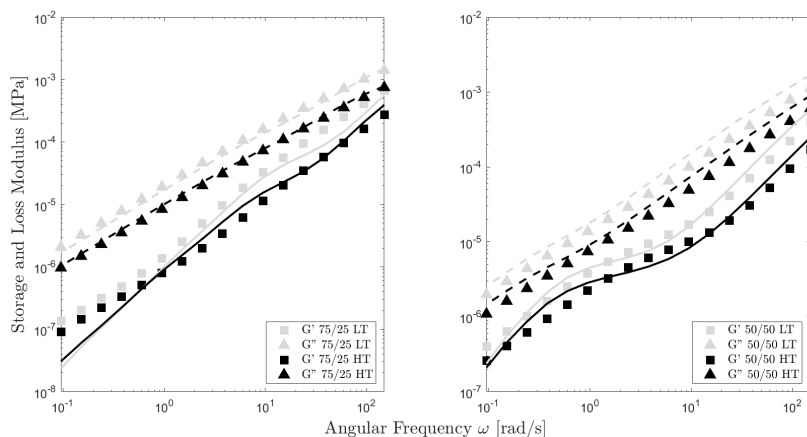
FIGURE 4.4: Frequency-sweep data of PP75/PETG LT and HT (left), and PP50/PETG50 LT and HT (right) showing storage (G') and loss (G") moduli. Symbols: experimental data. Solid lines: Palierne model predictions, best fit to the experimental data using an interfacial tension of 12.1 mN/m between PP and PET [80].

In Fig. 4.3 the noise in the data for PP might be due to a low signal. Furthermore, on comparing PP and PETG it appears the latter exhibits a slightly more elastic behaviour at low frequencies, i.e. terminal behaviour departing from the typical $G' \propto$

ω^2 ($\omega \to 0$) as seen in the PP. This behaviour of PETG is e.g. observed in [81], albeit at a lower temperature. Here it is speculated to be due to entanglements in the melt. Moreover, it is seen from Fig. 4.3 that the blend rheology at low frequencies is relatively similar to that of PETG, even at low concentrations of PETG. A similar trend for blends of poly(lactic acid)/polyamide 11 (PLA/PA11) was observed by F. Walha et al. [82] with low concentrations of PA11 as the dispersed phase.

A distinct feature displayed by the blends is the increase in elasticity at low frequencies ('shoulder'), which is typically observed in immiscible polymer blends with spherical droplets dispersed in the continuous matrix phase [83–85]. It is attributed to the shape relaxation of the dispersed phase droplets with the interfacial tension as the driving force [84]. Furthermore, it is observed that the 'shoulder' is substantially more pronounced in the 50/50 blend at both temperatures. Assuming the same interfacial tension in both blends, the shape relaxation time can be shown to be proportional to the droplet radius. Thus, since larger droplets require more time to relax, the relaxation shoulder is also shifted to lower frequencies with larger droplet radii [36]. Especially for the blends at low temperature (LT) a shift in the 'shoulder' to higher frequencies with decreasing dispersed phase content can be noticed, in agreement with findings from the PLOM study. It should be noted, however, that immiscible blends may also exhibit a co-continuous morphology in a wide concentration range [86]. The co-continuous structure is characteristic of strongly interpenetrating domains of both blend components. However, the rheological behaviour of co-continuous blends is different from droplet-matrix blends in that the former does not display a terminal behaviour; the high degree of inter-connectivity associated with the resulting network structure prevents terminal flow. Hence, a broad range of characteristic lengths of domains, and thus different relaxation times, endow the co-continuous blends with a power law behaviour, $G' \propto \omega^{\alpha}$ ($\alpha < 1$), at low frequencies [87, 88]. Regarding the PP/PETG blends investigated in this project, the clear 'shoulder' present in the 50/50 blend suggests a droplet-matrix structure of this melt. Furthermore, X. Zhang et al. [89] investigated a PP70/PETG30 blend, and both SEM and melt rheometry studies suggested a droplet-matrix structure.

In order to quantitatively investigate the influence of processing conditions on the melt miscibility, the blends are treated as undiluted suspensions of viscoelastic droplets in a viscoelastic fluid. The complex shear modulus of the blend G_b^* under small-amplitude deformations can then be described by the Palierne-model [90]

$$G_b^*(\omega) = G_m^*(\omega) \frac{1 + 3\sum_i \phi_i H_i(\omega)}{1 - 2\sum_i \phi_i H_i(\omega)}, \qquad (4.2)$$

where the subscript m denotes the matrix phase, ϕ is a volume fraction, and the sum extends over the number of differently sized dispersed-phase particles with

$$H_i(\omega) = \frac{4\frac{\Gamma}{R_i}\left[2G_m^*(\omega) + 5G_i^*(\omega)\right] + \left[G_i^*(\omega) - G_m^*(\omega)\right]\left[16G_m^*(\omega) + 19G_i^*(\omega)\right]}{40\frac{\Gamma}{R_i}\left[G_m^*(\omega) + G_i^*(\omega)\right] + \left[2G_i^*(\omega) + 3G_m^*(\omega)\right]\left[16G_m^*(\omega) + 19G_i^*(\omega)\right]}. \qquad (4.3)$$

Again, Γ is an interfacial tension, while G_i^* is the complex modulus of the dispersed phase. It can be noted that Eq. (4.2) contains no empirical parameters. To further simplify the analysis, a uniform particle size distribution is assumed, i.e. $R_i = R$.

Thus, finding R requires knowledge about the interfacial tension between the matrix and dispersed phases. J.-C. Lepers et al. [80] found the interfacial tension between PP and PET to be 12.1 mN/m at 280 °C using the breaking thread method with PET as the thread. Although PET and PETG are chemically different and interfacial tension typically decreases with temperature in several polymer blends [91, 92], the above-mentioned value is assumed to apply for both blends and temperatures for the purposes of this analysis. Moreover, according to Eq. (4.2) the complex moduli of the pure components must be known. However, due to the compounding of the blend components at elevated temperatures, processing-induced degradation of the components will occur as shown by R. Klitkou [75] for multiple extrusions of PP and found in Fig. 4.5 below.
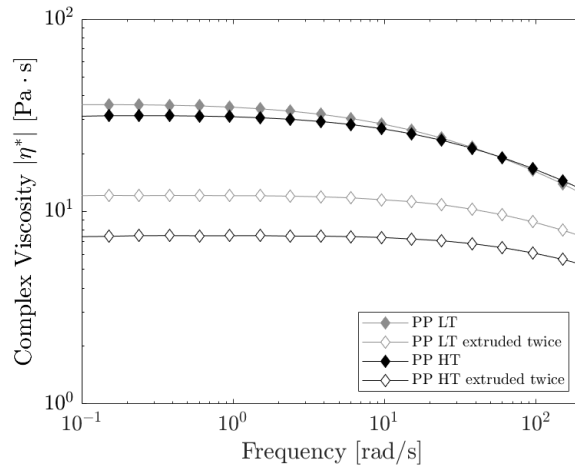
FIGURE 4.5: Complex viscosity of virgin and twice extruded polypropylene at temperatures of 250 °C (LT) and 260 °C (HT) used to investigate the PP/PETG blends. Lines are a guide to the eye.

This lowering of the Newtonian plateau is consistent with a decrease in molecular weight due to thermal and mechanical degradation of the polymer chains. This effect is significant and accounted for in Eqs. (4.2) and (4.3) to obtain the model predictions in Fig. 4.4. The values of R obtained by nonlinear least-squares optimization are presented in Table 4.1.

TABLE 4.1: Values of droplet radii R used in the Palierne-model.

Blend	Temperature (°C)	R (μm)
PP75/PETG25	250	66
PP75/PETG25	260	170
PP50/PETG50	250	530
PP50/PETG50	260	1260

Firstly, the prediction of the monodisperse Palierne-model in Fig. 4.4 does not fit the moduli well, especially the storage modulus of the PP75/PETG25 blend. Furthermore, the behaviour of the PP75/PETG25 blend appears to be quite influenced by the behaviour of pure PETG at low frequencies. Yet, the weight of the PETG in the Palierne model is relatively modest with its volume fraction of roughly 0.2 assuming a simple rule of mixtures applies. This is speculated to partially contribute to the relatively large deviation between model and data at low frequencies.

The discrepancies between model and data at low frequencies could also be due to a droplet size distribution as observed in Fig. 4.2 and, along with steric interactions, as suggested by S. Tyagi et al. [93] for polypropylene/ethylene vinyl acetate blends. As mentioned by I. Vinckier et al. [83] the substitution of a distribution of radii by the volumetric mean radius should have no significant effect on the prediction of the Palierne model if the polydispersity index (PDI) < 2. As shown by S. V. Canevarolo [94], the polydispersity of PP decreased with number of extrusion cycles which is also supported by findings in Fig. 4.5 due to later onset of shear-thinning behaviour. Matters are further complicated by the fact that polydispersity increases with increasing content of dispersed phase [6, 37, 95]. Also, blend composition can affect the degradative behaviour of a polymer blend, and thus the degradation behaviour of the components in the blend may differ from that observed in the pure systems; for instance due to interactions among different species in the blends during degradation [96]. This will influence the ability of the Palierne model to capture the blend behaviour since it relies on representative pure component behaviour. However, even though the processing conditions were shown to have a significant effect on the rheology of the pure components, the effect of degradation in blend versus pure components was not investigated. Thus, whether the pure component polydispersities were below a value of two is not known, making it difficult to conclude further about the observed discrepancies in observed dynamic behaviour and Palierne model predictions.

Lastly, the predicted values of dispersed phase radii in Table 4.1 are relatively large compared to typical values of about $1\,\mu$m in polymer blends [37]. The radii appear to increase by a factor 2-3 when raising the temperature 10 °C in both blends. The fact that the dispersed phases are larger than or comparable to the gap height of 1 mm seems doubtful but would also yield the Palierne analysis untrustworthy since the droplets will likely loose their spherical shape. Yet, the trend appears to be larger droplet radii in the PP50/PETG50 blends in agreement with the discussion above. However, it is not possible to directly compare the magnitude of the radii predicted by the Palierne model with those obtained from the extruded strands in Fig. 4.2 due to coarsening of the microstructure during sample equilibration. This coarsening is exemplified by the melt morphology of the PP50/PETG50 LT blend in Fig. 4.6 measured at 250 °C over the course of one hour. The melt morphology development of the remaining blends (PP50/PETG50 HT, and PP75/PETG25 HT and LT) can be found in Appendix F, and their calculated number (D_N) and volume (D_V) average particle diameters and their ratio $\left(\mathrm{PDI} = \frac{D_V}{D_N}\right)$ are presented in Table 4.2. When comparing the Palierne model predictions with volume average diameter, representative of the predictions of the Palierne model [83, 97], the Palierne model greatly overestimates dispersed phase particle dimensions compared to the observed ones.

TABLE 4.2: Number ($D_{N,x}$) and volume ($D_{V,x}$) average dispersed phase equivalent particle diameters[†], and polydispersity index (PDI_x) after x minutes.

Blend[‡]	$D_{N,15}$	$D_{N,30}$	$D_{N,45}$	$D_{N,60}$	$D_{V,15}$	$D_{V,30}$	$D_{V,45}$	$D_{V,60}$	PDI_{15}	PDI_{30}	PDI_{45}	PDI_{60}
50/50HT	14.6	13.6	17.9	17.1	56.4	69.1	78.4	84.9	3.9	5.1	4.4	5.0
75/25HT	8.3	9.3	8.4	8.9	23.1	24.6	28.4	33.5	2.8	2.6	3.4	3.8
50/50LT	15.7	14.1	12.8	13.4	40.3	47.2	60.7	67.4	2.6	3.4	4.7	5.0
75/25LT	7.0	8.6	8.5	9.6	10.8	16.1	18.3	19.9	1.5	1.9	2.2	2.1

[†]Assuming dispersed phase particles are circular in the micrographs.

[‡]Numbers indicate weight fractions of PP/PETG, and LT =250 °C and HT =260 °C.
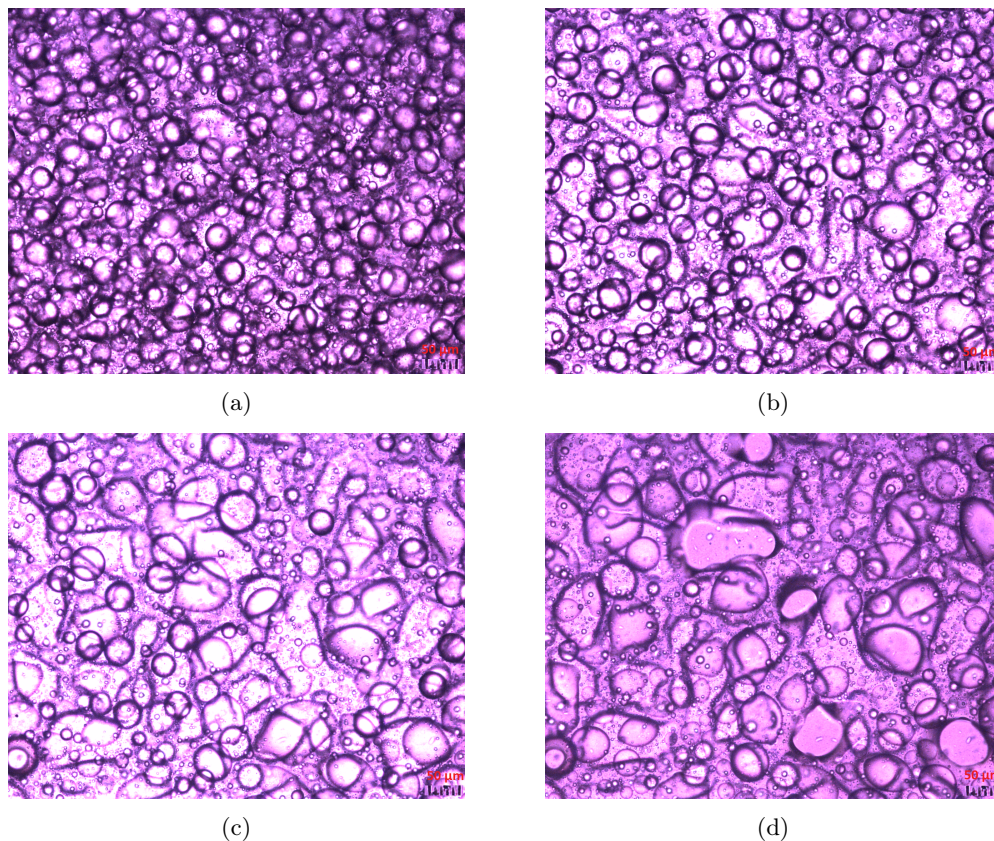
FIGURE 4.6: Polarized light images of the PP50/PETG50 LT blend with ×10 magnification at 250 °C after 15 min (a), 30 min (b), 45 min (c), and 60 min (d). The measurements were performed under static conditions.

Moreover, a coarsening of the dispersed phase is seen in all the micrographs, and from Table 4.2 it is seen that the D_V and PDI generally increase with time. Furthermore, as seen in Fig. F.4 the cube of D_V seems to increase linearly with time, except in case of the PP75/PETG25 HT blend. The linear increase in droplet volume with time is associated with Ostwald ripening [83], i.e. the diffusion of dispersed phase molecules from the continuous phase to the droplet phase. The exception could be due to additional mechanisms contributing to the coarsening such as coalescence. Yet, according to Ostwald ripening larger droplets will grow on the expense of smaller ones as seen in the micrographs. Moreover, the consequence of Ostwald ripening is a broadening of the droplet size distribution, in agreement with the generally observed increase in PDI with time in Table 4.2. The increase in droplet size with time is in agreement also with data reported in the literature; for instance, A. Argoud et al. [98] found that the growth of domain sizes in non-compatibilized polyamide 6/HDPE blends increased significantly from 10 μm to 140 μm in 15 minutes under static annealing conditions at 290 °C. Moreover, from rheological measurements of the complex viscosities of the pure components in Figs. E.1 and E.2 it is seen that the viscosity ratio $\eta_r = \eta_d/\eta_m$ between dispersed phase 'd' and matrix 'm' is > 1; this leads to a tendency for dispersed phase coalescence [99], in agreement with the above-mentioned findings.

However, the measured values of PDI > 2 cast doubt on the assumption of uniform particle size distribution used in the Palierne model analysis. Moreover, the investigated blends were non-dilute which could cause droplet-droplet interactions that are not adequately captured by the Palierne model. These factors may contribute to the

large deviation of predicted droplet diameters in Table 4.1 and measured diameters in Table 4.2, especially for the PP50/PETG50 blends.

4.2 Compatibilized Blends

The effect of adding various amounts of Acti-Tech 09MA13 (AT) compatibilizer to the rPPC/PET blend was investigated by means of PLOM. The results obtained with two different magnifications are presented in Fig. 4.7.

(a) rPPC/PET/0   (b) rPPC/PET/0

(c) rPPC/PET/4   (d) rPPC/PET/4

(e) rPPC/PET/6   (f) rPPC/PET/6
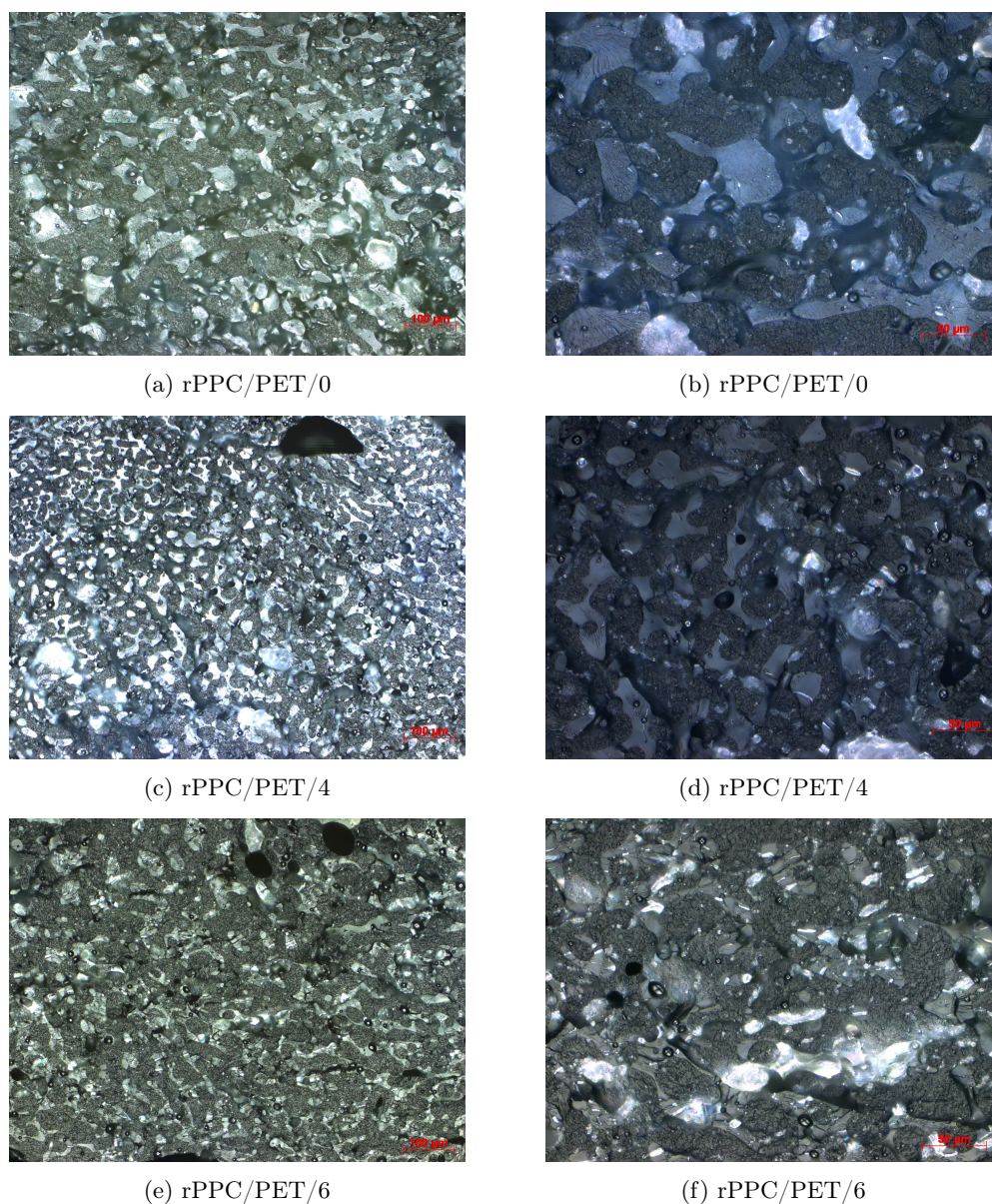
FIGURE 4.7: Surface (parallel to extrusion direction) images of rPPC/PET/X pellets using polarized light with 20× (left) and 50× (right) magnification.

It is observed, that the typical domain size decreases and the dispersion improves as compatibilizer is added to the blend. However, it is difficult to distinguish one domain from another in e.g. the rPPC/PET/6 blend in Fig. 4.7f. Yet, a rough image analysis finds the order of average domain sizes to be rPPC/PET/0 ($\sim 1000\,\mu\mathrm{m}^2$) >

rPPC/PET/6 ($\sim 700\,\mu\text{m}^2$) > rPPC/PET/4 ($\sim 500\,\mu\text{m}^2$). This agrees well with findings by e.g. L. Li et al. [99] who investigated the compatibilizing effect of ethylene-propylene copolymer in PP/PE blends. Here the authors found a decrease in the size of the dispersed PE-phase with addition of copolymer up to a certain extent. Also, M. Akbari et al. [44] studied a PP30/PET70 blend and found an improved dispersion upon addition of up to 10 wt.% PP-g-MAH compatibilizer.

The rPPC/PET-blends were further analyzed by Fourier transform infrared spectroscopy (FT-IR) to investigate the effect of compatibilizer on the vibrational spectrum. In general, if the blend components are immiscible the absorption spectrum of the blend will be the sum of the component spectra. On the other hand, for miscible or partially miscible blends, intermolecular interactions will perturb bonds between atoms, thus resulting in changes of peak position and shape [100–102]. The obtained spectra are shown in Fig. 4.8a, and a narrow part of the obtained spectra is presented in Fig. 4.8b. The spectra of the three blends in Fig. 4.8a appear similar with no indication of peak shifts, suggesting immiscibility of the blend components. The peak around $1779\,\text{cm}^{-1}$ clearly observed in Fig. 4.8b is attributed to the symmetric C=O stretching of an anhydride [44, 103]. Its absence in the blends indicates a chemical reaction between the terminal ester and/or hydroxyl groups of PET with maleic anhydride (MAH) [104, 105]. This agrees well with the PLOM findings in Fig. 4.7, with improved dispersion being facilitated by the compatibilizer.
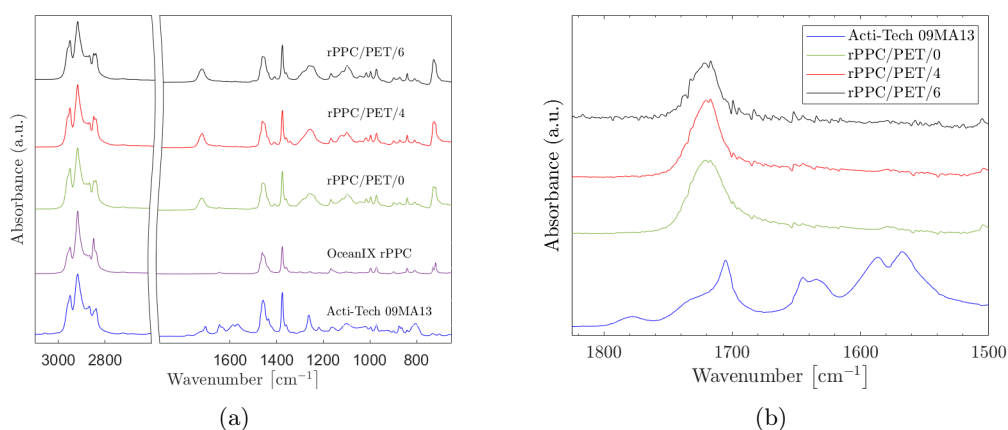
FIGURE 4.8: Fourier transform infrared spectra of (a) the blends rPPC/PET/0, rPPC/PET/4, and rPPC/PET/6, as well as the compatibilizer Acti-Tech 09MA13 and OceanIX rPPC (equivalent PP/HDPE composition as in rPPC and supplied by Plastix). (b) Same as left but without the OceanIX rPPC. The spectra were normalized to the maximum intensity at $2917\,\text{cm}^{-1}$, attributed to asymmetric CH$_2$ stretch [106], to facilitate the comparison.

The thermal characteristics of the rPPC/PET blends were studied by DSC, and the results are presented in Figs. 4.9a, 4.9b and 4.10. Three crystallization peaks observed in Fig. 4.9a have been attributed to PET, PP and HDPE in order of descending temperature. It must be noted that some polymers may exhibit transcrystallinity, a phenomenon resulting from the nucleating ability of the pan surface, which can result in exothermic peaks with a 'shoulder' as shown by N. Billon et al. [107] for HDPE. However, H. P. Blom et al. [108] studied PP/HDPE blends by DSC and noted that for their blends with a ratio of 70/30 wt.% PP/HDPE, the observed double peak was due to crystallization of the PP and HDPE; the larger peak was attributed to HDPE due to its relatively larger heat of fusion compared to PP.
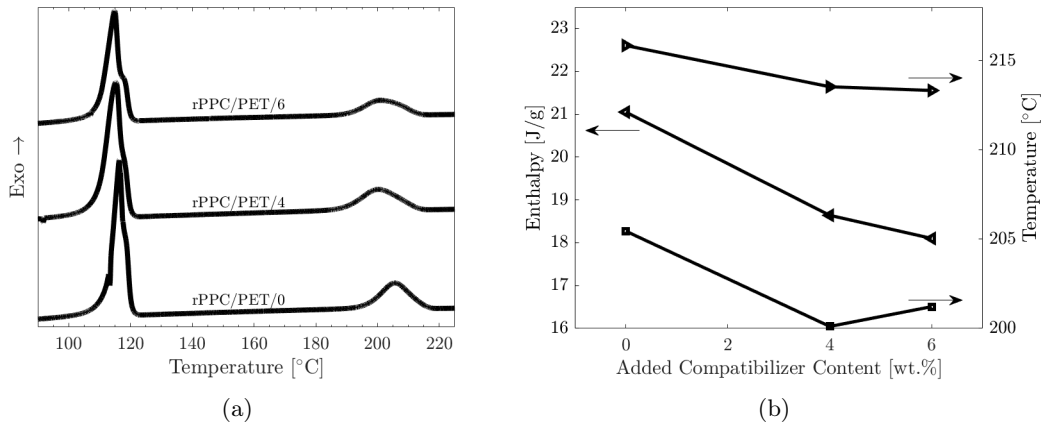
FIGURE 4.9: DSC thermogram of crystallization processes in the three blends (a), and enthalpy, peak $\left(T_c^{peak}\right)$ and onset $\left(T_c^{onset}\right)$ temperatures of the PET crystallization process as a function of the added compatibilizer content (b).

Similar results were reported by C. Aumnate et al. [109]. Furthermore, it can be noticed that the crystallization temperatures (peak and onset) of the PP and HDPE, i.e. the multimodal peak in the interval 100-120 °C, do not appear significantly affected by the presence of the compatibilizer. Yet, a slight shift to lower temperatures ($\sim 1 - 1.5$ °C) of especially the highest peak (attributed to HDPE) can be noticed. A similar effect was observed by M. Kuzmanovic et al. [110] in their PP/PET composites using a similar Acti-Tech compatibilizer as in this study. Their explanation is based on the PET phase acting as a nucleating agent for the PP matrix. However, the added compatibilizer will cover the PET phase to some degree, thus inhibiting the nucleating effect of PET on the PP phase. Moreover, a slight broadening of the rPPC crystallization exotherm is observed in Fig. 4.9a upon addition of compatibilizer. A similar broadening of PP crystallization peaks, as well as shift of peak crystallization temperature to lower values, in compatibilized PP/PET blends was observed by M. Lima et al. [111] using various compatibilizers, e.g. one based on glycidyl methacrylate. They attributed their findings to a slower crystallization process due to affinity of their compatibilizers to the PP domains. Since the Vistamaxx-backbone of the AT compatibilizer in this study is based on ethylene and propylene repeat units, it is miscibile with the matrix of the blends in this study [110].

TABLE 4.3: Values of crystallization (ΔH_c) and melting (ΔH_m) enthalpies, as well as degree of crystallinity (DOC), for PET.

Blend	ΔH_c^{PET} (J/g)	ΔH_m^{PET} (J/g)	$DOC_{PET}^{\dagger}$ (%)
rPPC/PET/0	21.1	18.8	67.1
rPPC/PET/4	18.6	17.6	65.5
rPPC/PET/6	18.1	16.9	64.2

†For the fixed PET/rPPC ratio the PET weight fractions w_i (see Eq. (4.4)) used are 0.2, 0.192 and 0.188 with 0, 4 and 6 wt.% added compatibilizer, respectively. These values hence overestimate the actual PET weight fraction since the original ~ 6 wt.% compatibilizer are not accounted for.

As seen in both Figs. 4.9a and 4.9b, the peak and onset crystallization temperatures of the dispersed PET phase are shifted to lower temperatures with the addition of compatibilizer. A similar trend was found by Y. Tao et al. [105] and can be explained

based on the previously mentioned role of the MAH functional group of the AT compatibilizer. The formation of the PET-g-AT copolymer results in a lowered mobility of the PET polymer chains and hence impedes the crystallization of the PET. This results in a decrease in both crystallization temperature and enthalpy.

The melting behaviours of the three blends are presented in Fig. 4.10.
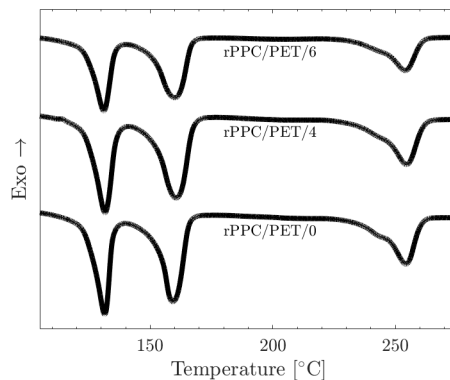
FIGURE 4.10: DSC thermogram of melting processes in the three blends.

It is difficult to quantitatively investigate the enthalpies associated with PP and HDPE in the blends due to overlap between the respective melting peaks, as well as a PET glass transition prior to the HDPE melting peak resulting in an ill-defined baseline. Yet, by analyzing the melting of the PET phase in the interval from roughly 220-265 °C, the enthalpies of fusion in Table 4.3 follow the order rPPC/PET/0 > rPPC/PET/4 > rPPC/PET/6. A similar trend was found by L. M. G. Araujo et al. [112] for PP/PET blends compatibilized by a maleic anhydride-functionalized elastomer SEBS-g-MAH. Furthermore, the degree of crystallinity (DOC) of blend component i is related to the enthalpy of fusion (ΔH_m^i) as [110]

$$DOC_i = \frac{\Delta H_m^i}{\Delta H_m^\circ \cdot w_i} \cdot 100\%, \tag{4.4}$$

where w_i is weight fraction of blend component i, and ΔH_m° is 140 J/g for 100 % crystalline PET [112]. The results in Table 4.3 indicate a decrease in the DOC of the PET phase with increasing added compatibilizer content. This agrees with both the above discussion on decreased mobility of PET in PET-g-AT copolymers, as well as with findings by C. P. Papadopoulou et al. [21] who observed a decrease in PET crystallinity in PET/PP blends compatibilized by SEBS-g-MAH.

The effect of added compatibilizer content on the molecular transitions in the blends was investigated by DMA. The results from the temperature ramps are presented in Fig. 4.11. It is from E' in Fig. 4.11a that increasing compatibilizer content provides the blend with an additional elasticity at low to moderate temperatures. This suggests an increased interfacial interaction between the component phases causing improved stress transfer [113]. It can further be observed, that E' of the rPPC/PET/0 blend becomes larger than that of the rPPC/PET/4 and rPPC/PET/6 blends. The thermogram of the AT compatibilizer in Fig. D.2 suggests melting of crystalline regions of the compatibilizer in the range 40 to 100 °C. This can be speculated to cause the weakened elastic response in Fig. 4.11a of the rPPC/PET/4 and rPPC/PET/6 blends relative to the rPPC/PET/0 blend. Furthermore, from Fig. 4.11b the loss

moduli generally increase in the rPPC/PET/4 and rPPC/PET/6 blends compared to the rPPC/PET/0 blend, suggesting improved ability to dissipate energy. Both aforementioned observations were also reported by M. S. Lima et al. [111] for PP/PET blends using various compatibilizers.

(a)

(b)

(c)
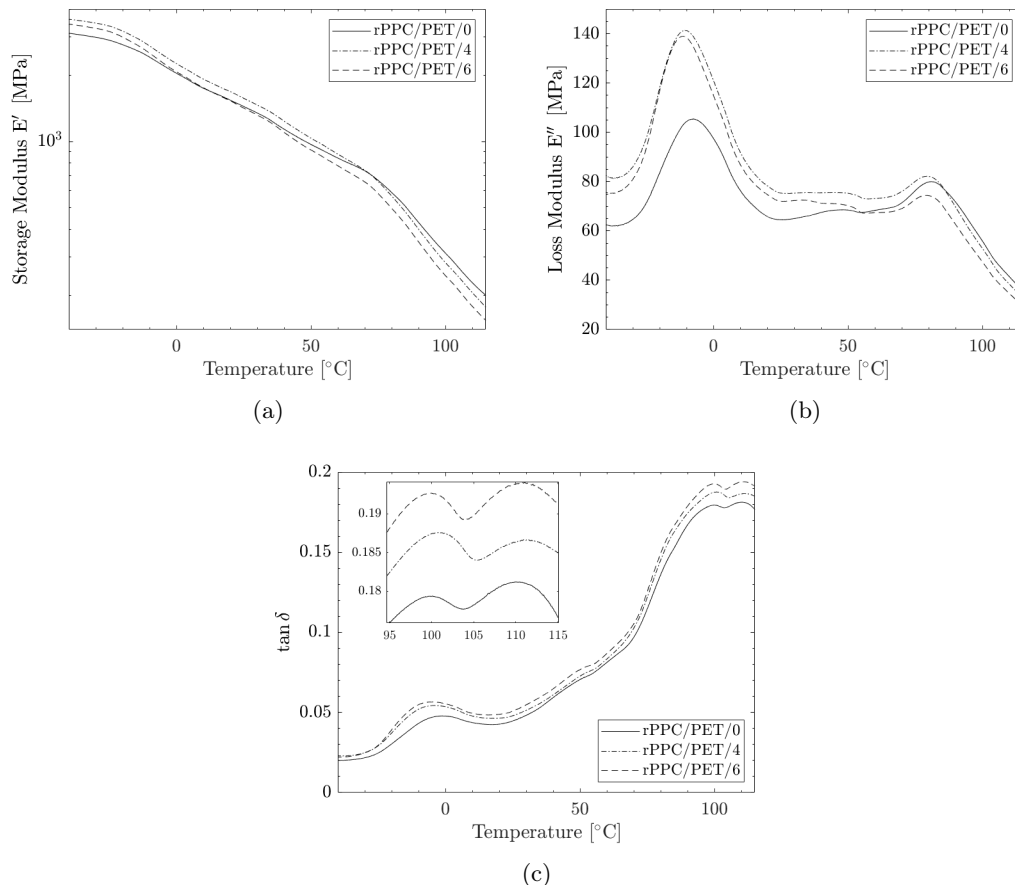
FIGURE 4.11: The storage moduli (a), loss moduli (b), and loss tangents (c) for the rPPC/PET blends with various added compatibilizer contents.

Due to the sensitivity of DMA to macroscopic and molecular relaxation processes [114], it is interesting to investigate the influence of added compatibilizer content on the glass transition temperatures of the various components. Relevant data extracted from Fig. 4.11 is thus shown in Table 4.4. It should be noted, that the peak around 100 °C shown in the inset of Fig. 4.11c was attributed to $T_{g,PET}$ based on both values reported in the literature [111] and from the response of OceanIX rPPC (equivalent to rPPC) presented in Fig. G.1. The peak between −5 °C and 0 °C in $\tan\delta$ is attributed to PP [111] while that of HDPE is outside the measured interval [115]. It is observed from Table 4.4 that $T_{g,PP}$ from loss modulus and $\tan\delta$ peaks shifts relatively significantly to lower temperatures with increasing compatibilizer content. This contrasts findings by M. S. Lima et al. [111] and Y. Zhu et al. [116] who found no significant change of $T_{g,PP}$ in PP/PET blends with e.g. MAH- or epoxy-based compatibilizers. The observed decrease in the $T_{g,PP}$ may be speculated to be facilitated by an increased free volume as a result of the addition of compatibilizer with relatively bulky MAH side groups. The increased free volume will provide a greater mobility to the PP phase in between the glassy PET, thus lowering $T_{g,PP}$. On the other hand, as mentioned in the discussion of the DSC results, the Vistamaxx-backbone of AT is miscible with

the rPPC and may be dispersed in the PP matrix. This would modify the PP matrix properties depending on the degree of dispersion. This would likely shift $T_{g,PP}$ towards that of AT. The $T_{g,PP}$ from the onset points of the E'-curve do not appear significantly affected by the added compatibilizer content.

TABLE 4.4: Glass transition temperatures (T_g) of the PP and PET.

Blend	Storage modulus E'[†]		Loss modulus E"[‡]		$\tan\delta$[‡]	
	$T_{g,PP}$	$T_{g,PET}$	$T_{g,PP}$	$T_{g,PET}$	$T_{g,PP}$	$T_{g,PET}$
rPPC/PET/0	−25.6 °C	71.5 °C	−7.5 °C	81.2 °C	−1.4 °C	99.6 °C
rPPC/PET/4	−25.8 °C	71.9 °C	−10.5 °C	79.5 °C	−4.5 °C	101.0 °C
rPPC/PET/6	−25.1 °C	71.7 °C	−11.2 °C	79.1 °C	−5.9 °C	100.0 °C

[†]Glass transition temperature determined by onset point.

[‡]Glass transition temperature determined from coordinates of respective peaks.

For the PET, the results in Table 4.4 for E' do not indicate a change in $T_{g,PET}$ with added compatibilizer content, and neither does it seem to be the case for the $T_{g,PET}$ from $\tan\delta$. On the other hand, the $T_{g,PET}$ from E" appears to decrease slightly with increasing compatibilizer content, in agreement with data reported in the literature on PP/PET blends containing MAH- and glycidyl methacrylate (GMA)-based compatibilizers [77, 116]. The authors attribute the decrease in $T_{g,PET}$ to enhanced interactions between the discrete phases facilitated by their compatibilizers. This is in agreement with the role of AT in migrating to the PP-PET interface to improve adhesion between the phases.

Mechanical properties of the blends were studied by tensile and impact testing, and the results are presented in Fig. 4.12. It is seen that the impact strength of the blend is improved with the addition of compatibilizer. Similar observations are reported for other PP/PET blends using commercial or similar compatibilizers to this study [110, 117], SEBS-g-MAH [77, 112], SEBS-g-GMA [77], PP-g-MAH [116], and PP-g-GMA [118]. The explanation for the improved impact strength can be understood in terms of an improved stress transfer between matrix and dispersed phase due to reduced dispersed phase size, improved dispersion, and enhanced interface adhesion [110, 112, 119]. This agrees well with 1) the findings from the PLOM study indicating improved dispersion of the blend components, 2) the aforementioned formation of PET-g-AT facilitating improved adhesion between dispersed and matrix phases, and 3) the elastomeric character of the AT backbone [119], which will provide toughness to the blend. Also, unreacted AT dispersed in the matrix phase may act as a nucleating agent and promote a greater number density of spherulite crystals, which would improve the impact strength [110, 120]. However, due to the relatively large standard deviation of the rPPC/PET/6 blend it is difficult to observe a significant improvement by increasing the added compatibilizer content from 4 to 6 wt.%; this effect could be due to saturation of the PET [121, 122].

Results from the tensile tests also indicate an improvement in interface adhesion between PET and matrix material; both elongation at yield and break, as well as yield strength increase when compatibilizer is added relative to the rPPC/PET/0 blend, in agreement with data reported in the literature for compatibilized PP/PET blends [21, 104, 112, 113, 116]. However, the elastic modulus appears relatively unaffected by the addition of compatibilizer when taking into account the overlap of standard deviations. Moreover, some authors [21, 113, 118, 123] also report of an optimum amount of compatibilizer above which the mechanical properties either remain unchanged or deteriorate.
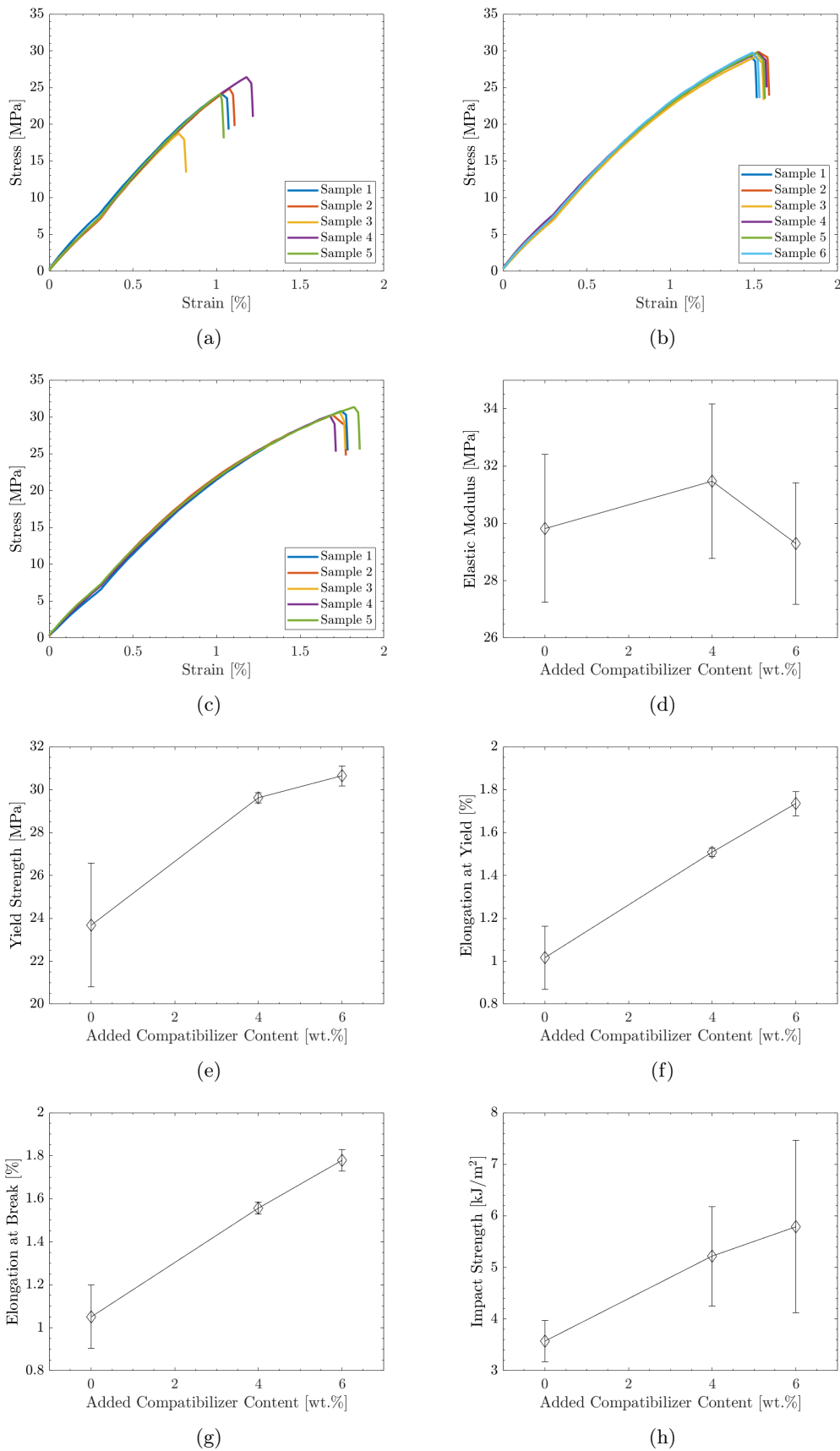
FIGURE 4.12: The measured stress-strain diagrams of the the rPPC/PET/0 (a), rPPC/PET/4 (b), and rPPC/PET/6 (c) blends. Extracted from the stress-strain diagrams are elastic moduli (d), yield strength (e), elongation at yield (f), and elongation at break (g). Impact strengths are shown in (h), and all test specimens exhibited a complete break.

As previously mentioned, the interface between matrix and dispersed phase may become saturated causing dispersion of the compatibilizer in the matrix phase. At relatively high concentrations the typically soft backbone of the compatibilizer might contribute to the reduced strength of the blends [116, 119]. This is, however, not observed for the added compatibilizer contents investigated in this study.

The rheological behaviour of the molten blends was studied at the extrusion temperature of 280 °C. In Fig. 4.13 the complex viscosity of the three blends is presented, while Fig. 4.14 presents the storage and loss moduli of the blends.
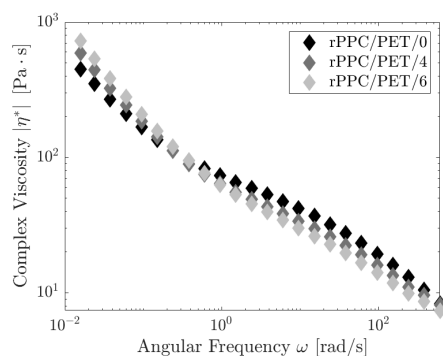
FIGURE 4.13: The complex viscosities of the rPPC/PET/X blends with various added compatibilizer contents.
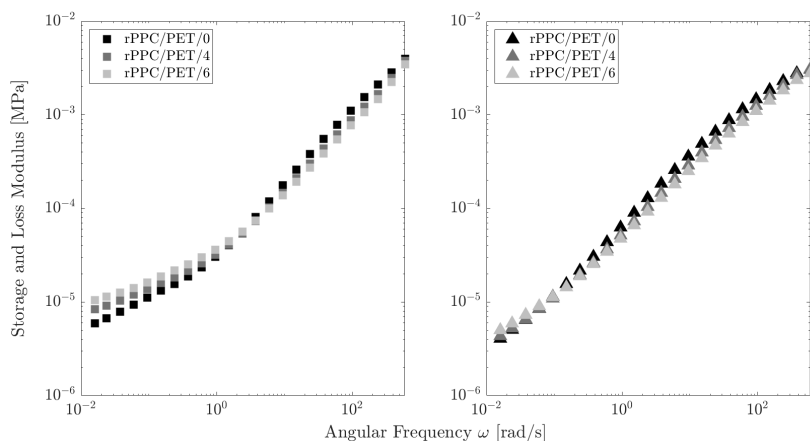
FIGURE 4.14: The storage (left) and loss (right) moduli for the rPPC/PET blends with various added compatibilizer contents.

Firstly, in Fig. 4.13 the absence of a Newtonian plateau is noticed, indicating a highly non-Newtonian behaviour of the blends. Also, with increasing compatibilizer content the shear thinning effect becomes more pronounced. Nevertheless, the increase in complex viscosity with increased compatibilizer content is in agreement with data reported in the literature for both blends with a droplet-matrix morphology [104, 112, 124, 125] and co-continuous blends [126]. It can be understood in terms of the enhanced interfacial adhesion between the immiscible phases of the blends. Also, the previously-mentioned formation of PET-g-AT will increase the MW of PET, thus increasing viscosity and the elastic response. This substantiates the findings from the mechanical tests. The increased elastic response at low frequencies is also observed in Fig. 4.14. The slight decrease in G' with compatibilizer content at high frequencies can be speculated to be due to the soft backbone of AT; this will influence the structural behaviour of the blends at high frequency deformations due to insufficient time for relaxation to occur.

4.3 Molecular Dynamics Simulations

Molecular dynamics simulations (MD) were performed in order to investigate the miscibility of PET and PP. However, since simulating realistic polymer chain lengths is not feasible computationally, it is important to investigate the minimum chain length sufficient to adequately represent the behaviour of the polymer. This is typically done by calculating the solubility parameter (δ) [19, 71] and density [15] as a function of the degree of polymerization (DP). These investigations were performed for the PET and PP in this study, and the results are plotted in Fig. 4.15.
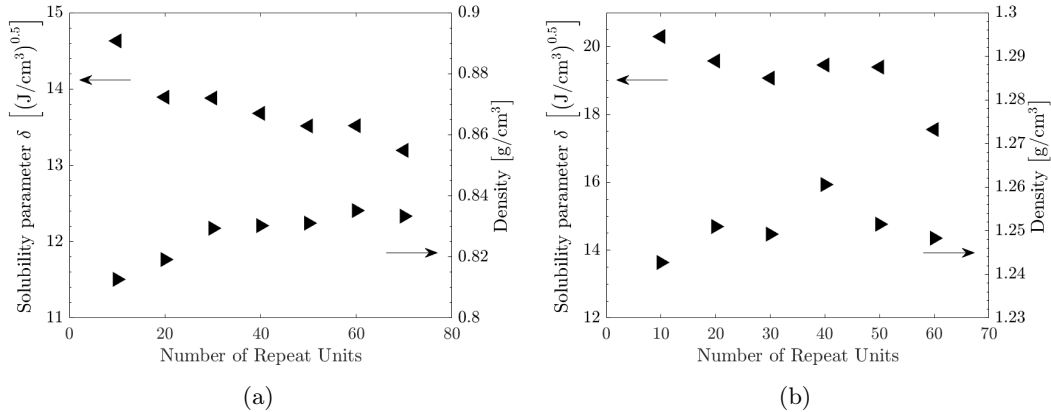
FIGURE 4.15: Solubility parameter (δ) and density of polypropylene (a) and poly(ethylene terephthalate) (b) as a function of number of repeat units found by molecular dynamics simulations. Solubility parameter data was obtained from the last 50 ps of the 100 ps NVT-dynamics after NPT-equilibration, while densities were calculated from the last 50 ps of the NPT-equilibration run at 298 K and 0 bar.

TABLE 4.5: Calculated and experimentally observed solubility parameters (δ) and densities (ρ) for the polymers investigated in this study.

[The ρs are calculated from the last 50 ps NPT-dynamics at 298 K and 0 bar, while δs are calculated from the last 50 ps of additional 100 ps NVT-dynamics at 298 K.]

			MD calculations			Experimental values	
	DP	MW [g/mol]	$\delta \left[\left(\mathrm{J/cm^3}\right)^{0.5}\right]$	$\rho \left[\mathrm{g/cm^3}\right]$		$\delta \left[\left(\mathrm{J/cm^3}\right)^{0.5}\right]$	$\rho \left[\mathrm{g/cm^3}\right]$
PP	50	2104	13.5	0.83		17.3-18.8*	0.9*
PET	30	5765	19.1	1.25		21.9§	1.41*

*Based on data from J. E. Mark [127].

§Based on data from Y.-Z. Wang [128].

It is seen in Fig. 4.15a that the density of PP appears to reach a plateau at about 0.83 g/cm³. This is lower than the initial density of 0.9 g/cm³ used. On the other hand, the solubility parameter of PP appears to continually decrease, similar to observations reported by Y. Fu et al. [129], while being up to 30 % lower than experimentally observed values (see Table 4.5). However, it may be noted that even though the simulations were carried out at 0 bar this is essentially equivalent to 1 bar (experimental conditions) due to the relatively large pressure fluctuations in simulations (see e.g. Fig. B.1e) [130]. Also, a decrease in MW will result in reduced CEDs due to a lower density of interactions, thus leading to lower values of δ [131]. Yet, based on Fig. 4.15a and literature findings [129, 132] a DP of 50 was chosen to represent

a PP chain. Furthermore, a similar behaviour is observed for the PET in Fig. 4.15b where a plateau in the density at about 1.25 g/cm^3 is found. However, the solubility parameter seems to drastically drop at 60 repeat units which could be in part due to the relatively coarse structure minimization employed in this study or insufficient equilibration. In general, the cause of the drop in solubility parameter with increasing chain length is not known, but it may be speculated that a more crystalline order can persist at low DP; this finite size effect will increase the cohesive energy and hence the solubility parameter. However, based on the plots in Fig. 4.15b a DP of 30 was chosen for PET which also seems reasonable given that Y. Fu et al. [74] used 20 repeat units to represent their PET chain for blend miscibility studies. It should be noted that negative deviations between simulated and experimental solubility parameter values have also been observed for simulated polymer systems using COMPASS [19, 71, 131] and other force fields [133]. Bulky side groups will restrict the rotation of the backbone C-C bonds leading to low probabilities of overcoming torsional energy barriers. Furthermore, combined with insufficient equilibration it inhibits the possibility of thoroughly exploring the potential energy surfaces. Thus, the effort of locating configurations which would enhance intermolecular interactions, and hence solubility parameters and densities, will be hampered. On the other hand, other authors report an agreement between simulated and experimental solubility parameters using the COMPASS force field, e.g. for PET and polylactic acid [74]. In this latter study the authors, however, used a more thorough equilibration protocol than employed in this work, thus supporting the above-mentioned discussion.

For the equilibration runs it is possible to choose different relaxation time values to control the strength of coupling to pressure baths. Thus, in the NPT-dynamics used to equilibrate the structures at atmospheric pressure, the influence of different relaxation time constants τ_P in Eq. (2.28) were investigated using the Berendsen barostat. This was done on both pure PP and PET. The resulting curves showing the time evolution of density and cell lengths can be found in Appendix H while solubility parameters of the resulting structures are presented in Table 4.6.

TABLE 4.6: Influence of relaxation constant τ_P (Eq. (2.28)) during NPT-dynamics on solubility parameters δ in the pure systems.

[The δs are calculated after performing t$_{\mathrm{NPT}}$ ps NPT at 1 bar and 298 K, and t$_{\mathrm{NVT}}$ ps NVT-dynamics at 298 K. Then, δ is the average of the last 50 ps of the NVT-dynamics.]

	$\tau_P = 0.1$ ps			$\tau_P = 0.05$ ps			$\tau_P = 0.025$ ps		
	t$_{\mathrm{NPT}}$ (ps)	t$_{\mathrm{NVT}}$ (ps)	$\delta \left[\left(\frac{\mathrm{J}}{\mathrm{cm}^3} \right)^{0.5} \right]$	t$_{\mathrm{NPT}}$ (ps)	t$_{\mathrm{NVT}}$ (ps)	$\delta \left[\left(\frac{\mathrm{J}}{\mathrm{cm}^3} \right)^{0.5} \right]$	t$_{\mathrm{NPT}}$ (ps)	t$_{\mathrm{NVT}}$ (ps)	$\delta \left[\left(\frac{\mathrm{J}}{\mathrm{cm}^3} \right)^{0.5} \right]$
PP[†]	200	100	13.2	150	100	13.4			
PET[‡]	400	100	19.9	400	100	20.1	400[§]	100	19.8

[†]Loading was 9 polymer chains each consisting of 50 repeat units.

[‡]Loading was 9 polymer chains each consisting of 30 repeat units.

[§]After an additional 200 ps at 2, 20 and 1 bar pressure $\delta = 20.1 \left(\mathrm{J/cm}^3 \right)^{0.5}$.

From Table 4.6 it is seen that the calculated solubility parameters are relatively insensitive to the choice of relaxation time constant. However, from the plots in Appendix H it is clear that decreasing the relaxation time allows the structure to reach an equilibrium more rapidly. This is advantageous when equilibrating structures, and hence subsequent NPT equilibration dynamics with the Berendsen barostat used $\tau_P = 0.025$ ps, except for the pure PP system where $\tau_P = 0.05$ ps was used.

After equilibrating the blend structures at 298 K and 1 bar, 100 ps NVT-dynamics

were performed, the last 50 ps of which were used for the analysis of cohesive energies (see Eq. (2.13)). The resulting FH interaction parameters as a function of PET content in the blends are presented in Fig. 4.16.
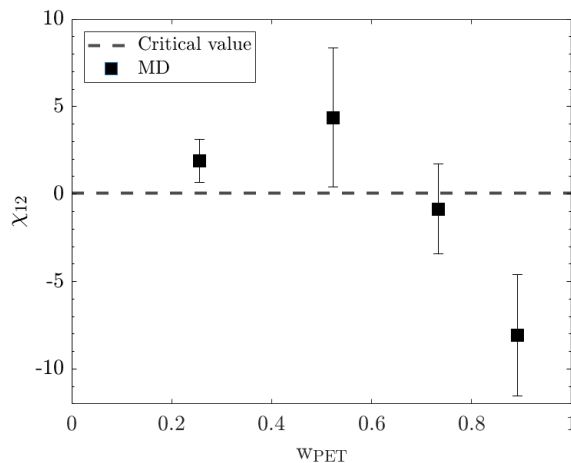
FIGURE 4.16: The Flory-Huggins interaction parameters χ_{12} between polypropylene (PP) and polyethylene terephthalate (PET) for the various PP/PET blends at 298 K. Values represented by squares are calculated from data obtained by molecular dynamics simulations (MD) together with Eq. (2.13), while the critical value ($\chi_c = 0.054$) was calculated using Eq. (2.16). Error bars represent the standard error of the mean calculated based on three different initial structures.

To the author's knowledge, no similar study has been performed on PP/PET blends. Yet, some authors report that PP and PET are immiscible at concentrations similar to those investigated by MD in this study [20]. Furthermore, it is seen that the blend becomes more immiscible with the increase in PET content from 25 to 50 wt.%. However, the PP25/PET75 blend seems to be slightly miscible, yet more initial structures are needed to reduce the standard error. Interestingly, it appears the PP10/PET90 blend becomes miscible as the predicted interaction parameter is around -8.1, well below the critical value of $\chi_c = 0.054$. MD of various blends have shown, that the interaction parameter shows a concentration dependence [18, 71], and the blend may display miscibility in narrow to relatively broad concentration ranges [29, 129]. The miscibility observed in Fig. 4.16 can be speculated to be due to dipole-dipole interactions between the ester-groups of PET which will amount to a relatively large cohesive energy and thus solubility parameter as seen in Table 4.5 when comparing PET and PP. Yet, it is not possible to directly study this dipole-dipole interaction with the COMPASS forcefield as it is included in the non-bonded interactions.

Molecular dynamics simulations were performed to estimate the glass transition temperature of the PP and PET in both the pure systems, the PP75/PET25 and PP/PP-g-PET blends. It should be noted, however, that due to the limited accessible timescales available for MD simulations, the resulting cooling rate used to locate the glass transition temperature in this study was 7.2×10^{12} K min^{-1}; this is in stark contrast to the $10 - 40$ K min^{-1} used in typical DSC scans. With structural relaxation time scales of the order $\sim 10^2$ s close to the T_g [134], a large cooling rate can be expected to displace T_g values to higher temperatures since, at the T_g, the characteristic experimental and structural relaxation times become equal [135–137]. The obtained specific volume versus temperature cooling curves for PP, PET, PP75/PET25 and PP/PP-g-PET systems are shown in Fig. 4.17.
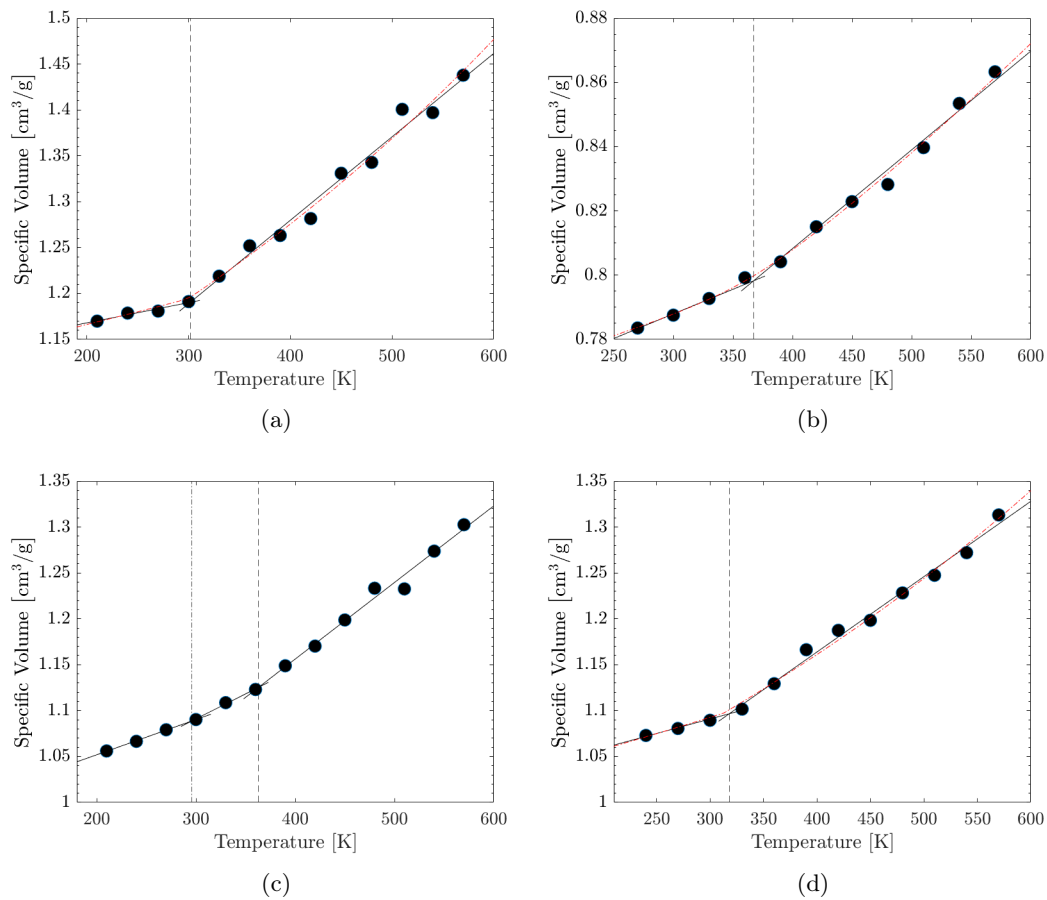
FIGURE 4.17: Specific volume calculated from last $50\,\mathrm{ps}$ of NPT-dynamics at each temperature for the pure PP (a), pure PET (b), the PP75/PET25 blend (c), and PP/PP-g-PET blend (d). The grafted content of MAH on PP in the PP/PP-g-PET blend was $5\,\mathrm{wt}\,\%$, PP content was roughly $75\,\mathrm{wt}\,\%$ in total, and the compatibilizer content was roughly 10 wt.%. The solid lines are linear fits to the data, and their intersections are marked by the dashed vertical lines. The red dotted lines are the hyperbola fits obtained with Eq. (4.5).

From Figs. 4.17a, 4.17b and 4.17d a relatively clear bend in the curves is seen and marked by the vertical dashed lines. On the other hand, the non-compatibilized blend in Fig. 4.17c appears to show two such bends; the two glass transitions are an indication of the immiscibility of this blend which is in agreement with the findings from the FH interaction parameter in Fig. 4.16.

In order to investigate more quantitatively the glass transition temperatures of the PP and PET in the systems, two methods were employed. Firstly, the glass transition temperature is located in the region where the specific volume versus temperature graph departs from a linear relationship [60]. This separates the glassy region at low temperatures from the rubbery region at high temperatures. The intersection point of the best fit lines to the linear portion of each region is then taken as the glass transition temperature [134]. However, this procedure requires the modeler to assess the range of data in both the glassy and rubbery regions to be fitted, thus making this approach relatively subjective. Hence, the second approach dispenses this issue by fitting all points in the density vs. temperature-data to a hyperbola regression model following the procedure outlined by P. N. Patrone et al. [12]. The equation for the single-branch hyperbola is

$$\rho(T) = \rho_0 - a\,(T - T_0) - b\left[\frac{1}{2}\,(T - T_0) + \sqrt{\frac{(T - T_0)^2}{4} + \exp(c)}\,\right], \qquad (4.5)$$

where $\rho(T)$ is the density at temperature T, ρ_0 and T_0 are the density and temperature at the glass transition, and a, b and c are constant parameters. In the limit $c \to -\infty$ one obtains $\rho(T) = \rho_0 - a\,(T - T_0) - b\left[\frac{1}{2}\,(T - T_0) + \frac{1}{2}\sqrt{(T - T_0)^2}\,\right]$; it is thus seen that the parameters $-a$ and $-(a+b)$ are the slopes of the low and high-temperature regimes, respectively. Since density typically decreases with temperature, a and b are positive whereas c, which smooths out the slope discontinuity at $T = T_0$, may take any value. Both approaches were applied to the data in Fig. 4.17, and the obtained T_g-values for both PP and PET are presented in Table 4.7.

TABLE 4.7: Glass transition temperatures (T_g) of the PP, PET and PP-g-PET found by molecular dynamics simulations.

System	Linear fit[†]		Hyperbola fit[‡]	
	$T_{g,PP}$	$T_{g,PET}$	$T_{g,PP}$	$T_{g,PET}$
Pure PET	-	367 K	-	360 K
Pure PP	302 K	-	300 K	-
PP75/PET25	296 K	363 K	-	-
PP/PP-g-PET	318 K		313 K	

[†]Intersection of straight lines obtained from least squares regression in the glassy and rubbery regions.
[‡]Obtained with non-linear regression using Eq. (4.5) by minimizing the squared error between (all) data and hyperbola fit $\sum_i \left[\rho_{data}(T_i) - \rho_{hyperbola}(T_i)\right]^2$.

Firstly, the T_g-values for PP and PET in the pure systems found with the two above-mentioned methods agree well. Secondly, the T_g-values for PP and PET in the non-compatibilized blend are very similar to the T_g-values in the pure systems. This quantitatively suggests the blend is immiscible as expected since the two components of the blend do not exhibit specific interactions [122, 138]. However, taking values for the T_g of PP to be 276 K [139], and that of PET as 342 K from DSC measurements at 20 K/min [140], it is seen that the MD simulations tend to overestimate the experimental value. This is in agreement with the above-mentioned and findings by Y. Wang et al. [141]; these authors found the T_g of PET by MD to be roughly 357-362 K with a heating rate of 8×10^{11} K min^{-1}. As mentioned by A. Soldera et al. [60], another reason for the discrepancies between experimental and simulated T_g's could be due to a low number of configurations used to represent the phase space (see Eq. (2.19)). Yet, P. Gestoso et al. [133] mention that satisfactory agreement between their simulated and experimentally measured T_g of poly(vinyl phenol) may be due to the simulations not accessing the same spectrum of conformational fluctuations. Nevertheless, since the results in Fig. 4.17 are based on only one initial configuration of each system, data from more initial configurations would likely improve the accuracy of the predicted T_gs. This is due to the fact that the more complicated the energy landscape, the greater the specific volume fluctuations in the curves of specific volume versus temperature. Hence, a smaller fraction of the total possible configurations are explored [12]. Also, since the glass transition is a kinetic process, the path traversed by the molecule through the energy landscape will influence the structure of the molecule and the glass transition. Furthermore, factors influencing

the simulated glass transition temperature are; firstly, the MW (and hence DP) of the chains where, according to the Flory-Fox theory of free volume, a decrease in MW will decrease the T_g due to a larger free volume [134]. For instance, M. Mohammadi et al. [142] observed, for various DPs of poly(methyl methacrylate) and at various simulated cooling rates using MD, a decrease in T_g with decreasing DP. Secondly, the initial density of the system influences the T_g since, again, a lower density will increase the free volume and hence reduce the T_g [143]. Combined, these latter two factors and the high cooling rate may be speculated to impose a compensating effect on the simulated T_g, thus making it reasonably close to the experimentally observed value [143]. However, the degree of influence the two above-mentioned factors exert on the estimated T_g-values has not been investigated in this project. Lastly, the effect of the cooling rate deserves some extra attention. Some authors have suggested the use of the Williams-Landel-Ferry (WLF) equation to relate the shift in T_g

$$\Delta T_g = \frac{-C_2 \cdot \log_{10}\left(\frac{\dot{q}_{\mathrm{exp}}}{\dot{q}_{\mathrm{sim}}}\right)}{C_1 + \log_{10}\left(\frac{\dot{q}_{\mathrm{exp}}}{\dot{q}_{\mathrm{sim}}}\right)}, \tag{4.6}$$

to the relative cooling rates $\left(\frac{\dot{q}_{\mathrm{exp}}}{\dot{q}_{\mathrm{sim}}}\right)$ between experiments and simulations, with the 'universal' parameters being $C_1 = 17.44$ and $C_2 = 51.6\,\mathrm{K}$ [144]. At not too large simulation cooling rates $\dot{q}_{\mathrm{sim}}$ it is seen from Eq. (4.6) that the T_g shifts $\frac{C_2}{C_1} \approx 3\,\mathrm{K}$ per decade change in simulation cooling rate. With this rule of thumb in mind, the previously mentioned experimental glass transition temperatures ($276\,\mathrm{K}$ for PP and $342\,\mathrm{K}$ for PET) can be estimated to shift to higher temperatures by roughly $36\,\mathrm{K}$ (assuming an order of magnitude $\dot{q}_{\mathrm{exp}} \sim 10^1$ K/s), in closer agreement with the values presented in Table 4.7.

Regarding the reactively compatibilized PP75/PET25 blend, PP/PP-g-PET, the estimated T_g which is 45-49 K lower than $\mathrm{T_{g,PET}}$ in the pure PET and (non-compatibilized) PP75/PET25 blend. The lowering of $\mathrm{T_{g,PET}}$ was observed experimentally in PP80/PET20 blends reactively compatibilized by SEBS-g-MAH [77, 112] or PP-g-MAH [116], and PP70/PET30 blends reactively compatibilized by GMA- and epoxy-functionalized copolymers [111]. This was attributed to the enhanced interactions between the two incompatible domains. However, in this MD study the results may be interpreted in terms of an increased free volume due to the bulky MAH-sidegroup on the PP-g-PET copolymer. Even though the fractional free volume was not computed, the necessary information can be inferred from the molar volume-plot in Fig. 4.18.
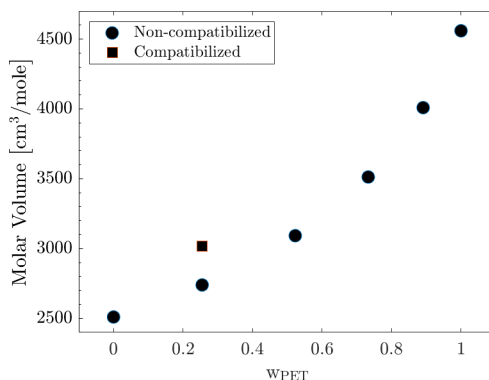
FIGURE 4.18: Average molar volumes from three different initial structures of the various blends and pure systems investigated in this study at 298 K and 1 bar. Here, 'compatibilized' refers to the PP/PP-g-PET blend. Molar volume was calculated as an average from the last 50 ps of the NPT-dynamics for three different initial structures, except the PP/PP-g-PET which was based on one initial structure.

Apart from the non-ideal behaviour of molar volume with PET content, it is seen how the molar volume of the PP75/PET25 blend increases significantly when compatibilizing the blend. The increase is attributed to the bulky MAH-sidegroup since the remainder of the blend components remain unchanged (i.e. DP, number of molecules etc.). This will accordingly endow the PET with a greater mobility and hence lower T_g. However, the influence of combining two different materials on the physical properties of the resulting material must also be taken into account. This was for instance discussed in the previous section regarding the compatibilization of rPPC/PET blends. Furthermore, it must be noted that from Fig. 4.17d only one T_g-value is discernible namely that of the PP-g-PET copolymer. Thus, from the obtained data it was not possible to locate the T_g of PP in the compatibilized blend.

The radial distribution function (RDF) g(r) presented in Eq. (2.30) can be separated into two components; an intramolecular RDF containing information about the conformation, and an intermolecular RDF related to the molecular arrangement in the bulk structure [133]. The intermolecular g(r) has been used to assess the miscibility in polymer blends [15, 74, 129]; when g(r) values of certain atom pairs residing in distinct components are greater than g(r) values found for atom pairs of similar components, P. Gestoso et al. [145] mention the blend shows a tendency towards miscibility. On the other hand, a lower g(r) for atom pairs of distinct components indicates immiscibility. Thus, the remainder of this section will focus on the computed intermolecular RDFs for carbon-carbon pairs $\left(g_{c-c}^{inter}(r)\right)$ in the pure components and non-compatibilized blends. The intermolecular RDFs were calculated using the last 50 ps trajectories of the NVT-production runs for three different initial structures, and they are presented in Fig. 4.19.
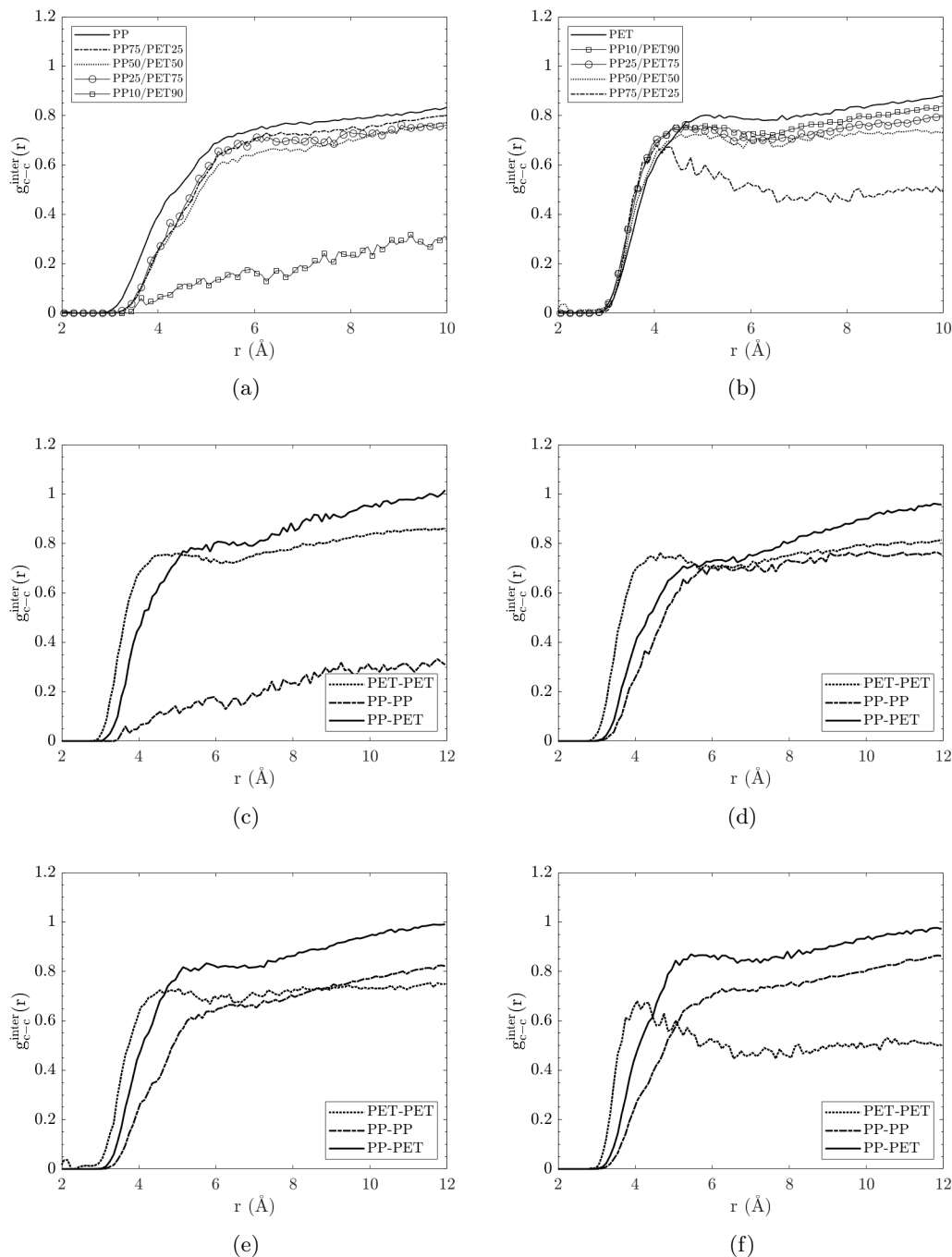
FIGURE 4.19: Radial distribution functions $g_{c-c}^{inter}(r)$ of the intermolecular carbon-carbon pairs in similar (PP-PP and PET-PET) and dissimilar (PP-PET) sets of the PP in the pure and blended systems (a), PET in the pure and blended systems (b), PP10/PET90 (c), PP25/PET75 (d), PP50/PET50 (e), and PP75/PET25 (f). The $g_{c-c}^{inter}(r)$ are the averages of three different initial structures.

No distinct peaks appear in the RDF for carbon-carbon pairs in the pure PP or between PP chains in the blends in Fig. 4.19a. This implies the absence of a crystalline-like order [133]. For the PP75/PET25 blend in Fig. 4.19b, however, a peak is present at roughly 4 Å. Y. Fu et al. [74] similarly found a peak at roughly 4 Å in the $g_{c-c}^{inter}(r)$ of PET-PET chains, and G. W. Longman et al. [146] suggested this peak, in their case derived from the RDF of x-ray diffraction data from PET samples, is

related to nearest neighbour intermolecular ordering. Otherwise, at larger distances the $g_{c-c}^{inter}(r)$ generally decreases as both PP and PET contents decrease in Figs. 4.19a and 4.19b, respectively. This implies, that carbon pairs of similar chains are less likely found near each other as their concentration decreases, in agreement with data reported in the literature from MD simulations on PP/polyamide-11 and poly(ethylene oxide)/poly(vinyl chloride) blends [15, 129].

The general trend of $g_{c-c}^{inter}(r)$ in Figs. 4.19c to 4.19f is that PET-PET interactions appear to dominate at shorter distances up to $r < 4-6$ Å since it is larger than the other RDFs at these distances. Hereafter, carbon-carbon pairs of dissimilar chains (PP-PET) appear more prevalent. However, having the above-mentioned criterion for miscibility in mind, then from the computed χ_{12}-values in Fig. 4.16 it would be expected at least for the PP10/PET90 blend that the $g_{c-c}^{inter}(r)$ for PP-PET would be larger than that of PET-PET at relatively short distances as well. Yet, the dominating $g_{c-c}^{inter}(r)$ for PET-PET at shorter distances suggest that PET-PET interactions are relatively strong and thus lead to the large cohesive energy of the blends and hence negative χ_{12}-values; these interaction could e.g. be dipole-dipole interactions between ester groups as previously mentioned, since they are relatively short-ranged.

The effect of reactive compatibilization in the PP75/PET25 blend was also studied by means of RDFs. Figure 4.19f is reproduced in Fig. 4.20 along with the $g_{c-c}^{inter}(r)$ for the PP/PP-g-PET blend.
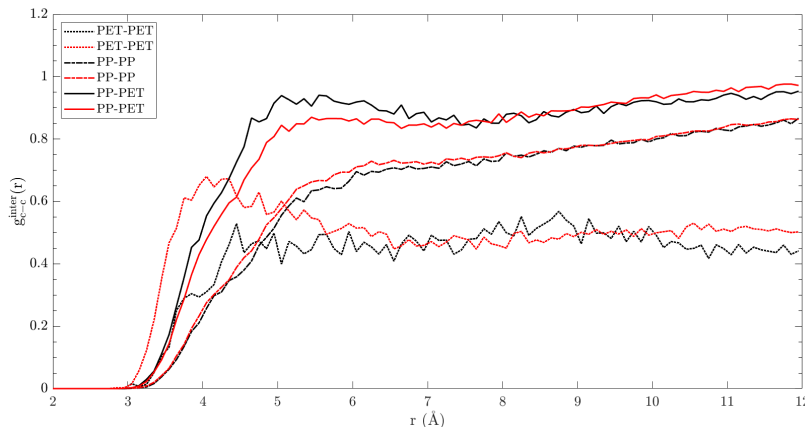
FIGURE 4.20: Radial distribution functions $g_{c-c}^{inter}(r)$ of the intermolecular carbon-carbon pairs of similar (PP-PP and PET-PET) and dissimilar (PP-PET) sets in the PP75/PET25 (red) and PP/PP-g-PET (black) blends.

It can be noticed how the $g_{c-c}^{inter}(r)$ of PET-PET is significantly lower in the compatibilized blend while simultaneously being similar to, or lower, than the $g_{c-c}^{inter}(r)$ for PP-PET. This suggests a diminished tendency to form PET-PET contacts in the compatibilized blend. It can be speculated to be partly due to the increased MW of the copolymer relative to isolated PP and PET which decreases the mobility [147], thus impeding the ordering of PET units. On the other hand, a slight increase in the tendency to find carbon-carbon pairs between PP and PET appears in the PP/PP-g-PET blend relative to PP75/PET25. Moreover, at larger separations of roughly $r > 7$ Å the $g_{c-c}^{inter}(r)$ for PP-PET in both blends are comparable and approach a value of one. These observations are to some extent expected since a copolymer between PP and PET is formed in the PP/PP-g-PET blend, yet at larger separations the presence of the copolymer should not influence the location of the free PP chains.

Chapter 5

Conclusion

Morphological and rheological studies were performed on immiscible blends of polypropylene (PP) and poly(ethylene terephthalate glycol) (PETG) in order to evaluate the effect of various processing temperatures during extrusion compounding on the blend miscibility. Polarized light optical microscopy (PLOM) images of the surface of extruded pellets revealed a larger density, size and polydispersity of dispersed phase droplets with increasing dispersed phase content.

Furthermore, the rheological Palierne model for immiscible viscoelastic blend components was applied in the analysis of dispersed phase droplet size during oscillatory shear at the processing temperatures. The model fit the data with moderate success, and the predicted droplet sizes were compared to those obtained from melt morphology analysis at the processing temperatures measured under static conditions. It was found that the Palierne model greatly overestimated dispersed phase particle dimensions. However, both microscopy and rheology analysis revealed a tendency of larger dispersed phase droplets with increased dispersed phase content and processing temperature, suggesting increased immiscibility. Furthermore, the melt morphology analysis revealed a coarsening of the dispersed phase droplets as would be expected from Ostwald ripening.

Blends of PP and high-density polyethylene (HDPE) (rPPC) and poly(ethylene terephthalate) (PET) and 6 wt % Acti-Tech 09MA13 (AT) compatibilizer, denoted rPPC/PET, were mixed with various amounts of addition AT compatibilizer to study the influence of AT content on the blend properties. Larger amounts of additional AT were found to improve the dispersion.

Fourier-transform infrared spectroscopy revealed the maleic anhydride (MAH) functionalized AT reacted with PET to form PET-g-AT copolymers. The formation of PET-g-AT impeded the crystallization, and hence lowered the degree of crystallinity, of PET due to reduced mobility.

Furthermore, dynamic mechanical analysis (DMA) revealed a notable decrease in the glass transition temperature (T_g) of PP with additional AT content. This was speculated to be due partly to an increased free volume, caused by the addition of AT with relatively bulky MAH grafted sidegroups, and the affinity between AT and rPPC resulting in a combination between the mechanical properties of AT and rPPC. On the other hand, DMA revealed only a slight decrease of the (T_g) of PET which could be speculated to be due to the formation of PET-g-AT copolymer with properties again in between PET and AT.

Mechanical properties from tensile and impact tests revealed an improved ductility and impact strength with additional compatibilizer, suggesting an improved interfacial adhesion and stress transfer between the phases in the blend. However, due to large standard deviations the increase in impact strength when adding 6 wt % compared

to 4 wt % AT to the rPPC/PET blend was minimal. Lastly, rheological analysis at the processing temperature clearly revealed an increased elasticity with additional AT content due to improved interfacial adhesion due to the formation of PET-g-AT.

Molecular dynamics simulations (MD) were performed on various blends of PP and PET to study their miscibility using various methods. Preliminary investigations set out to determine the minimum representative dimensions of PP and PET for further studies, and a degree of polymerization (DP) of $DP = 50$ and $DP = 30$ for PP and PET was chosen, respectively. Simulated solubility parameters (δ) and densities (ρ) were underestimated relative to experimentally observed values, which was at least partly attributed to insufficient or coarse equilibration.

Three different initial structures of the investigated blends and pure systems were then equilibrated and analyzed for cohesive energies from which the Flory-Huggins (FH) interaction parameter could be extracted. The PP75/PET25 and PP50/PET50 blends were found to be immiscible, the standard error of the PP25/PET75 blend was on both sides of the critical FH interaction parameter, but the PP10/PET90 blend appeared miscible. The latter finding was speculated to be due to relatively strong dipole-dipole interactions between PET chains which favor PET-PET interactions, not specific interactions between PP and PET.

Furthermore, the glass transition temperatures in the pure systems and PP75/PET25 non-compatibilized and compatibilized (denoted PP/PP-g-PET) blends were investigated by dilatometry where a kink in the specific volume vs. temperature-curve signifies the glass transition. Linear extrapolation and hyperbolic regression analysis yielded comparable values of T_g; 360 K-367 K for PET, 296 K-302 K for PP, and 313 K-318 K for the PP-g-PET copolymer. The simulations overestimate the T_gs for PP and PET by up to 9 and 7 % compared to experimental values, respectively. This is consistent with the orders of magnitude larger cooling rate in MD compared to experiments. Furthermore, T_gs for PP and PET in pure systems and the PP75/PET25 blend are similar, substantiating the immiscibility of this blend observed from the thermodynamic analysis. However, the T_g observed in the PP/PP-g-PET blend is between that of PP and PET as expected for a copolymer. Furthermore, an increased free volume might also have contributed to the lowering of the T_g relative to that of PET.

Lastly, intermolecular radial distribution functions (RDFs) between carbon-carbon pairs in similar and dissimilar (PP and PET chains) sets were investigated. Generally, a tendency for ordering of PET at short distances was observed in all non-compatibilized blends which could be driven by the above-speculated tendency to form dipole-dipole interactions between ester-groups. However, in the PP/PP-g-PET blend this ordering was absent and instead carbon-carbon pairs of dissimilar sets were more likely to be found near one another. This was likely due to the presence of the copolymer whereby PP and PET are connected by the maleic anhydride acting as a linkage.

Bibliography

[1] J. Parameswaranpillai, S. Thomas, and Y. Grohens, "Polymer Blends: State of the Art, New Challenges, and Opportunities", in *Characterization of Polymer Blends: Miscibility, Morphology and Interfaces*, edited by S. Thomas, Y. Grohens, and P. Jyotishkumar (John Wiley and Sons, 2015) Chap. 1, pp. 1–5.

[2] L. A. Utracki and Z. H. Shi, "Development of polymer blend morphology during compounding in a twin-screw extruder. Part I: Droplet dispersion and coalescence - A review", Polym. Eng. Sci. **32**, 1824–1833 (1992).

[3] T. Ougizawa, S. A. Madbouly, and T. Inoue, "Shear flow effect on phase behaviour and morphology in polymer blends", Macromol. Symp. **149**, 69–74 (2000).

[4] J.-B. An, T. Suzuki, T. Ougizawa, T. Inoue, K. Mitamura, and K. Kawanishi, "Studies on miscibility and phase-separated morphology of nylon 4,6/poly(phenylene sulfide) blend under shear flow", J. Macromol. Sci. **41**, 407–418 (2002).

[5] J. K. Lee and C. D. Han, "Evolution of polymer blend morphology during compounding in an internal mixer", Polymer **40**, 6277–6296 (1999).

[6] B. D. Favis and D. Therrien, "Factors influencing structure formation and phase size in an immiscible polymer blend of polycarbonate and polypropylene prepared by twin-screw extrusion", Polymer **32**, 1474–1481 (1991).

[7] K. Friedrich, M. Evstatiev, S. Fakirov, O. Evstatiev, M. Ishii, and M. Harrass, "Microfibrillar reinforced composites from PET/PP blends: processing, morphology and mechanical properties", Compos. Sci. Technol. **65**, 107–116 (2005).

[8] C. C. Chen and J. L. White, "Compatibilizing agents in polymer blends: Interfacial tension, phase morphology, and mechanical properties", Polym. Eng. Sci. **33**, 923–930 (1993).

[9] J. Maris, S. Bourdon, J.-M. Brossard, L. Cauret, L. Fontaine, and V. Montembault, "Mechanical recycling: Compatibilization of mixed thermoplastic wastes", Polym. Degrad. Stabil. **147**, 245–266 (2018).

[10] E. P. A. van Bruggen, R. P. Koster, S. J. Picken, and K. Ragaert, "Influence of processing parameters and composition on the effective compatibilization of polypropylene-poly(ethylene terephthalate) blends", Intern. Polymer Processing XXXI **2**, 179–187 (2016).

[11] S. A. Hollingsworth and R. O. Dror, "Molecular dynamics simulation for all", Neuron **99**, 1129–1143 (2018).

[12] P. N. Patrone, A. Dienstfrey, A. R. Browning, S. Tucker, and S. Christensen, "Uncertainty quantification in molecular dynamics studies of the glass transition temperature", Polymer **87**, 246–259 (2016).

[13]T. E. Gartner, III and A. Jayaraman, "Modeling and simulations of polymers: a roadmap", Macromolecules **52**, 755–786 (2019).

[14]E. Meaurio, N. Hernandez-Montero, E. Zuza, and J.-R. Sarasua, "Miscible blends based on biodegradeable polymers", in *Characterization of Polymer Blends: Miscibility, Morphology and Interfaces*, edited by S. Thomas, Y. Grohens, and P. Jyotishkumar (John Wiley and Sons, 2015) Chap. 2, pp. 7–92.

[15]Z. Luo and J. Jiang, "Molecular dynamics and dissipative particle dynamics simulations for the miscibility of poly(ethylene oxide)/poly(vinyl chloride) blends", Polymer **51**, 291–299 (2010).

[16]E. Braun, J. Gilmer, H. B. Mayes, D. L. Mobley, J. I. Monroe, S. Prasad, and D. M. Zuckerman, "Best practices for foundations in molecular simulations", Living J. Comp. Mol. Sci. **1**, 5957 (2019).

[17]A. Gooneie, S. Schuschnigg, and C. Holzer, "A review of multiscale computational methods in polymeric materials", Polymers **9**, 16 (2017).

[18]S. S. Jawalkar and T. M. Aminabhavi, "Molecular modeling simulations and thermodynamic approaches to investigate compatibility/incompatibility of poly(L-lactide) and poly/vinyl alcohol) blends", Polymer **47**, 8061–8071 (2006).

[19]I. M. de Arenaza, E. Meaurio, B. Coto, and J.-R. Sarasua, "Molecular dynamics modelling for the analysis and prediction of miscibility in polylactide/polyvinylphenol blends", Polymer **51**, 4431–4438 (2010).

[20]K. H. Yoon, H. W. Lee, and O. O. Park, "Properties of poly(ethylene terephthalate) and maleic anhydride-grafted polypropylene blends by reactive processing", J. Appl. Polym. Sci. **70**, 389–395 (1998).

[21]C. P. Papadopoulou and N. K. Kalfoglou, "Comparison of compatibilizer effectiveness for PET/PP blends: their mechanical, thermal and morphology characterization", Polymer **41**, 2543–2555 (2000).

[22]L. M. Robeson, *Polymer blends: a comprehensive review*, 1st ed. (Carl Hanser Verlag, Munich, 2007) Chap. 2, pp. 11–19.

[23]Z. Stary, "Thermodynamics and morphology and compatibilization of polymer blends", in *Characterization of Polymer Blends: Miscibility, Morphology and Interfaces*, edited by S. Thomas, Y. Grohens, and P. Jyotishkumar (John Wiley and Sons, 2015) Chap. 3, pp. 93–111.

[24]J. S. Higgins, J. E. G. Lipson, and R. P. White, "A simple approach to polymer mixture miscibility", Phil. Trans. R. Soc. A **368**, 1009–1025 (2010).

[25]P. J. Flory, "Thermodynamics of high polymer systems", J. Chem. Phys. **10**, 51–61 (1942).

[26]M. L. Huggins, "Thermodynamic properties of solutions of long-chain compounds", Ann. NY Acad. Sci. **43**, 1–32 (1942).

[27]C. M. Hansen, *Hansen Solubility Parameters: A User's Handbook*, 2nd ed. (CRC Press, 2007) Chap. 5, pp. 107–109.

[28]J. M. Hughes, D. Aherne, and J. N. Coleman, "Generalizing solubility parameter theory to apply to one- and two-dimensional solutes and to incorporate dipolar interactions", J. Appl. Polym. Sci. **127**, 4483–4491 (2013).

[29] S. S. Jawalkar, S. G. Adoor, M. Sairam, M. N. Nadagouda, and T. M. Aminabhavi, "Molecular modeling on the binary blend compatibility of poly(vinyl alcohol) and poly(methyl methacrylate): an atomistic simulation and thermodynamic approach", J. Phys. Chem. B **109**, 15611–15620 (2005).

[30] Y. C. Bae, J. J. Shim, D. S. Soane, and J. M. Prausnitz, "Representation of vapor-liquid and liquid-liquid equilibria for binary systems containing polymers: Applicability of an extended Flory-Huggins equation", J. Appl. Polym. Sci. **47**, 1193–1206 (1993).

[31] A. Eliassi, H. Modarress, and G. A. Mansoori, "Measurement of activity of water in aqueous Poly(ethylene glycol) solutions (effect of excess volume on the Flory-Huggins χ-parameter)", J. Chem. Eng. Data **44**, 52–55 (1999).

[32] M. T. Zafarani-Moattar and N. Tohidifar, "Vapor-liquid equilibria, density, and speed of sound for the system poly(ethylene glycol) 400 + methanol at different temperatures", J. Chem. Eng. Data **51**, 1769–1774 (2006).

[33] N. Schuld and B. A. Wolf, "Solvent quality as reflected in concentration- and temperature-dependent Flory-Huggins interaction parameters", J. Polym. Sci. B Polym. Phys. **39**, 651–662 (2001).

[34] M. Tambasco, J. E. G. Lipson, and J. S. Higgins, "Blend miscibility and the Flory-Huggins interaction parameter: a critical examination", Macromolecules **39**, 4860–4868 (2006).

[35] L. A. Utracki, "Compatibilization of polymer blends", Can. J. Chem. Eng. **80**, 1008–1016 (2002).

[36] E. Van Hemelrijck, P. Van Puyvelde, S. Velankar, C. W. Macosko, and P. Moldenaers, "Interfacial elasticity and coalescence suppression in compatibilized polymer blends", J. Rheol. **48**, 143–158 (2004).

[37] U. Sundararaj and C. W. Macosko, "Drop breakup and coalescence in polymer blends: the effects of concentration and compatibilization", Macromolecules **28**, 2647–2657 (1995).

[38] P. Van Puyvelde, S. Velankar, J. Mewis, and P. Moldenaers, "Effect of Marangoni stresses on the deformation and coalescence in compatibilized immiscible polymer blends", Polym. Eng. Sci. **42**, 1956 (2002).

[39] P. Van Puyvelde, S. Velankar, and P. Moldenaers, "Rheology and morphology of compatibilized polymer blends", Curr. Opin. Colloid Interface Sci. **6**, 457–463 (2001).

[40] C. Harrats, R. Fayt, and R. Jérôme, "Effect of block copolymers of various molecular architecture on the phase morphology and tensile properties of LDPE rich (LDPE/PS) blends", Polymer **43**, 863–873 (2002).

[41] Y. Lyatskaya, D. Gersappe, N. A. Gross, and A. C. Balazs, "Designing compatibilizers to reduce interfacial tension in polymer blends", J. Phys. Chem. **100**, 1449–1458 (1996).

[42] F. Berzin, J.-J. Flat, and B. Vergnes, "Grafting of maleic anhydride on polypropylene by reactive extrusion: effect of maleic anhydride and peroxide concentrations on reaction yield and products characteristics", J. Polym. Eng. **33**, 673–682 (2013).

[43]S. H. P. Bettini and J. A. M. Agnelli, "Evaluation of methods used for analysing maleic anhydride grafted onto polypropylene by reactive processing", Polym. Test. **19**, 3–15 (2000).

[44]M. Akbari, A. Zadhoush, and M. Haghighat, "PP/PET blending by using PP-g-MA synthesized by solid phase", J. Appl. Polym. Sci. **104**, 3986–3993 (2007).

[45]M. Pracella and D. Chionna, "Reactive compatibilization of blends of PET and PP modified by GMA grafting", Macromol. Symp. **198**, 161–171 (2003).

[46]M. F. Champagne, M. A. Huneault, C. Roux, and W. Peyrel, "Reactive compatibilization of polypropylene/polyethylene terephthalate blends", Polym. Eng. Sci. **39**, 976–989 (1999).

[47]J. M. Haile, *Molecular dynamics simulation*, 1st ed. (John Wiley and Sons, 1997) Chap. 2 and 3, pp. 11–67.

[48]J. P. Dahl, *Introduction to the quantum world of atoms and molecules*, 1st ed. (World Scientific Publishing Co. Pte. Ltd., 2001) Chap. 13, pp. 289–293.

[49]X. P. Resina, "Study of the reaction mechanism in Mandelate Racemase enzyme: reaction path and dynamical sampling approaches", PhD thesis (Universitat Autonoma de Barcelona, 2004).

[50]J. R. Maple, U. Dinur, and A. T. Hagler, "Derivation of force fields for molecular mechanics and dynamics from ab-initio energy surfaces", Proc. Natl. Acad. Sci. **85**, 5350–5354 (1988).

[51]S. A. Adcock and J. A. McCammon, "Molecular dynamics: survey of methods for simulating the activity of proteins", Chem. Rev. **106**, 1589–1615 (2006).

[52]M. A. González, "Force fields and molecular dynamics simulations", Collection SFN **12**, 169–200 (2011).

[53]S. L. Mayo, B. D. Olafson, and W. A. Goodard III, "Dreiding: a generic force field for molecular simulations", J. Phys. Chem. **94**, 8897–8909 (1990).

[54]A. K. Rappé, C. J. Casewit, K. S. Colwell, W. A. Goodard III, and W. M. Skiff, "UFF, a full periodic table force field for molecular mechanics and molecular dynamics simulations", J. Am. Chem. Soc. **114**, 10024–10035 (1992).

[55]A. D. MacKerrel Jr., D. Bashford, M. Bellott, R. L. Dunbrack, J. D. Evanseck, M. J. Field, S. Fischer, J. Gao, H. Guo, S. Ha, D. Joseph-MacCarthy, L. Kuchnir, K. Kuczera, F. T. K. Lau, C. Mattos, S. Michnick, T. Ngo, D. T. Nguyen, B. Prodhom, W. E. Reiher III, B. Roux, M. Schlenkrich, J. C. Smith, R. Stote, R. Straub, M. Watanabe, J. Wiórkiewicz-Kuczera, D. Jin, and M. Karplus, "All-atom empirical potential for molecular modelling and dynamics studies of proteins", J. Phys. Chem. B **102**, 3586–3616 (1998).

[56]H. Sun, "COMPASS: an ab-initio force-field optimized for condensed-phase applications - overview with details on alkane and benzene compounds", J. Phys. Chem. B **102**, 7338–7364 (1998).

[57]B. A. Wells and A. L. Chaffee, "Ewald summation for molecular simulations", J. Chem. Theory. Comput. **11**, 3684–3695 (2015).

[58]C. Sagui and T. A. Darden, "Molecular dynamics simulations of biomolecules: long-range electrostatic effects", Annu. Rev. Biophys. Biomol. Struct. **28**, 155 (1999).

[59] P. H. Hunenberger, "Thermostat algorithms for molecular dynamics simulations", Adv. Polym. Sci. **173**, 105–149 (2005).

[60] A. Soldera and N. Metatla, "Glass transition of polymers: Atomistic simulation versus experiments", Phys. Rev. E **74**, 061803 (2006).

[61] G. Bussi, D. Donadio, and M. Parrinello, "Canonical sampling through velocity rescaling", J. Chem. Phys. **126**, 014101 (2007).

[62] H. C. Andersen, "Molecular dynamics simulations at constant pressure and/or temperature", J. Chem. Phys. **72**, 2384 (1980).

[63] E. A. Koopman and C. P. Lowe, "Advantages of a Lowe-Andersen thermostat in molecular dynamics simulations", J. Chem. Phys. **124**, 204103 (2006).

[64] H. J. C. Berendsen, J. P. M. Postma, W. F. van Gunsteren, A. DiNola, and J. R. Haak, "Molecular dynamics with coupling to an external bath", J. Chem. Phys. **81**, 3684 (1984).

[65] S. Nosé, "A molecular dynamics method for simulations in the canonical ensemble", Molecular Physics **100**, 191–198 (2002).

[66] W. G. Hoover, "Canonical dynamics: equilibrium phase-space distributions", Phys. Rev. A **31**, 1695–1697 (1985).

[67] A. Seeger, D. Freitag, F. Freidel, and G. Luft, "Melting point of polymers under high pressure Part I: Influence of the polymer properties", Thermochim. Acta **424**, 175–181 (2004).

[68] S. M. J. Rogge, L. Vanduyfhuys, A. Ghysels, M. Waroquier, T. Verstraelen, G. Maurin, and V. V. Speybroeck, "A comparison of barostats for the mechanical characterization of metal-organic frameworks", J. Chem. Theory. Comput. **11**, 5583–5597 (2015).

[69] B. G. Levine, J. E. Stone, and A. Kohlmeyer, "Fast analysis of molecular dynamics trajectories with graphics processing units - radial distribution function histogramming", J. Comput. Phys. **230**, 3556–3569 (2011).

[70] A. D. Drozdov, J. deC. Christiansen, R. Klitkou, and C. G. Potarniche, "Viscoelasticity and viscoplasticity of polypropylene/polyethylene blends", Int. J. Solids Struct. **47**, 2498–2507 (2010).

[71] D. Mu, X.-R. Huang, Z.-Y. Lu, and C.-C. Sun, "Computer simulation study on the compatibility of poly(ethylene oxide)/poly(methyl methacrylate) blends", Chem. Phys. **348**, 122–129 (2008).

[72] *Maleic anhydride*, https://pubchem.ncbi.nlm.nih.gov/compound/Maleic-anhydride, Accessed: 30/05-2021.

[73] I. M. Inuwa, N. C. A. Razak, R. Arjmandi, and A. Hassan, "Effects of halloysite nanotubes on the mechanical, thermal, and flammability properties of PP-g-MAH compatibilized polyethylene terephthalate/polypropylene nanocomposites", Polym. Compos. **39**, 1–11 (2017).

[74] Y. Fu, L. Liao, L. Yang, Y. Lan, L. Mei, Y. Liu, and S. Hu, "Molecular dynamics and dissipative particle dynamics simulations for prediction of miscibility in polyethylene terephthalate/polylactide blends", Molecular Simulation **39**, 415–422 (2013).

[75]R. Klitkou, E. A. Jensen, and J. de C. Christiansen, "Effect of multiple extrusions on the impact properties of polypropylene/clay nanocomposites", J. Appl. Polym. Sci. **126**, 620–630 (2012).

[76]M. Kattan, E. Dargent, J. Ledru, and J. Grenet, "Strain-induced crystallization in uniaxially drawn PETG plates", J. Appl. Polym. Sci. **81**, 3405–3412 (2001).

[77]M. Heino, J. Kirjava, P. Hietaoja, and J. Seppälä, "Compatibilization of polyethylene terephthalate/polypropylene blends with styrene-ethylene/butylene-styrene (SEBS) block copolymers", J. Appl. Polym. Sci **65**, 241–249 (1997).

[78]B. D. Favis and J. P. Chalifoux, "Influence of composition on the morphology of polypropylene/polycarbonate blends", Polymer **29**, 1761–1767 (1988).

[79]K. B. Migler, E. K. Hobbie, and F. Qiao, "*In-line* study of droplet deformation in polymer blends in channel flow", Polym. Eng. Sci. **39**, 2282–2291 (1999).

[80]J.-C. Lepers, B. D. Favis, and C. Lacroix, "The influence of partial emulsification on coalescence suppression and interfacial tension reduction in PP/PET blends", J. Polym. Sci. B Polym. Phys. **37**, 939–951 (1999).

[81]W.-R. Jiang, R.-Y. Bao, W. Yang, Z.-Y. Liu, B.-H. Xie, and M.-B. Yang, "Morphology, interfacial and mechanical properties of polylactide/poly(ethylene terephthalate glycol) blends compatibilized by polylactide-g-maleic anhydride", Mater. Des. **59**, 524–531 (2014).

[82]F. Walha, K. Lamnawar, A. Maazouz, and M. Jaziri, "Rheological, morphological and mechanical studies of sustainably sourced polymer blends based on poly(lactic acid) and polyamide 11", Polymers **8**, 61 (2016).

[83]I. Vinckier and H. M. Laun, "Manifestation of phase separation processes in oscillatory shear: droplet-matrix systems versus co-continuous morphologies", Rheol. Acta **38**, 274–286 (1999).

[84]R. Li, W. Yu, and C. Zhou, "Rheological characterization of droplet-matrix versus co-continuous morphology", J. Macromol. Sci. Part B **45**, 889–898 (2006).

[85]F. Ardakani, Y. Jahani, and J. Morshedian, "Dynamic viscoelastic behaviour of polypropylene/polybutene-1 blends and its correlation with morphology", J. Appl. Polym. Sci. **125**, 640–648 (2012).

[86]R. T. Tol, G. Groeninckx, I. Vinckier, P. Moldenaers, and J. Mewis, "Phase morphology and stability of co-continuous (PPE/PS)/PA6 and PS/PA6 blends: effect of rheology and reactive compatibilization", Polymer **45**, 2587–2601 (2004).

[87]S. Steinmann, W. Gronski, and C. Friedrich, "Quantitative rheological evaluation of phase inversion in two-phase polymer blends with cocontinuous morphology", Rheol. Acta **41**, 77–86 (2002).

[88]Y. Lv, Y. Huang, M. Kong, H. Zhu, Q. Yang, and G. Li, "Stress relaxation behaviour of co-continuous PS/PMMA blends after step shear strain", Rheol. Acta **52**, 355–367 (2013).

[89]X. Zhang, B. Li, K. Wang, Q. Zhang, and Q. Fu, "The effect of interfacial adhesion on the impact strength of immiscible PP/PETG blends compatibilized with triblock copolymers", Polymer **50**, 4737–4744 (2009).

[90] D. Graebling, R. Muller, and J. F. Palierne, "Linear viscoelastic behaviour of some incompatible polymer blends in the melt. Interpretation of data with a model of emulsion of viscoelastic liquids", Macromolecules **26**, 320–329 (1993).

[91] S. H. Anastasiadis, I. Gancarz, and J. T. Koberstein, "Interfacial tension of immiscible polymer blends: temperature and molecular weight dependence", Macromolecules **21**, 2980–2987 (1988).

[92] C. J. Carriere, G. Biresaw, and R. L. Sammler, "Temperature dependence of the interfacial tension of PS/PMMA, PS/PE, and PMMA/PE blends", Rheol. Acta **39**, 476–482 (2000).

[93] S. Tyagi, A. K. Ghosh, P. Montanari, G. W. M. Peters, and H. E. H. Meijer, "Linear viscoelastic and transient behavior of polypropylene and ethylene vinyl acetate blends: an evaluation of the linear Palierne and a nonlinear viscoelastic model for dispersive mixtures", Polym. Eng. Sci. **42**, 2107–2119 (2002).

[94] S. V. Canevarolo, "Chain scission distribution function for polypropylene degradation during multiple extrusions", Polym. Degrad. Stabil. **709**, 71–76 (2000).

[95] B. D. Favis, "The effect of processing parameters on the morphology of an immiscible binary blend", J. Appl. Polym. Sci. **39**, 285–300 (1990).

[96] F. P. La Mantia, M. Morreale, L. Botta, M. C. Mistretta, M. Ceraulo, and R. Scaffaro, "Degradation of polymer blends: A brief review", Polym. Degrad. Stabil. **145**, 79–92 (2017).

[97] C. Lacroix, M. Bousmina, P. J. Carreau, B. D. Favis, and A. Michel, "Properties of PETG/EVA blends: 1. Viscoelastic, morphological and interfacial properties", Polymer **37**, 2939–2947 (1996).

[98] A. Argoud, L. Trouillet-Fonti, S. Ceccia, and P. Sotta, "Morphologies in polyamide 6/high density polyethylene blends with high amounts of reactive compatibilizer", Eur. Polym. J. **50**, 177–189 (2014).

[99] L. Li, L. Chen, P. Bruin, and M. A. Winnik, "Morphology evolution and location of ethylene-propylene copolymer in annealed polyethylene/polypropylene blends", J. Polym. Sci. B Polym. Phys. **35**, 979–991 (1997).

[100] G. Zhang, J. Zhang, X. Zhou, and D. Shen, "Miscibility and phase structure of binary blends of polylactide and poly(vinylpyrrolidone)", J. Appl. Polym. Sci. **88**, 973–979 (2003).

[101] J.-M. Huang, H.-J. Cheng, J.-S. Wu, and F.-C. Chang, "Blends of poly(propylene) and polyacetal compatibilized by ethylene vinyl alcohol copolymers", J. Appl. Polym. Sci. **89**, 1471–1477 (2003).

[102] B. A. Calderon and M. J. Sobkowicz, "Evidence of compatibility and thermal stability improvement of poly(propylene carbonate) and polyoxymethylene blends", J. Appl. Polym. Sci. **135**, 45823 (2017).

[103] M. Sclavons, P. Franquinet, V. Carlier, G. Verfaillie, I. Fallais, R. Legras, M. Laurent, and F. C. Thyrion, "Quantification of the maleic anhydride grafted onto polypropylene by chemical and viscometric titrations, and FTIR spectroscopy", Polymer **41**, 1989–1999 (2000).

[104] F. P. La Mantia, M. Ceraulo, G. Giacchi, M. C. Mistretta, and L. Botta, "Effect of a compatibilizer on the morphology and properties of polypropylene/polyethylentherephthalate spun fibers", Polymers **9**, 47 (2017).

[105] Y. Tao and K. Mai, "Non-isothermal crystallization and melting behaviour of compatibilized polypropylene/recycled poly(ethylene terephthalate) blends", Eur. Polym. J. **43**, 3538–3549 (2007).

[106] P. J. Larkin, *Infrared and Raman spectroscopy: principles and spectral interpretation*, 2nd ed. (Elsevier, 2018) Chap. 8, p. 205.

[107] N. Billon, V. Henaff, E. Pelous, and J. M. Haudin, "Transcrystallinity effects in high-density polyethylene. I. Experimental observations in differential scanning calorimetry analysis", J. Appl. Polym. Sci. **86**, 725–733 (2002).

[108] H. P. Blom, J. W. Teh, T. Bremner, and A. Rudin, "Isothermal and non-isothermal crystallization of PP: effect of annealing and of the addition of HDPE", Polymer **39**, 4011–4022 (1998).

[109] C. Aumnate, N. Rudolph, and M. Sarmadi, "Recycling of polypropylene/polyethylene blends: effect of chain structure on the crystallization behaviors", Polymers **11**, 1456 (2019).

[110] M. Kuzmanovic, L. Delva, D. Mi, C. I. Martins, L. Cardon, and K. Ragaert, "Development of crystalline morphology and its relationship with mechanical properties of PP/PET microfibrillar composites containing POE and POE-g-MA", Polymers **10**, 291 (2018).

[111] M. S. Lima, A. A. Matias, J. R. C. Costa, A. C. Fonseca, J. F. J. Coelho, and A. C. Serra, "Glycidyl methacrylate-based copolymers as new compatibilizers for polypropylene/polyethylene terephthalte blends", J. Polym. Res. **26**, 127 (2019).

[112] L. M. G. Araujo and A. R. Morales, "Compatibilizatino of recycled polypropylene and recycled poly(ethylene terephthalate) blends with SEBS-g-MA", Polimeros **28**, 84–91 (2018).

[113] A. P. A. de Carvalho and A. dS. Sirqueira, "Effect of compatibilization in situ on PA/SEBS blends", Polimeros **26**, 123–128 (2016).

[114] R. E. Wetton, R. D. L. Marsh, and J. G. Van-de-Velde, "Theory and application of dynamic mechanical thermal analysis", Thermochim. Acta **175**, 1–11 (1991).

[115] A. Lamri, M. Shirinbayan, M. Pereira, L. Truffault, J. Fitoussi, S. Lamouri, F. Bakir, and A. Tcharkhtchi, "Effects of strain rate and temperature on the mechanical behaviour of high-density polyethylene", J. Appl. Polym. Sci. **137**, 48778 (2020).

[116] Y. Zhu, C. Liang, Y. Bo, and S. Xu, "Compatibilization of polypropylene/recycled polyethylene terephthalate blends with maleic anhydride grafted polypropylene in the presence of diallyl phthalate", J. Polym. Res. **22**, 35 (2015).

[117] A. A. Matias, M. S. Lima, J. Pereira, P. Pereira, R. Barros, J. F. Coelho, and A. C. Serra, "Use of recycled polypropylene/poly(ethylene terephthalate) blends to manufacture water pipes: an industrial scale study", Waste Manag. **101**, 250–258 (2020).

[118] X. Yi, L. Xu, Y.-L-Wang, G.-J. Zhong, X. Ji, and Z.-M. Li, "Morphology and properties of isotactic polypropylene/poly(ethylene terephthalate) in situ microfibrillar reinforced blends: influence of viscosity ratio", Eur. Polym. J. **46**, 719–730 (2010).

[119] Y. Wang, D. Mi, L. Delva, L. Cardon, J. Zhang, and K. Ragaert, "New approach to optimize mechanical properties of the immiscible polypropylene/poly(ethylene terephthalate) blend: effect of shish-kebab and core-shell structure", Polymers **10**, 1094 (2018).

[120] W. G. Perkins, "Polymer toughness and impact resistance", Polym. Eng. Sci. **39**, 2445–2460 (1999).

[121] M. Seier, S. Stanic, T. Koch, and V.-M. Archodoulaki, "Effect of different compatibilization systems on the rheological, mechanical and morphological properties of polypropylene/polystyrene blends", Polymers **12**, 2335 (2020).

[122] S. Jose, B. Francis, S. Thomas, and J. Karger-Kocsis, "Morphology and mechanical properties of polyamide 12/polypropylene blends in presence and absence of reactive compatibiliser", Polymer **47**, 3874–3888 (2006).

[123] N. C. Abdul Razak, I. M. Inuwa, A. Hassan, and S. A. Samsudin, "Effects of compatibilizers on mechanical properties of PET/PP blend", Compos. Interfaces **20**, 507–515 (2013).

[124] M. K. Razavi Aghjeh, M. Khodabandelou, and M. Khezrefaridi, "Rheology and morphology of high impact polystyrene/polyethylene blends and the effect of compatibilization on their properties", J. Polym. Sci. **114**, 2235–2245 (2009).

[125] N. Mekhilef, B. D. Favis, and P. J. Carreau, "Morphological stability, interfacial tension, and dual-phase continuity in polystyrene-polyethylene blends", J. Polym. Sci. B Polym. Phys. **35**, 293–308 (1997).

[126] T. S. Omonov, C. Harrats, G. Groeninckx, and P. Moldenaers, "Anisotropy and instability of the co-continuous phase morphology in uncompatibilized and reactively compatibilized polypropylene/polystyrene blends", Polymer **48**, 5289–5302 (2007).

[127] J. O. Iroh, "Poly(ethylene terephthalate)", in *Polymer Data Handbook*, edited by J. E. Mark, 2nd ed. (Oxford University Press, Inc., 1999), p. 558.

[128] Y.-Z. Wang, "Solubility parameters of poly(sulfonyldiphenylene phenylphosphonate) and its miscibility with poly(ethylene terephthalate)", J. Polym. Sci. B Polym. Phys. **41**, 2296–2301 (2003).

[129] Y. Fu, L. Liao, Y. Lan, L. Yang, L. Mei, Y. Liu, and S. Hu, "Molecular dynamics and mesoscopic dynamics simulations for prediction of miscibility in polypropylene/polyamide-11 blends", J. Mol. Struct. **1012**, 113–118 (2012).

[130] S. L. Duncan and R. G. Larson, "Comparing experimental and simulated pressure-area isotherms for DPPC", Biophys. J. **94**, 2965–2986 (2008).

[131] H. Liu, Y. Li, W. E. Krause, O. J. Rojas, and M. A. Pasquinelli, "The soft-confined method for creating molecular models of amorphous polymer surfaces", J. Phys. Chem. B **116**, 1570–1578 (2012).

[132] A. Gooneie, J. Gonzalez-Gutierrez, and C. Holzer, "Atomistic modelling of confined polypropylene chains between ferric oxide substrates at melt temperature", Polymers **8**, 361 (2016).

[133]P. Gestoso and J. Brisson, "Effect of hydrogen bonds on the amorphous phase of a polymer as determined by atomistic molecular modelling", Comput. Theor. Polym. Sci. **11**, 263–271 (2001).

[134]J.-L. Barrat, J. Baschnagel, and A. Lyulin, "Molecular dynamics simulations of glassy polymers", Soft Matter **6**, 3430–3446 (2010).

[135]J. Han, R. H. Gee, and R. H. Boyd, "Glass transition temperatures of polymers from molecular dynamics simulations", Macromolecules **27**, 7781–7784 (1994).

[136]N. Metatla and A. Soldera, "Computation of densities, bulk moduli and glass transition temperatures of vinylic polymers from atomistic simulation", Mol. Simul. **32**, 1187–1193 (2006).

[137]C. T. Moynihan, A. J. Easteal, and J. Wilder, "Dependence of the glass transition temperature on heating and cooling rate", J. Phys. Chem. **78**, 2673–2677 (1974).

[138]V. Thirtha, R. Lehman, and T. Nosker, "Glass transition effects in immiscible polymer blends", ANTEC Conference proceedings **6**, 2380–2384 (2005).

[139]D. V. Howe, "Polypropylene, isotactic", in *Polymer Data Handbook*, edited by J. E. Mark, 2nd ed. (Oxford University Press, Inc., 1999), p. 782.

[140]I. Okazaki and B. Wunderlich, "Modulated differential scanning calorimetry in the glass transition region. V. Activation energies and relaxation times of poly(ethylene terephthalate)s", J. Polym. Sci. B Polym. Phys. **34**, 2941–2952 (1996).

[141]Y. Wang, W. Wang, Z. Zhang, L. Xu, and P. Li, "Study of the glass transition temperature and the mechanical properties of PET/modified silica nanocomposite by molecular dynamics simulation", Eur. Polym. J. **75**, 36–45 (2016).

[142]M. Mohammadi, H. Fazli, M. Karevan, and J. Davoodi, "The glass transition temperature of PMMA: A molecular dynamics study and comparison of various determination methods", Eur. Polym. J. **91**, 121–133 (2017).

[143]K. Yu, Z. Li, and J. Sun, "Polymer structures and glass transition: A molecular dynamics simulation study", Macromol. Theory Simul. **10**, 624–633 (2001).

[144]T. W. Sirk, K. S. Khare, M. Karim, J. L. Lenhart, J. W. Andzelm, G. B. McKenna, and R. Khare, "High strain rate mechanical properties of a cross-linked epoxy across the glass transition", Polymer **54**, 7048–7057 (2013).

[145]P. Gestoso and J. Brisson, "Towards the simulation of poly(vinyl phenol)/poly(vinyl methyl ether) blends by atomistic molecular modelling", Polymer **44**, 2321–2329 (2003).

[146]G. W. Longman, R. P. Sheldon, and G. D. Wignall, "Investigation of short range ordering in polymers by means of radial distribution functions derived from x-ray diffraction. Part 2 *Polyethylene terephthalate*", J. Mater. Sci. **11**, 1339–1346 (1976).

[147]P.-G. de Gennes, *Scaling concepts in polymer physics*, 1st ed. (Cornell University Press, 1979) Chap. 8, pp. 223–227.

Appendix A

COMPASS Forcefield

The functional form of the COMPASS forcefield, as given by H. Sun [56], is

$$
\begin{aligned}
E_{total} = &\sum_b \left[k_2(b - b_0)^2 + k_3(b - b_0)^3 + k_4(b - b_0)^4 \right] + \\
&\sum_\theta \left[k_2(\theta - \theta_0)^2 + k_3(\theta - \theta_0)^3 + k_4(\theta - \theta_0)^4 \right] + \\
&\sum_\phi \left[k_1(1 - \cos\phi) + k_2(1 - \cos 2\phi) + k_3(1 - \cos 3\phi) \right] + \sum_\chi k_2\chi^2 + \\
&\sum_{b,b'} k(b - b_0)(b' - b_0') + \sum_{b,\theta} k(b - b_0)(\theta - \theta_0) + \\
&\sum_{b,\phi} (b - b_0) \left[k_1 \cos\phi + k_2 \cos 2\phi + k_3 \cos 3\phi \right] + \\
&\sum_{\theta,\phi} (\theta - \theta_0) \left[k_1 \cos\phi + k_2 \cos 2\phi + k_3 \cos 3\phi \right] + \sum_{\theta,\theta'} k(\theta' - \theta_0')(\theta - \theta_0) + \\
&\sum_{\theta,\theta',\phi} k(\theta' - \theta_0')(\theta - \theta_0) \cos\phi + \\
&\sum_{i,j} \frac{q_i q_j}{r_{ij}} + \sum_{i,j} \epsilon_{ij} \left[2 \left(\frac{r_{ij}^\circ}{r_{ij}} \right)^9 - 3 \left(\frac{r_{ij}^\circ}{r_{ij}} \right)^6 \right].
\end{aligned}
$$

The valence terms represent internal coordinates of bonds (b), bond angle (θ), torsion angle (ϕ), and out-of-plane angle (χ). The cross-coupling terms include combinations of two or three internal coordinates. The nonbond interactions include (1) a Coulombic function for electrostatic interactions between pairs of atoms separated by two or more intervening atoms or those that belong to different molecules; (2) a Lennard-Jones (LJ) 9-6 function which is comparatively softer in the repulsion region than the LJ 12-6 function. For a more thorough explanation of the parameters, the reader is referred to [56].

Appendix B

Molecular Dynamics Simulations Equilibration
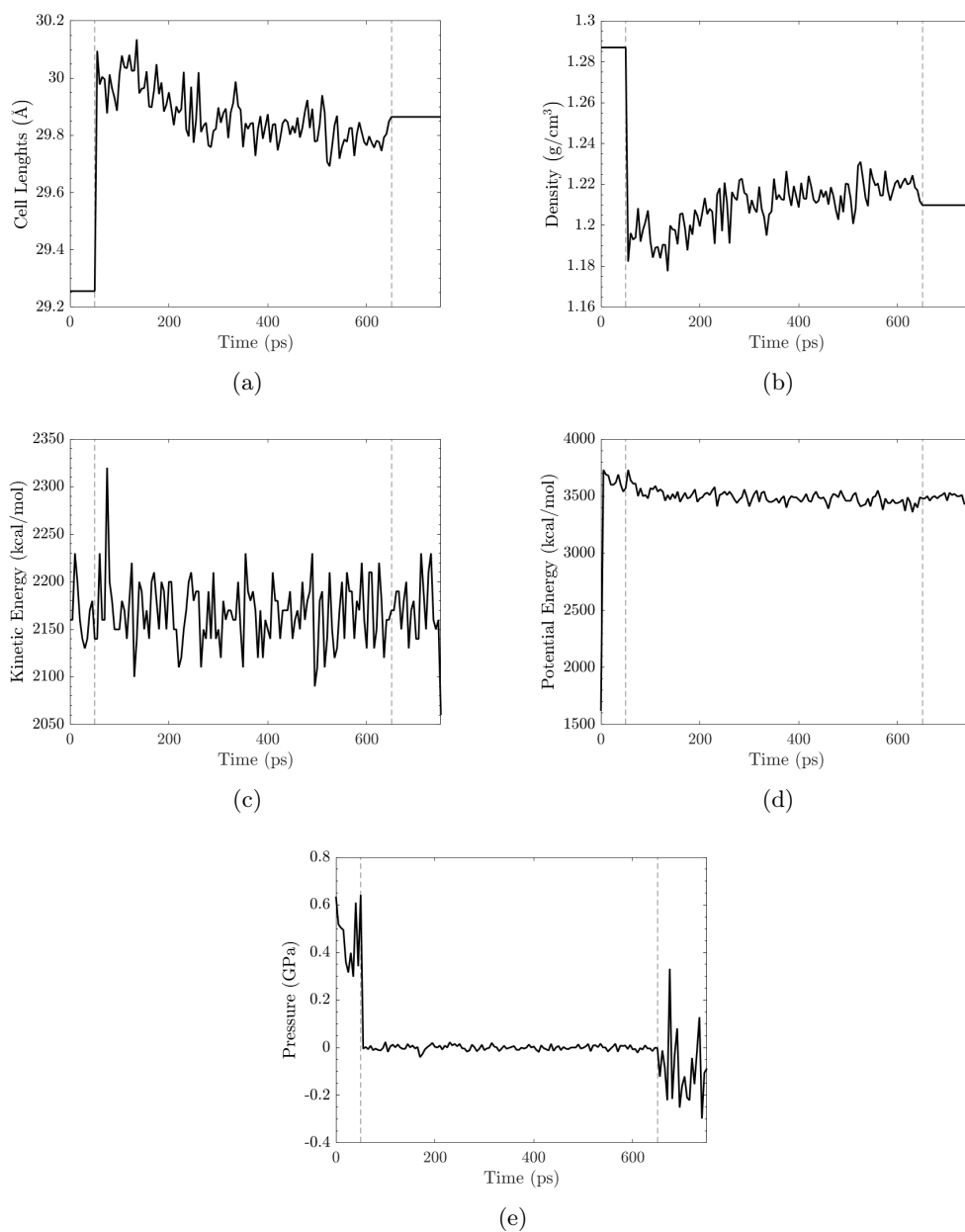
FIGURE B.1: Various intensive and extensive properties as a function of time for one of the PP10/PET90 blend structures, namely; cell lengths (a), density (b), total kinetic energy (c), total potential energy (d), and pressure (e). The data between the vertical dashed lines was obtained from NPT-equilibration dynamics while the left-most data is from the 50 ps NVT-equilibration after annealing. The remaining right-most data was obtained during the NVT-production run.

Appendix C

Fibrillar Surface of rPPC/PET/X Blends
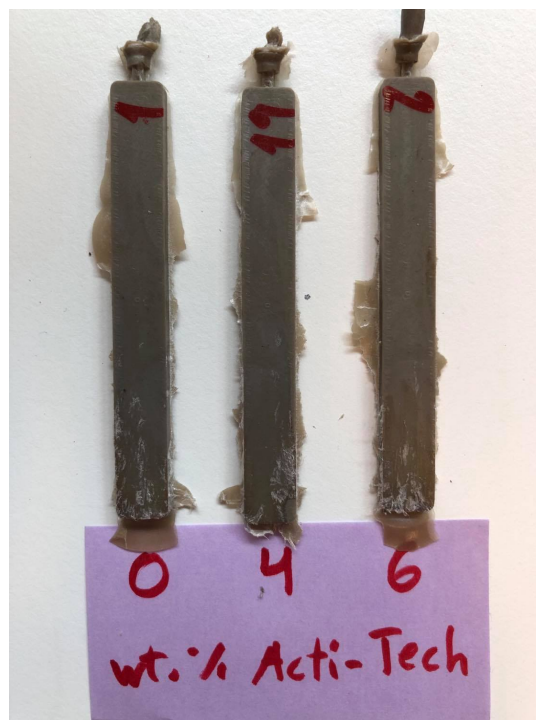
FIGURE C.1: Examples of rPPC/PET/0, rPPC/PET/4 and rPPC/PET/6 blends with the observed frayed and fibrillar surface.

Appendix D

DSC Curves
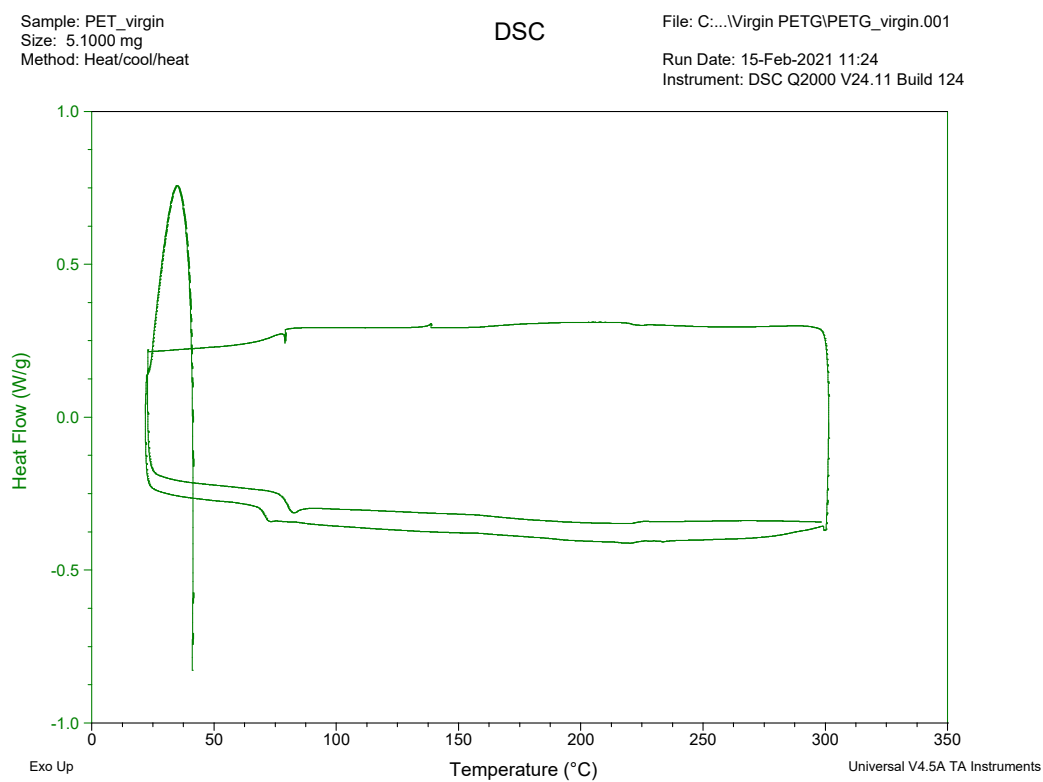
FIGURE D.1: DSC heat/cool/heat of virgin PETG performed at a rate of 10 °C/min.
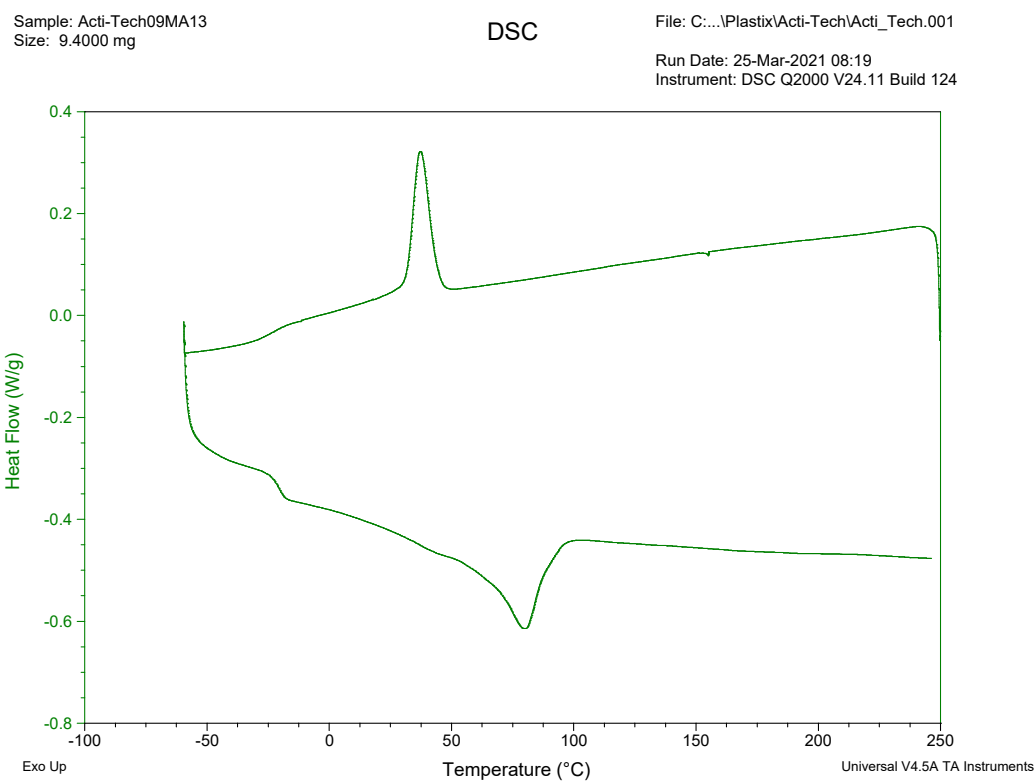
FIGURE D.2: DSC thermogram of cooling and second heating of the Acti-Tech 09MA13 compatibilizer, performed at a heating rate of 10 °C/min and a cooling rate of 5 °C/min.

Appendix E

Complex Viscosities of PP and PETG
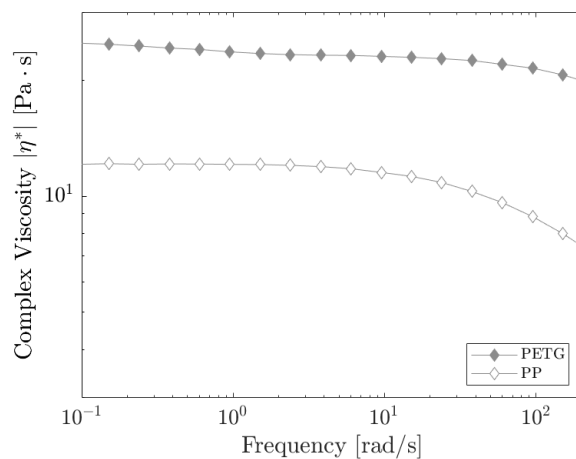
FIGURE E.1: Complex viscosity of twice extruded PP and PETG at a temperature of 250 °C (LT). Lines are a guide to the eye.
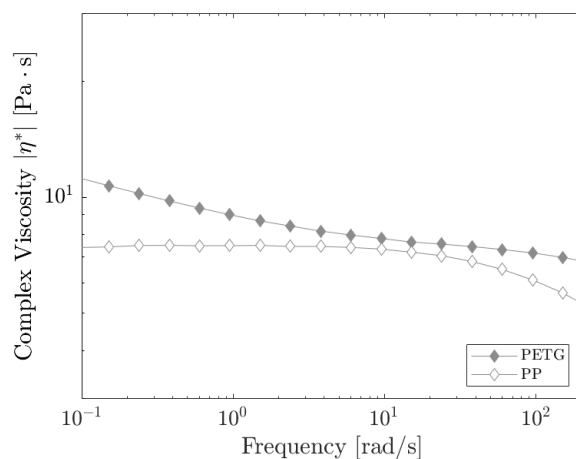
FIGURE E.2: Complex viscosity of twice extruded PP and PETG at a temperature of 260 °C (HT). Lines are a guide to the eye.

Appendix F

Hot-Stage Microscopy of PP/PETG Blends
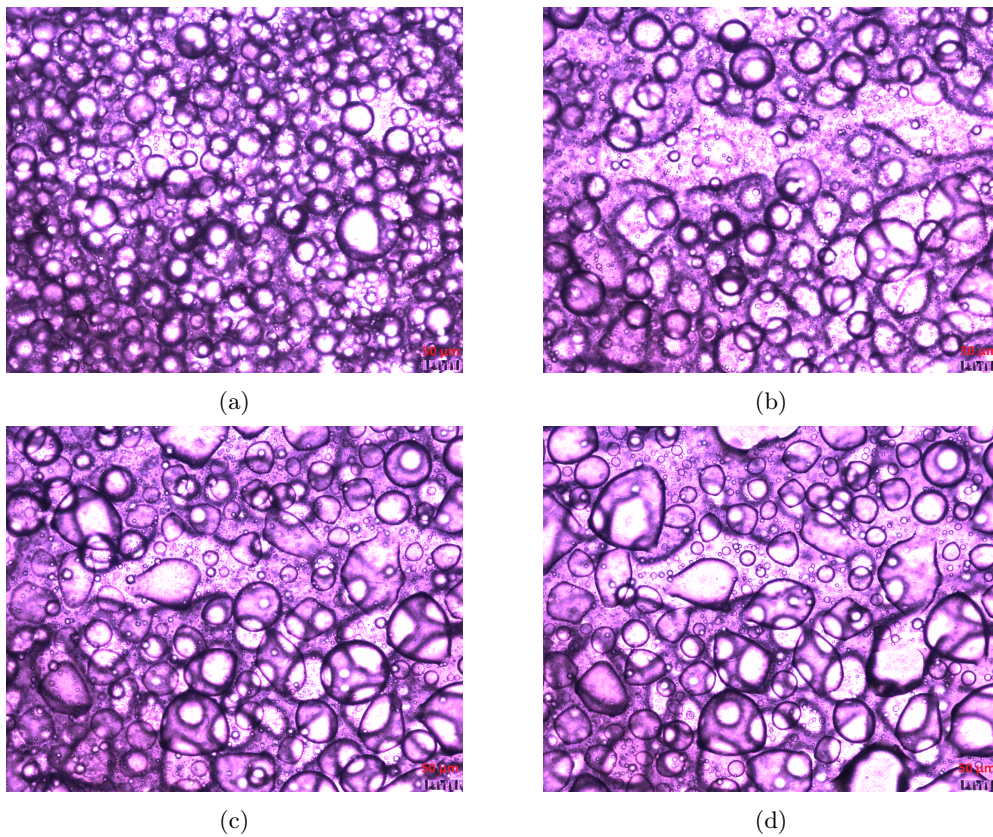
FIGURE F.1: Polarized light images of the PP50/PETG50 HT blend with ×10 magnification at 260 °C after 15 min (a), 30 min (b), 45 min (c), and 60 min (d).
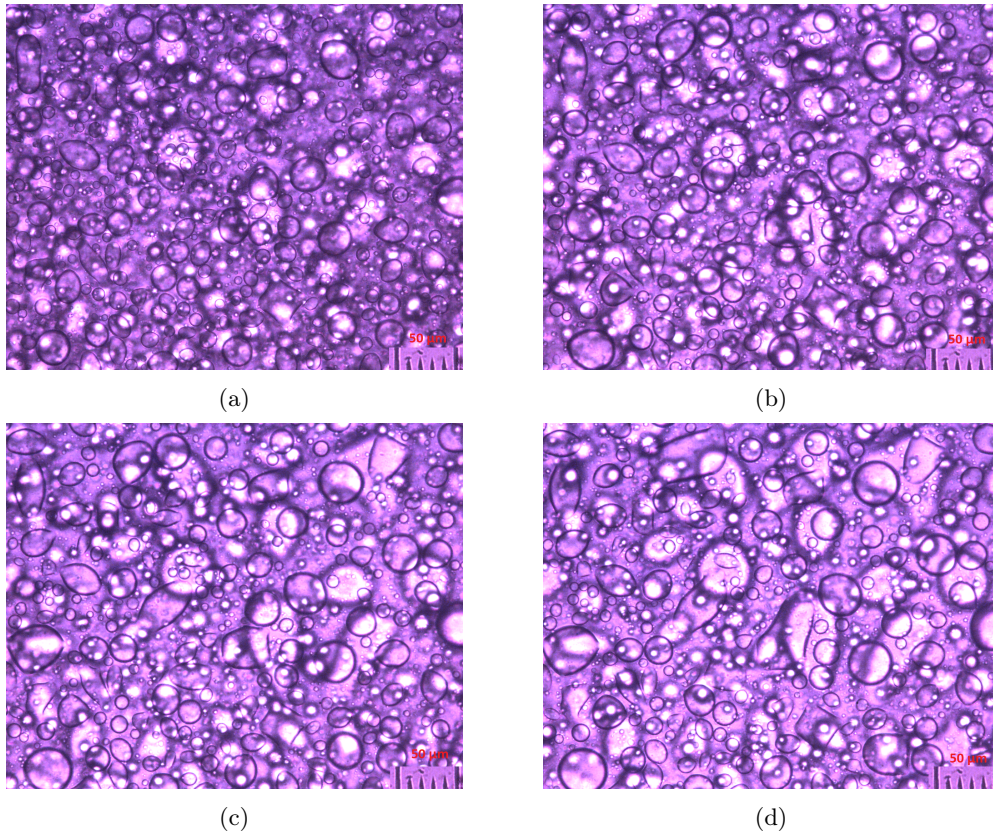
FIGURE F.2: Polarized light images of the PP75/PETG25 HT blend with ×20 magnification at 260 °C after 15 min (a), 30 min (b), 45 min (c), and 60 min (d).

(a)   (b)

(c)   (d)
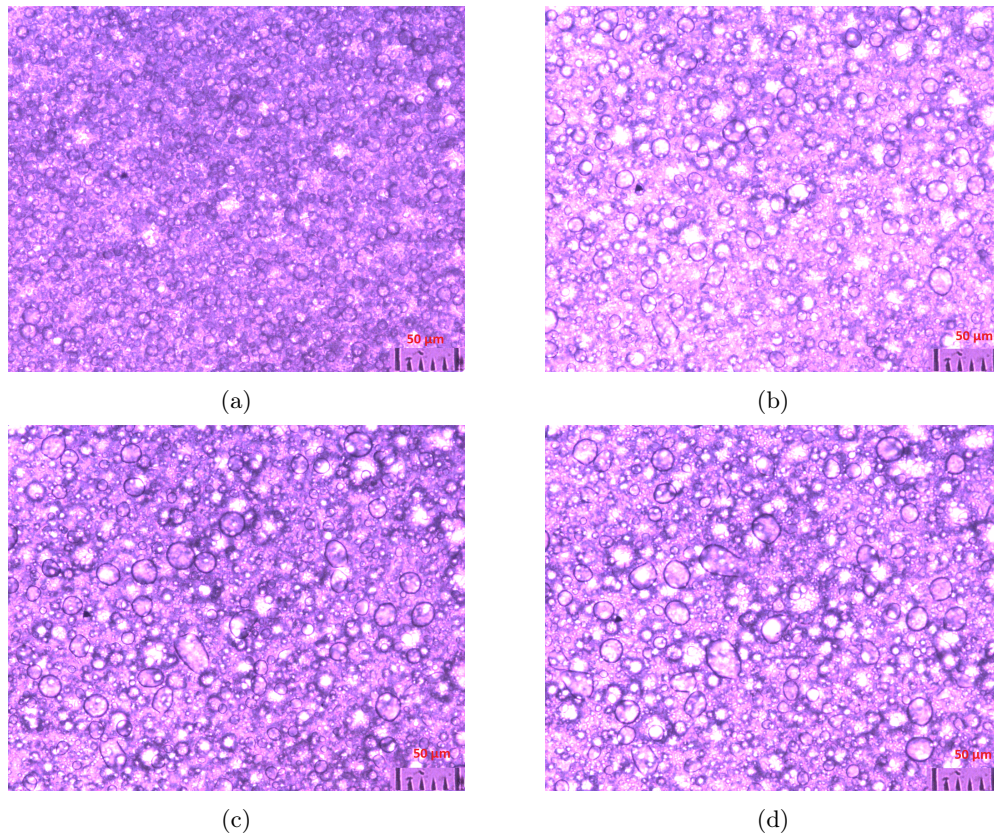
FIGURE F.3: Polarized light images of the PP75/PETG25 LT blend with ×20 magnification at 250 °C after 15 min (a), 30 min (b), 45 min (c), and 60 min (d).
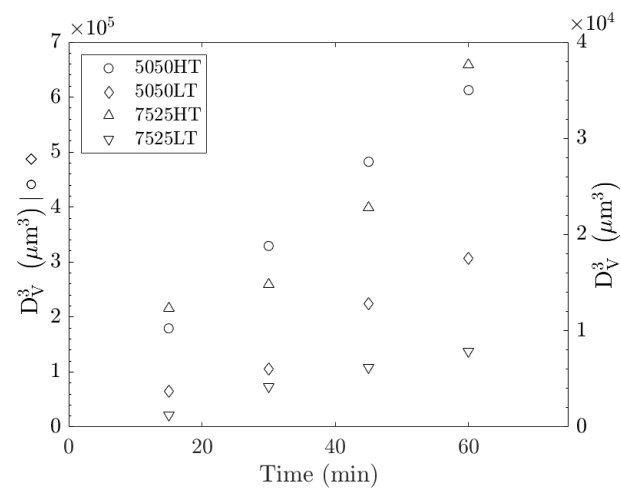
FIGURE F.4: Time evolution of the volumetric average droplet diameter cubed from the melt micrographs. The left y-axis relates to values obtained on the PP50/PETG50 HT and LT blends, while the right y-axis represents values from the PP75/PETG25 HT and LT blends.

Appendix G

DMA on rPPC

In Fig. G.1 the data obtained on piston injection molded OceanIX rPPC, supplied by Plastix, is shown. The OceanIX rPPC contains 70 % PP and 30 % HDPE similarly to the rPPC mentioned in the report.
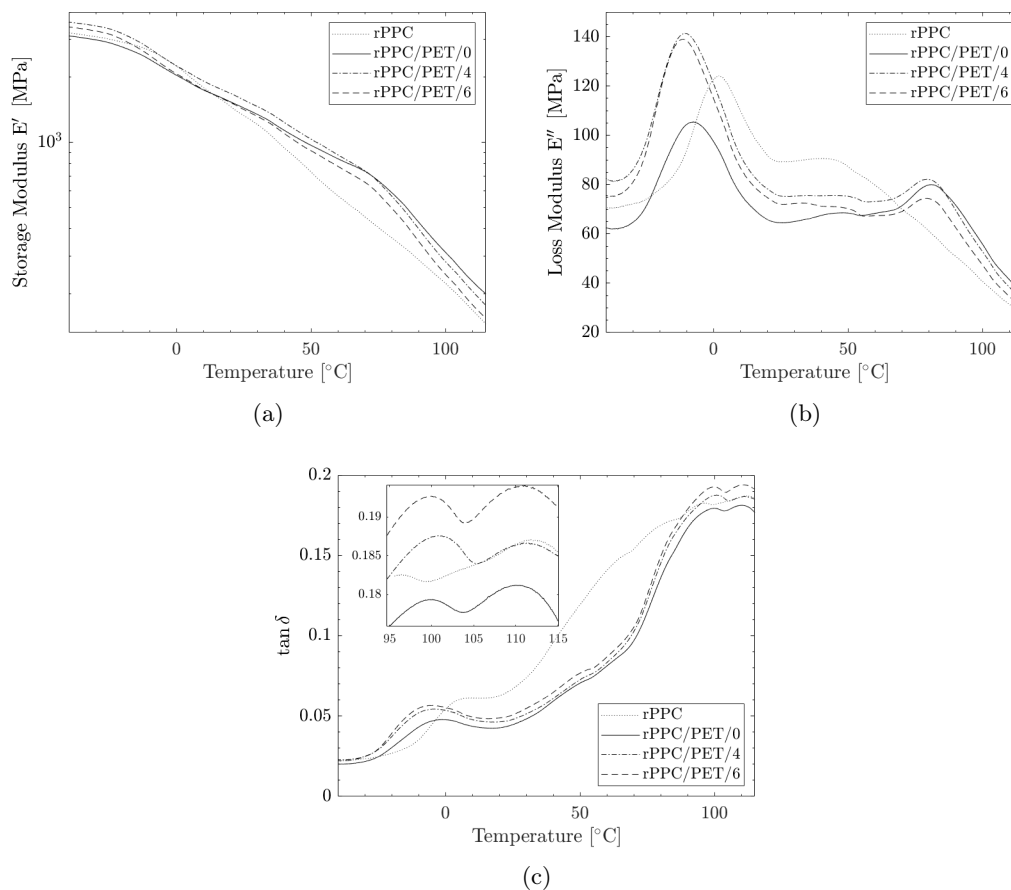
FIGURE G.1: The storage moduli E' (a), loss moduli E" (b), and $\tan \delta$ (c) for a non-extruded rPPC and the rPPC/PET blends with various added compatibilizer contents.

Appendix H

Berendsen Decay Constant
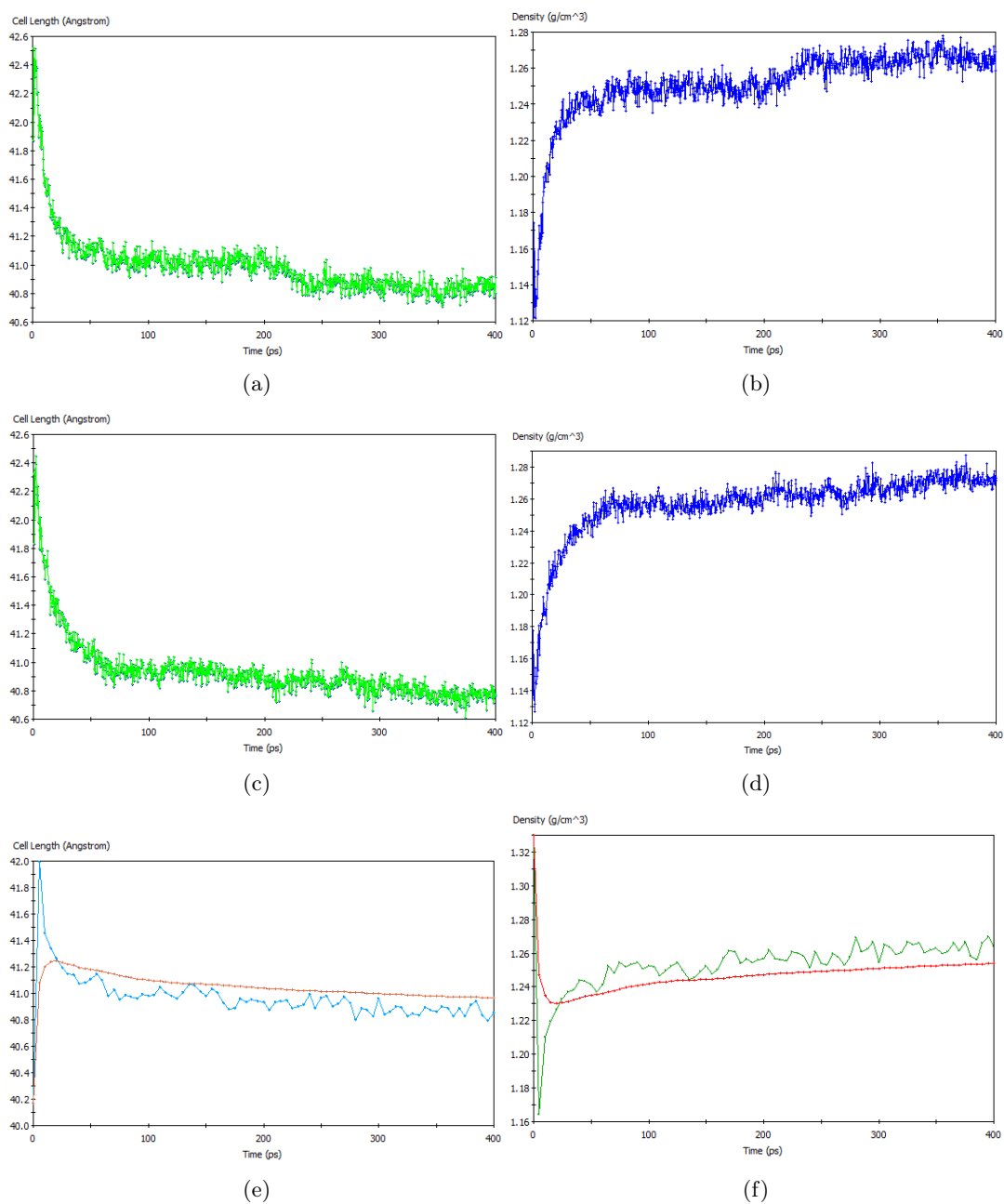
FIGURE H.1: Continued on next page.

(g)

(h)

(i)

(j)
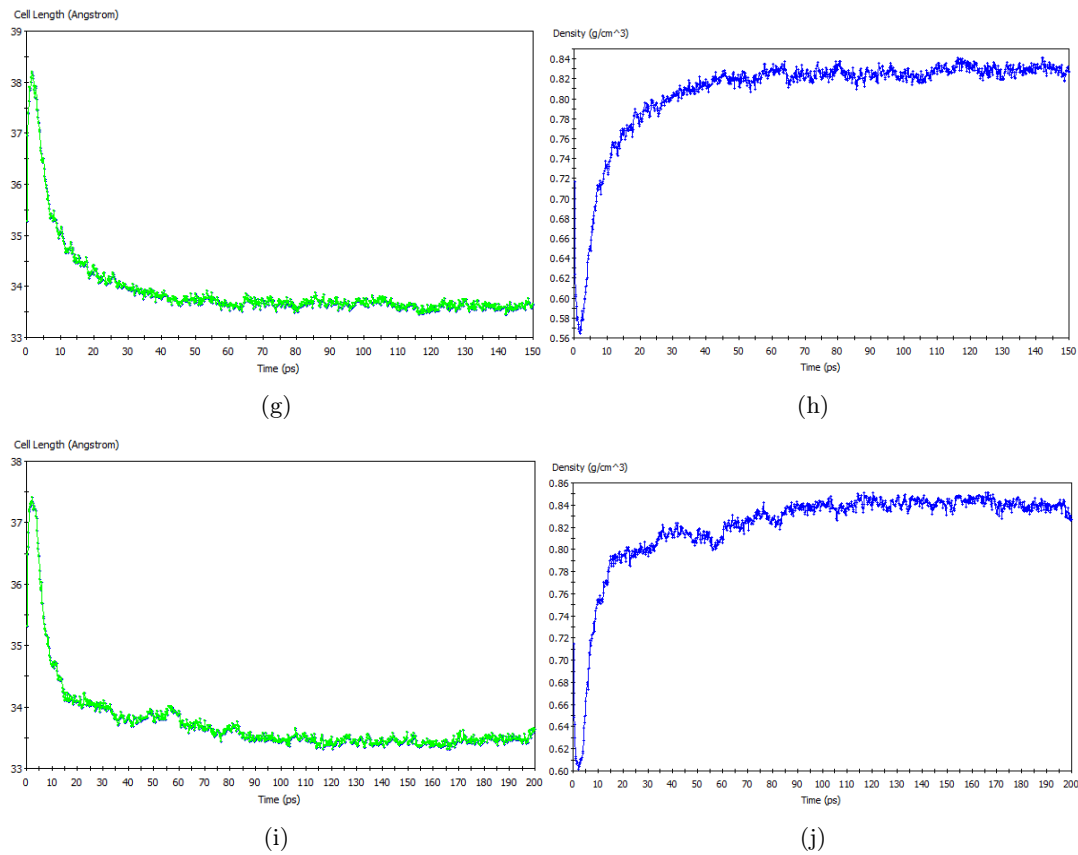
FIGURE H.1: The time evolution of cell lengths and densities for PET (a-f) and PP (g-j) obtained from NPT-dynamics with a pressure of 1 bar controlled by the Berendsen barostat, and a temperature of 298 K controlled by the Nosé-Hoover-Langevin thermostat. Decay constants were 0.025 ps (a,b), 0.05 ps (c,d,g,h) and 0.1 ps (e,f,i,j). The red line in (e,f) is a running average while the blue and green are the measured profiles.

Appendix I

Licenses to Reproduce Figures

Figure 2.3 from P. Van Puyvelde et al.

ELSEVIER LICENSE
TERMS AND CONDITIONS

May 25, 2021

This Agreement between Mr. Thomas Larsen ("You") and Elsevier ("Elsevier") consists of your license details and the terms and conditions provided by Elsevier and Copyright Clearance Center.

License Number	5075800855001
License date	May 25, 2021
Licensed Content Publisher	Elsevier
Licensed Content Publication	Current Opinion in Colloid & Interface Science
Licensed Content Title	Rheology and morphology of compatibilized polymer blends
Licensed Content Author	Peter Van Puyvelde,Sachin Velankar,Paula Moldenaers
Licensed Content Date	Nov 1, 2001
Licensed Content Volume	6
Licensed Content Issue	5-6
Licensed Content Pages	7
Start Page	457
End Page	463
Type of Use	reuse in a thesis/dissertation
Portion	figures/tables/illustrations

Number of figures/tables/illustrations	1
Format	electronic
Are you the author of this Elsevier article?	No
Will you be translating?	No
Title	Processing, Compatibilization and Modelling of Immiscible Polyolefin/Copolyester Blends
Institution name	Aalborg University
Expected presentation date	Jun 2021
Portions	The schematic showing coalescence suppresion: Fig. 3 on page 4.
Requestor Location	Mr. Thomas Larsen Langagervej 4, 1. 227 Lindholmsvej 134A, Nørresundby Aalborg Øst, No states available 9220 Denmark Attn: Mr. Thomas Larsen
Publisher Tax ID	GB 494 6272 12
Total	0.00 EUR

Terms and Conditions

INTRODUCTION

1. The publisher for this copyrighted material is Elsevier. By clicking "accept" in connection with completing this licensing transaction, you agree that the following terms and conditions apply to this transaction (along with the Billing and Payment terms and conditions established by Copyright Clearance Center, Inc. ("CCC"), at the time that you opened your Rightslink account and that are available at any time at http://myaccount.copyright.com).

GENERAL TERMS

2. Elsevier hereby grants you permission to reproduce the aforementioned material subject to the terms and conditions indicated.

3. Acknowledgement: If any part of the material to be used (for example, figures) has appeared in our publication with credit or acknowledgement to another source, permission must also be sought from that source. If such permission is not obtained then that material may not be included in your publication/copies. Suitable acknowledgement to the source must be made, either as a footnote or in a reference list at the end of your publication, as follows:

"Reprinted from Publication title, Vol /edition number, Author(s), Title of article / title of chapter, Pages No., Copyright (Year), with permission from Elsevier [OR APPLICABLE SOCIETY COPYRIGHT OWNER]." Also Lancet special credit - "Reprinted from The Lancet, Vol. number, Author(s), Title of article, Pages No., Copyright (Year), with permission from Elsevier."

4. Reproduction of this material is confined to the purpose and/or media for which permission is hereby given.

5. Altering/Modifying Material: Not Permitted. However figures and illustrations may be altered/adapted minimally to serve your work. Any other abbreviations, additions, deletions and/or any other alterations shall be made only with prior written authorization of Elsevier Ltd. (Please contact Elsevier's permissions helpdesk here). No modifications can be made to any Lancet figures/tables and they must be reproduced in full.

6. If the permission fee for the requested use of our material is waived in this instance, please be advised that your future requests for Elsevier materials may attract a fee.

7. Reservation of Rights: Publisher reserves all rights not specifically granted in the combination of (i) the license details provided by you and accepted in the course of this licensing transaction, (ii) these terms and conditions and (iii) CCC's Billing and Payment terms and conditions.

8. License Contingent Upon Payment: While you may exercise the rights licensed immediately upon issuance of the license at the end of the licensing process for the transaction, provided that you have disclosed complete and accurate details of your proposed use, no license is finally effective unless and until full payment is received from you (either by publisher or by CCC) as provided in CCC's Billing and Payment terms and conditions. If full payment is not received on a timely basis, then any license preliminarily granted shall be deemed automatically revoked and shall be void as if never granted. Further, in the event that you breach any of these terms and conditions or any of CCC's Billing and Payment terms and conditions, the license is automatically revoked and shall be void as if never granted. Use of materials as described in a revoked license, as well as any use of the materials beyond the scope of an unrevoked license, may constitute copyright infringement and publisher reserves the right to take any and all action to protect its copyright in the materials.

9. Warranties: Publisher makes no representations or warranties with respect to the licensed material.

10. Indemnity: You hereby indemnify and agree to hold harmless publisher and CCC, and their respective officers, directors, employees and agents, from and against any and all claims arising out of your use of the licensed material other than as specifically authorized pursuant to this license.

11. No Transfer of License: This license is personal to you and may not be sublicensed, assigned, or transferred by you to any other person without publisher's written permission.

12. No Amendment Except in Writing: This license may not be amended except in a writing signed by both parties (or, in the case of publisher, by CCC on publisher's behalf).

13. Objection to Contrary Terms: Publisher hereby objects to any terms contained in any purchase order, acknowledgment, check endorsement or other writing prepared by you, which terms are inconsistent with these terms and conditions or CCC's Billing and Payment terms and conditions. These terms and conditions, together with CCC's Billing and Payment terms and conditions (which are incorporated herein), comprise the entire agreement between you and publisher (and CCC) concerning this licensing transaction. In the event of any conflict between your obligations established by these terms and conditions and those established by CCC's Billing and Payment terms and conditions, these terms and conditions shall control.

14. Revocation: Elsevier or Copyright Clearance Center may deny the permissions described in this License at their sole discretion, for any reason or no reason, with a full refund payable to you. Notice of such denial will be made using the contact information provided by you. Failure to receive such notice will not alter or invalidate the denial. In no event will Elsevier or Copyright Clearance Center be responsible or liable for any costs, expenses or damage incurred by you as a result of a denial of your permission request, other than a refund of the amount(s) paid by you to Elsevier and/or Copyright Clearance Center for denied permissions.

LIMITED LICENSE

The following terms and conditions apply only to specific license types:

15. **Translation**: This permission is granted for non-exclusive world **English** rights only unless your license was granted for translation rights. If you licensed translation rights you may only translate this content into the languages you requested. A professional translator must perform all translations and reproduce the content word for word preserving the integrity of the article.

16. **Posting licensed content on any Website**: The following terms and conditions apply as follows: Licensing material from an Elsevier journal: All content posted to the web site must maintain the copyright information line on the bottom of each image; A hyper-text must be included to the Homepage of the journal from which you are licensing at http://www.sciencedirect.com/science/journal/xxxxx or the Elsevier homepage for books at http://www.elsevier.com; Central Storage: This license does not include permission for a scanned version of the material to be stored in a central repository such as that provided by Heron/XanEdu.

Licensing material from an Elsevier book: A hyper-text link must be included to the Elsevier homepage at http://www.elsevier.com . All content posted to the web site must maintain the copyright information line on the bottom of each image.

Posting licensed content on Electronic reserve: In addition to the above the following clauses are applicable: The web site must be password-protected and made available only to bona fide students registered on a relevant course. This permission is granted for 1 year only. You may obtain a new license for future website posting.

17. **For journal authors:** the following clauses are applicable in addition to the above:

Preprints:

A preprint is an author's own write-up of research results and analysis, it has not been peer-reviewed, nor has it had any other value added to it by a publisher (such as formatting, copyright, technical enhancement etc.).

Authors can share their preprints anywhere at any time. Preprints should not be added to or enhanced in any way in order to appear more like, or to substitute for, the final versions of

articles however authors can update their preprints on arXiv or RePEc with their Accepted Author Manuscript (see below).

If accepted for publication, we encourage authors to link from the preprint to their formal publication via its DOI. Millions of researchers have access to the formal publications on ScienceDirect, and so links will help users to find, access, cite and use the best available version. Please note that Cell Press, The Lancet and some society-owned have different preprint policies. Information on these policies is available on the journal homepage.

Accepted Author Manuscripts: An accepted author manuscript is the manuscript of an article that has been accepted for publication and which typically includes author-incorporated changes suggested during submission, peer review and editor-author communications.

Authors can share their accepted author manuscript:

- immediately
    - via their non-commercial person homepage or blog
    - by updating a preprint in arXiv or RePEc with the accepted manuscript
    - via their research institute or institutional repository for internal institutional uses or as part of an invitation-only research collaboration work-group
    - directly by providing copies to their students or to research collaborators for their personal use
    - for private scholarly sharing as part of an invitation-only work group on commercial sites with which Elsevier has an agreement
- After the embargo period
    - via non-commercial hosting platforms such as their institutional repository
    - via commercial sites with which Elsevier has an agreement

In all cases accepted manuscripts should:

- link to the formal publication via its DOI
- bear a CC-BY-NC-ND license - this is easy to do
- if aggregated with other manuscripts, for example in a repository or other site, be shared in alignment with our hosting policy not be added to or enhanced in any way to appear more like, or to substitute for, the published journal article.

Published journal article (JPA): A published journal article (PJA) is the definitive final record of published research that appears or will appear in the journal and embodies all value-adding publishing activities including peer review co-ordination, copy-editing, formatting, (if relevant) pagination and online enrichment.

Policies for sharing publishing journal articles differ for subscription and gold open access articles:

Subscription Articles: If you are an author, please share a link to your article rather than the full-text. Millions of researchers have access to the formal publications on ScienceDirect, and so links will help your users to find, access, cite, and use the best available version.

Theses and dissertations which contain embedded PJAs as part of the formal submission can be posted publicly by the awarding institution with DOI links back to the formal publications on ScienceDirect.

If you are affiliated with a library that subscribes to ScienceDirect you have additional private sharing rights for others' research accessed under that agreement. This includes use for classroom teaching and internal training at the institution (including use in course packs and courseware programs), and inclusion of the article for grant funding purposes.

Gold Open Access Articles: May be shared according to the author-selected end-user license and should contain a CrossMark logo, the end user license, and a DOI link to the formal publication on ScienceDirect.

Please refer to Elsevier's posting policy for further information.

18. **For book authors** the following clauses are applicable in addition to the above: Authors are permitted to place a brief summary of their work online only. You are not allowed to download and post the published electronic version of your chapter, nor may you scan the printed edition to create an electronic version. **Posting to a repository:** Authors are permitted to post a summary of their chapter only in their institution's repository.

19. **Thesis/Dissertation**: If your license is for use in a thesis/dissertation your thesis may be submitted to your institution in either print or electronic form. Should your thesis be published commercially, please reapply for permission. These requirements include permission for the Library and Archives of Canada to supply single copies, on demand, of the complete thesis and include permission for Proquest/UMI to supply single copies, on demand, of the complete thesis. Should your thesis be published commercially, please reapply for permission. Theses and dissertations which contain embedded PJAs as part of the formal submission can be posted publicly by the awarding institution with DOI links back to the formal publications on ScienceDirect.

Elsevier Open Access Terms and Conditions

You can publish open access with Elsevier in hundreds of open access journals or in nearly 2000 established subscription journals that support open access publishing. Permitted third party re-use of these open access articles is defined by the author's choice of Creative Commons user license. See our open access license policy for more information.

Terms & Conditions applicable to all Open Access articles published with Elsevier:

Any reuse of the article must not represent the author as endorsing the adaptation of the article nor should the article be modified in such a way as to damage the author's honour or reputation. If any changes have been made, such changes must be clearly indicated.

The author(s) must be appropriately credited and we ask that you include the end user license and a DOI link to the formal publication on ScienceDirect.

If any part of the material to be used (for example, figures) has appeared in our publication with credit or acknowledgement to another source it is the responsibility of the user to ensure their reuse complies with the terms and conditions determined by the rights holder.

Additional Terms & Conditions applicable to each Creative Commons user license:

CC BY: The CC-BY license allows users to copy, to create extracts, abstracts and new works from the Article, to alter and revise the Article and to make commercial use of the Article (including reuse and/or resale of the Article by commercial entities), provided the user gives appropriate credit (with a link to the formal publication through the relevant DOI), provides a link to the license, indicates if changes were made and the licensor is not represented as endorsing the use made of the work. The full details of the license are available at http://creativecommons.org/licenses/by/4.0.

CC BY NC SA: The CC BY-NC-SA license allows users to copy, to create extracts, abstracts and new works from the Article, to alter and revise the Article, provided this is not done for commercial purposes, and that the user gives appropriate credit (with a link to the formal publication through the relevant DOI), provides a link to the license, indicates if changes were made and the licensor is not represented as endorsing the use made of the

work. Further, any new works must be made available on the same conditions. The full details of the license are available at http://creativecommons.org/licenses/by-nc-sa/4.0.

CC BY NC ND: The CC BY-NC-ND license allows users to copy and distribute the Article, provided this is not done for commercial purposes and further does not permit distribution of the Article if it is changed or edited in any way, and provided the user gives appropriate credit (with a link to the formal publication through the relevant DOI), provides a link to the license, and that the licensor is not represented as endorsing the use made of the work. The full details of the license are available at http://creativecommons.org/licenses/by-nc-nd/4.0. Any commercial reuse of Open Access articles published with a CC BY NC SA or CC BY NC ND license requires permission from Elsevier and will be subject to a fee.

Commercial reuse includes:

- Associating advertising with the full text of the Article
- Charging fees for document delivery or access
- Article aggregation
- Systematic distribution via e-mail lists or share buttons

Posting or linking by commercial companies for use by customers of those companies.

20. **Other Conditions**:

v1.10

Questions? customercare@copyright.com or +1-855-239-3415 (toll free in the US) or +1-978-646-2777.

Figure 2.4 from J. Maris et al.

ELSEVIER LICENSE
TERMS AND CONDITIONS

May 25, 2021

This Agreement between Mr. Thomas Larsen ("You") and Elsevier ("Elsevier") consists of your license details and the terms and conditions provided by Elsevier and Copyright Clearance Center.

License Number	5075811309741
License date	May 25, 2021
Licensed Content Publisher	Elsevier
Licensed Content Publication	Polymer Degradation and Stability
Licensed Content Title	Mechanical recycling: Compatibilization of mixed thermoplastic wastes
Licensed Content Author	Joachim Maris,Sylvie Bourdon,Jean-Michel Brossard,Laurent Cauret,Laurent Fontaine,Véronique Montembault
Licensed Content Date	Jan 1, 2018
Licensed Content Volume	147
Licensed Content Issue	n/a
Licensed Content Pages	22
Start Page	245
End Page	266
Type of Use	reuse in a thesis/dissertation

Portion	figures/tables/illustrations
Number of figures/tables/illustrations	1
Format	electronic
Are you the author of this Elsevier article?	No
Will you be translating?	No
Title	Processing, Compatibilization and Modelling of Immiscible Polyolefin/Copolyester Blends
Institution name	Aalborg University
Expected presentation date	Jun 2021
Portions	Part of "Scheme 2. Reactive functional groups." on page 8.
Requestor Location	Mr. Thomas Larsen Langagervej 4, 1. 227 Lindholmsvej 134A, Nørresundby Aalborg Øst, No states available 9220 Denmark Attn: Mr. Thomas Larsen
Publisher Tax ID	GB 494 6272 12
Total	0.00 USD

Terms and Conditions

INTRODUCTION

1. The publisher for this copyrighted material is Elsevier. By clicking "accept" in connection with completing this licensing transaction, you agree that the following terms and conditions apply to this transaction (along with the Billing and Payment terms and conditions established by Copyright Clearance Center, Inc. ("CCC"), at the time that you opened your Rightslink account and that are available at any time at http://myaccount.copyright.com).

GENERAL TERMS

2. Elsevier hereby grants you permission to reproduce the aforementioned material subject to the terms and conditions indicated.

3. Acknowledgement: If any part of the material to be used (for example, figures) has appeared in our publication with credit or acknowledgement to another source, permission must also be sought from that source. If such permission is not obtained then that material may not be included in your publication/copies. Suitable acknowledgement to the source must be made, either as a footnote or in a reference list at the end of your publication, as follows:

"Reprinted from Publication title, Vol /edition number, Author(s), Title of article / title of chapter, Pages No., Copyright (Year), with permission from Elsevier [OR APPLICABLE SOCIETY COPYRIGHT OWNER]." Also Lancet special credit - "Reprinted from The Lancet, Vol. number, Author(s), Title of article, Pages No., Copyright (Year), with permission from Elsevier."

4. Reproduction of this material is confined to the purpose and/or media for which permission is hereby given.

5. Altering/Modifying Material: Not Permitted. However figures and illustrations may be altered/adapted minimally to serve your work. Any other abbreviations, additions, deletions and/or any other alterations shall be made only with prior written authorization of Elsevier Ltd. (Please contact Elsevier's permissions helpdesk here). No modifications can be made to any Lancet figures/tables and they must be reproduced in full.

6. If the permission fee for the requested use of our material is waived in this instance, please be advised that your future requests for Elsevier materials may attract a fee.

7. Reservation of Rights: Publisher reserves all rights not specifically granted in the combination of (i) the license details provided by you and accepted in the course of this licensing transaction, (ii) these terms and conditions and (iii) CCC's Billing and Payment terms and conditions.

8. License Contingent Upon Payment: While you may exercise the rights licensed immediately upon issuance of the license at the end of the licensing process for the transaction, provided that you have disclosed complete and accurate details of your proposed use, no license is finally effective unless and until full payment is received from you (either by publisher or by CCC) as provided in CCC's Billing and Payment terms and conditions. If full payment is not received on a timely basis, then any license preliminarily granted shall be deemed automatically revoked and shall be void as if never granted. Further, in the event that you breach any of these terms and conditions or any of CCC's Billing and Payment terms and conditions, the license is automatically revoked and shall be void as if never granted. Use of materials as described in a revoked license, as well as any use of the materials beyond the scope of an unrevoked license, may constitute copyright infringement and publisher reserves the right to take any and all action to protect its copyright in the materials.

9. Warranties: Publisher makes no representations or warranties with respect to the licensed material.

10. Indemnity: You hereby indemnify and agree to hold harmless publisher and CCC, and their respective officers, directors, employees and agents, from and against any and all claims arising out of your use of the licensed material other than as specifically authorized pursuant to this license.

11. No Transfer of License: This license is personal to you and may not be sublicensed, assigned, or transferred by you to any other person without publisher's written permission.

12. No Amendment Except in Writing: This license may not be amended except in a writing signed by both parties (or, in the case of publisher, by CCC on publisher's behalf).

13. Objection to Contrary Terms: Publisher hereby objects to any terms contained in any purchase order, acknowledgment, check endorsement or other writing prepared by you, which terms are inconsistent with these terms and conditions or CCC's Billing and Payment terms and conditions. These terms and conditions, together with CCC's Billing and Payment terms and conditions (which are incorporated herein), comprise the entire agreement between you and publisher (and CCC) concerning this licensing transaction. In the event of any conflict between your obligations established by these terms and conditions and those established by CCC's Billing and Payment terms and conditions, these terms and conditions shall control.

14. Revocation: Elsevier or Copyright Clearance Center may deny the permissions described in this License at their sole discretion, for any reason or no reason, with a full refund payable to you. Notice of such denial will be made using the contact information provided by you. Failure to receive such notice will not alter or invalidate the denial. In no event will Elsevier or Copyright Clearance Center be responsible or liable for any costs, expenses or damage incurred by you as a result of a denial of your permission request, other than a refund of the amount(s) paid by you to Elsevier and/or Copyright Clearance Center for denied permissions.

LIMITED LICENSE

The following terms and conditions apply only to specific license types:

15. **Translation**: This permission is granted for non-exclusive world **English** rights only unless your license was granted for translation rights. If you licensed translation rights you may only translate this content into the languages you requested. A professional translator must perform all translations and reproduce the content word for word preserving the integrity of the article.

16. **Posting licensed content on any Website**: The following terms and conditions apply as follows: Licensing material from an Elsevier journal: All content posted to the web site must maintain the copyright information line on the bottom of each image; A hyper-text must be included to the Homepage of the journal from which you are licensing at http://www.sciencedirect.com/science/journal/xxxxx or the Elsevier homepage for books at http://www.elsevier.com; Central Storage: This license does not include permission for a scanned version of the material to be stored in a central repository such as that provided by Heron/XanEdu.

Licensing material from an Elsevier book: A hyper-text link must be included to the Elsevier homepage at http://www.elsevier.com . All content posted to the web site must maintain the copyright information line on the bottom of each image.

Posting licensed content on Electronic reserve: In addition to the above the following clauses are applicable: The web site must be password-protected and made available only to bona fide students registered on a relevant course. This permission is granted for 1 year only. You may obtain a new license for future website posting.

17. **For journal authors:** the following clauses are applicable in addition to the above:

Preprints:

A preprint is an author's own write-up of research results and analysis, it has not been peer-reviewed, nor has it had any other value added to it by a publisher (such as formatting, copyright, technical enhancement etc.).

Authors can share their preprints anywhere at any time. Preprints should not be added to or enhanced in any way in order to appear more like, or to substitute for, the final versions of articles however authors can update their preprints on arXiv or RePEc with their Accepted Author Manuscript (see below).

If accepted for publication, we encourage authors to link from the preprint to their formal publication via its DOI. Millions of researchers have access to the formal publications on ScienceDirect, and so links will help users to find, access, cite and use the best available version. Please note that Cell Press, The Lancet and some society-owned have different preprint policies. Information on these policies is available on the journal homepage.

Accepted Author Manuscripts: An accepted author manuscript is the manuscript of an article that has been accepted for publication and which typically includes author-incorporated changes suggested during submission, peer review and editor-author communications.

Authors can share their accepted author manuscript:

- immediately
    - via their non-commercial person homepage or blog
    - by updating a preprint in arXiv or RePEc with the accepted manuscript
    - via their research institute or institutional repository for internal institutional uses or as part of an invitation-only research collaboration work-group
    - directly by providing copies to their students or to research collaborators for their personal use
    - for private scholarly sharing as part of an invitation-only work group on commercial sites with which Elsevier has an agreement
- After the embargo period
    - via non-commercial hosting platforms such as their institutional repository
    - via commercial sites with which Elsevier has an agreement

In all cases accepted manuscripts should:

- link to the formal publication via its DOI
- bear a CC-BY-NC-ND license - this is easy to do
- if aggregated with other manuscripts, for example in a repository or other site, be shared in alignment with our hosting policy not be added to or enhanced in any way to appear more like, or to substitute for, the published journal article.

Published journal article (JPA): A published journal article (PJA) is the definitive final record of published research that appears or will appear in the journal and embodies all value-adding publishing activities including peer review co-ordination, copy-editing, formatting, (if relevant) pagination and online enrichment.

Policies for sharing publishing journal articles differ for subscription and gold open access articles:

Subscription Articles: If you are an author, please share a link to your article rather than the full-text. Millions of researchers have access to the formal publications on ScienceDirect, and so links will help your users to find, access, cite, and use the best available version.

Theses and dissertations which contain embedded PJAs as part of the formal submission can be posted publicly by the awarding institution with DOI links back to the formal publications on ScienceDirect.

If you are affiliated with a library that subscribes to ScienceDirect you have additional private sharing rights for others' research accessed under that agreement. This includes use for classroom teaching and internal training at the institution (including use in course packs and courseware programs), and inclusion of the article for grant funding purposes.

Gold Open Access Articles: May be shared according to the author-selected end-user license and should contain a CrossMark logo, the end user license, and a DOI link to the formal publication on ScienceDirect.

Please refer to Elsevier's posting policy for further information.

18. **For book authors** the following clauses are applicable in addition to the above: Authors are permitted to place a brief summary of their work online only. You are not allowed to download and post the published electronic version of your chapter, nor may you scan the printed edition to create an electronic version. **Posting to a repository:** Authors are permitted to post a summary of their chapter only in their institution's repository.

19. **Thesis/Dissertation**: If your license is for use in a thesis/dissertation your thesis may be submitted to your institution in either print or electronic form. Should your thesis be published commercially, please reapply for permission. These requirements include permission for the Library and Archives of Canada to supply single copies, on demand, of the complete thesis and include permission for Proquest/UMI to supply single copies, on demand, of the complete thesis. Should your thesis be published commercially, please reapply for permission. Theses and dissertations which contain embedded PJAs as part of the formal submission can be posted publicly by the awarding institution with DOI links back to the formal publications on ScienceDirect.

Elsevier Open Access Terms and Conditions

You can publish open access with Elsevier in hundreds of open access journals or in nearly 2000 established subscription journals that support open access publishing. Permitted third party re-use of these open access articles is defined by the author's choice of Creative Commons user license. See our open access license policy for more information.

Terms & Conditions applicable to all Open Access articles published with Elsevier:

Any reuse of the article must not represent the author as endorsing the adaptation of the article nor should the article be modified in such a way as to damage the author's honour or reputation. If any changes have been made, such changes must be clearly indicated.

The author(s) must be appropriately credited and we ask that you include the end user license and a DOI link to the formal publication on ScienceDirect.

If any part of the material to be used (for example, figures) has appeared in our publication with credit or acknowledgement to another source it is the responsibility of the user to ensure their reuse complies with the terms and conditions determined by the rights holder.

Additional Terms & Conditions applicable to each Creative Commons user license:

CC BY: The CC-BY license allows users to copy, to create extracts, abstracts and new works from the Article, to alter and revise the Article and to make commercial use of the Article (including reuse and/or resale of the Article by commercial entities), provided the user gives appropriate credit (with a link to the formal publication through the relevant DOI), provides a link to the license, indicates if changes were made and the licensor is not represented as endorsing the use made of the work. The full details of the license are available at http://creativecommons.org/licenses/by/4.0.

CC BY NC SA: The CC BY-NC-SA license allows users to copy, to create extracts, abstracts and new works from the Article, to alter and revise the Article, provided this is not done for commercial purposes, and that the user gives appropriate credit (with a link to the formal publication through the relevant DOI), provides a link to the license, indicates if changes were made and the licensor is not represented as endorsing the use made of the

work. Further, any new works must be made available on the same conditions. The full details of the license are available at http://creativecommons.org/licenses/by-nc-sa/4.0.

CC BY NC ND: The CC BY-NC-ND license allows users to copy and distribute the Article, provided this is not done for commercial purposes and further does not permit distribution of the Article if it is changed or edited in any way, and provided the user gives appropriate credit (with a link to the formal publication through the relevant DOI), provides a link to the license, and that the licensor is not represented as endorsing the use made of the work. The full details of the license are available at http://creativecommons.org/licenses/by-nc-nd/4.0. Any commercial reuse of Open Access articles published with a CC BY NC SA or CC BY NC ND license requires permission from Elsevier and will be subject to a fee.

Commercial reuse includes:

- Associating advertising with the full text of the Article
- Charging fees for document delivery or access
- Article aggregation
- Systematic distribution via e-mail lists or share buttons

Posting or linking by commercial companies for use by customers of those companies.

20. **Other Conditions**:

v1.10

Questions? customercare@copyright.com or +1-855-239-3415 (toll free in the US) or +1-978-646-2777.